

University of Alberta

Design, Fabrication, and Testing of High-Frequency High-Numerical-Aperture Annular
Array Transducer for Improved Depth-of-Field Photoacoustic Microscopy

by

Huihong Lu

A thesis submitted to the Faculty of Graduate Studies and Research

in partial fulfillment of the requirements for the degree of

Master of Science

in

Biomedical Engineering

Department of Electrical and Computer Engineering

© Huihong Lu

Spring 2012

Edmonton, Alberta

Permission is hereby granted to the University of Alberta Libraries to reproduce single copies of this thesis and to lend or sell such copies for private, scholarly or scientific research purposes only. Where the thesis is converted to, or otherwise made available in digital form, the University of Alberta will advise potential users of the thesis of these terms.

The author reserves all other publication and other rights in association with the copyright in the thesis and, except as herein before provided, neither the thesis nor any substantial portion thereof may be printed or otherwise reproduced in any material form whatsoever without the author's prior written permission.

Abstract

Researchers have been using single-element transducers for photoacoustic microscopy (PAM), but such systems have limited depth-of-field due to single focus. This project was to develop a high-frequency annular array transducer for improved depth-of-field PAM. We have designed a concave 40 MHz ultrasound transducer which has 8 annular array elements with equal area. The outer ring is 12 mm in diameter, the geometric focus is 12 mm, and the space between each annulus is 100 μm . The array was fabricated by lithographically patterning metalized polyimide film to define back electrodes. 9-micron-PVDF film was press-fit into the array pattern with epoxy as a backing material and a single drop of epoxy as a bonding layer. The array exhibits high sensitivity to high-frequency photoacoustic signals. Dynamic focusing of amplified and digitized signals permit extended depth-of-field imaging compared to the single-element transducer case. Dark-field light-delivery and 3-axis motorized scanning permit 3-D photoacoustic microscopy.

Acknowledgement

A special note of thanks goes to Acoustic Vision Technologies Inc, in particular William Gibson (PhD, PEng) who offered lab facilities for fabricating the transducers, who co-advised the candidate, and offered practical knowledge and experience regarding the transducer fabrication. We are also grateful to him for reading and correcting a couple of chapters of this thesis.

We gratefully acknowledge funding from NSERC (355544-2008, 375340-2009, STPGP 396444), Terry- Fox Foundation and the Canadian Cancer Society (TFF 019237, TFF 019240, CCS 2011-700718), the Alberta Cancer Research Institute (ACB 23728), the Canada Foundation for Innovation, Leaders Opportunity Fund (18472), Alberta Advanced Education & Technology, Small Equipment Grants Program (URSI09007SEG), Microsystems Technology Research Initiative (MSTRIRES0003166), University of Alberta Startup Funds, and Alberta Ingenuity / Alberta Innovates scholarships for graduate and undergraduate students who helped with this project.

We acknowledge Tim DeWolf, Tyler Harrison, and Alex Forbrich for their work on programming our 3-axis motor controller. We acknowledge help from Steve and Rick for guidance regarding board layout, nanofabrication staff including Stephanie, Bob, and Michael for their help with photolithography.

Table of Contents

Ch1: Objectives and Motivation -----	1-3
1.1 Photoacoustic Microscopy-----	1-2
1.2 Organization of this thesis-----	3
Ch2: Background on Photoacoustic Imaging -----	4-28
2.1 Introduction of photoacoustic imaging-----	4-7
2.2 Comparison between photoacoustic imaging and other imaging techniques--	7-9
2.2.1 Introduction of biomedical imaging techniques-----	7
2.2.2 Comparison of medical imaging modalities-----	8-9
2.3 Light propagation in tissue-----	9-15
2.3.1 Initial photoacoustic pressure-----	9-12
2.3.2 General photoacoustic equation-----	12-13
2.3.3 General forward solution-----	13-15
2.4 PA imaging systems and reconstruction algorithms-----	15-20
2.4.1 Introduction of PA imaging systems-----	15
2.4.2 Dark-field confocal PAM-----	15-18
2.4.3 PAT system-----	18-19
2.4.4 Reconstruction algorithm for different geometry-----	20
2.5 Application of photoacoustic imaging (literature review of PAI)-----	20-27
2.5.1 Application of PAT system-----	20-22
2.5.2 Application of PAM system-----	23-24
2.5.3 OR-PAM applications-----	24-26

2.5.4 Flow imaging and oxygen metabolism-----	26
2.5.5 Optical property estimation-----	26-27
2.6 Motivation to use high-frequency annular arrays-----	27-28
Ch3: Background on Ultrasound and Transducers -----	29-52
(including annular array)	
3.1 Introduction of ultrasound-----	29-33
3.1.1 Physical principles-----	29-30
3.1.2 Characteristics of ultrasound-----	30-33
3.2 Introduction of transducers-----	33-39
3.2.1 Field profile analysis for circular ultrasound transducers-----	35-37
3.2.2 Equivalent electrical circuit models-----	38-39
3.3 US imaging: A-scan, B-scan, C-scan systems-----	39-42
3.3.1 A-scan system-----	39
3.3.2 B-scan system-----	39-41
3.3.3 C-scan system-----	41-42
3.4 Fabrication of different linear array high-frequency transducers----- and their characteristics	42-44
3.5 High frequency ultrasound imaging methods & applications-----	44-47
3.6 Introduction of annular array transducers-----	47-48
3.7 Comparison of piezoelectric materials-----	48-49
3.7.1 Disadvantages of certain materials for transducer fabrication-----	49
3.7.2 Advantage properties for transducer fabrication-----	49
3.8 Different fabrication methods of annular array transducers-----	50-52

Ch4: Annular Array Simulations -----	52-68
4.1 Ultrasound pulse-echo impulse response-----	52-54
4.2 Simulation software-----	54
4.3 Modeling photoacoustic point-spread functions and reciprocity-----	55-56
4.4 The imaging process and point-spread functions-----	56-57
4.5 Simulation of PSFs using element concave ultrasound transducers-----	57-59
4.6 Simulation of annular array concave ultrasound transducer-----	59-60
4.7 Simulation of annular array pulse-echo-----	60-61
ultrasound point-spread functions	
4.8 Simulation of annular array-----	61-63
photoacoustic point-spread functions	
4.9 Dynamic receive (DR) beam-forming (algorithm & equations)-----	63-66
4.10 Main lobe relative to maximum side lobe level-----	66-68
Ch5: Annular Array Concave UT: Fabrication and Characterization ----	69-87
5.1 Pattern (copper-coated) Polyimide film-----	69-78
5.1.1 Annular array mask design-----	69-73
5.1.2 Photoresist deposit-----	73-74
5.1.3 Photoresist baking process-----	74-75
5.1.4 Photolithography-----	75-77
5.1.5 Developing-----	77
5.1.6 Etching-----	77-78
5.1.7 Stripping photoresist-----	78
5.2 Annular array concave ultrasound transducer fabrication-----	78-84

5.2.1 Fabrication materials-----	80
5.2.2 Film bonding-----	80-81
5.2.3 Press-fit assembly-----	81-82
5.2.4 Epoxy backing-----	82-83
5.2.5 Wire attachment-----	83-84
5.3 Annular array concave ultrasound transducer characterization-----	84-87
5.3.1 PCB board design-----	84-86
5.3.2 Fabricated annular array concave ultrasound transducer testing-----	86-87
Ch 6: Photoacoustic Microscopy Experiments, Limitations and Proposed Solutions -----	88-97
6.1 PAM experiment setup-----	88-92
6.1.1 Laser and optical system setup-----	89
6.1.2 3-axis stage-----	89-90
6.1.3 Light probe design-----	90
6.1.4 8-channel gage card-----	91
6.1.5 Mini-circuit amplifiers-----	91
6.1.6 Photo of PAM experiment system-----	92
6.2 PAM experiment results-----	92-95
6.2.1 PA image of hair by fabricated annular array ultrasound transducer-----	93-94
6.2.2 PA image of fiber by fabricated annular array ultrasound transducer-----	94-95
6.3 Limitations-----	95-96
6.3.1 Side lobe level issue-----	95

6.3.2 3-axis scanning limitation-----	96
6.3.3 Real-time imaging limitation-----	96
6.4 Proposed solution-----	96-97
6.4.1 Spray-on technique-----	96-97
Ch 7: Discussion, Conclusions, and Future Work -----	98-101
7.1 Discussion-----	98-101
Bibliography -----	102-110
Appendices -----	111-121
Appendix 1-----	111-113
Appendix 2-----	114-116
Appendix 3-----	117-119
Appendix 4-----	120-121

List of Tables

Table I-----8

Table II-----49

List of Figures

Figure 2.1-----	4
Figure 2.2-----	5
Figure 2.3-----	6
Figure 2.4-----	11
Figure 2.5-----	16
Figure 2.6-----	17
Figure 2.7-----	19
Figure 2.8-----	19
Figure 2.9-----	20
Figure 2.10-----	21
Figure 2.11-----	21
Figure 2.12-----	23
Figure 2.13-----	23
Figure 2.14-----	25
Figure 2.15-----	27
Figure 3.1-----	29
Figure 3.2-----	32
Figure 3.3-----	33
Figure 3.4-----	35
Figure 3.5-----	37
Figure 3.6-----	38

Figure 3.7-----40

Figure 3.8-----42

Figure 3.9-----46

Figure 3.10-----47

Figure 3.11-----50

Figure 4.1-----52

Figure 4.2-----55

Figure 4.3-----56

Figure 4.4-----57

Figure 4.5-----58

Figure 4.6-----59

Figure 4.7-----60

Figure 4.8-----61

Figure 4.9-----62

Figure 4.10-----63

Figure 4.11-----64

Figure 4.12-----65

Figure 4.13-----67

Figure 4.14-----68

Figure 5.1-----69

Figure 5.2-----70

Figure 5.3-----71

Figure 5.4-----71

Figure 5.5-----72

Figure 5.6-----73

Figure 5.7-----74

Figure 5.8-----74

Figure 5.9-----75

Figure 5.10-----76

Figure 5.11-----76

Figure 5.12-----77

Figure 5.13-----78

Figure 5.14-----78

Figure 5.15-----79

Figure 5.16-----80-81

Figure 5.17-----82

Figure 5.18-----82

Figure 5.19-----83

Figure 5.20-----83

Figure 5.21(a)-----84

Figure 5.21(b)-----85

Figure 5.22-----86

Figure 5.23-----87

Figure 6.1-----88

Figure 6.2-----90

Figure 6.3-----91

Figure 6.4-----92

Figure 6.5-----93

Figure 6.6-----94

Figure 6.7-----95

List of Symbols and Abbreviations

Abbreviations

PAI: photoacoustic imaging

PAM: photoacoustic microscopy

PAT: photoacoustic tomography

UT: ultrasound transducer

NA: numerical aperture

OR-PAM: optical resolution photoacoustic microscopy

HbO₂: oxygenated hemoglobin

HbR: deoxygenated hemoglobin

NIR: near-infrared

SO₂: oxygen saturation of hemoglobin

MPE: maximum permissible exposure

ANSI: American National Standard Institute

ICG: Indocyanine Green

ICG-PEG: indocyanine green polyethylene glycol

OCT: optical coherence tomography

FP: Fabry-Perot

HH-OR-PAM: handheld probe optical resolution photoacoustic microscopy

F-OR-PAM: fiber-based optical-resolution photoacoustic microscopy

fps: frames per second

cMUTs: capacitive micromachined ultrasonic transducers

PVDF: polyvinylidene fluoride

FWHM: full width at half maximum

PSF: point spread function

DR: dynamic-receive

DWL: Heidelberg direct write laser

WD: wet deck

IPA: isopropyl alcohol

MRay: Mega Rayleigh

IM: impedance matching

PCB: printed circuit board

SMA: Sub miniature version A

Symbols

L_p : characteristic dimension of the heated tissue volume region

D_T : thermal diffusivity of the tissue with a unit of m^2/s

τ_p : temporal laser pulse duration

k : isothermal compressibility, approximately $5 \times 10^{-10} \text{ Pa}^{-1}$ for water and soft tissue

β : thermal coefficient of volume expansion, approximately $4 \times 10^{-4} \text{ K}^{-1}$ for muscle

$p(r)$: changes in pressure at position r with unit of Pascal

$T(r)$: changes in temperature at position r with unit of Kelvin

ρ : mass density, approximately 1000 kg/m^3 for water or soft tissue

C_p : specific heat capacity at constant pressure

C_v : specific heat capacity at constant volume and both have the unit of $J/(kg \text{ K})$

A_e : local energy deposition density or specific and volumetric optical absorption density in J/cm^3

μ_a : absorption coefficient in cm^{-1}

F : local light or radio frequency fluence in J/cm^2

p_0 : immediate pressure rise or pressure wave after thermal absorption or thermal expansion due to laser excitation

Γ : Gruneisen parameter

F_0 : incident laser fluence in J/m^2

μ_{eff} : extinction coefficient

c : speed of sound in tissue

F_0 : incident laser fluence

μ_s : tissue scattering coefficient

$H(r, t)$: heating function

Φ : fluence rate

ϕ_v : velocity potential

S_0 : detection surface

Ω_0 : 2π

θ_0 : angle between the detection surface normal and the vector facing to the reconstruction point r

f : frequency

λ : wavelength

T : period

α_0 : temperature-dependent factor

θ_i : incident angle

θ_r : reflected angle

c_1 and c_2 : ultrasound wave propagation velocities in two different mediums respectively

Z_1 and Z_2 : the acoustic impedances of the two mediums

p_i and p_r : incident and reflection ultrasound wave pressure

$R_{1,2}$: reflection from medium 2 to medium 1

$T_{1,2}$: transmission from medium 1 to medium 2

$v(t)$: piston transducer surface average velocity

$h(r, t)$: impulse response

a : focal length

D : aperture diameter

Z_B : backing region acoustic impedance

Z_T : transmission region acoustic impedance

k^t : piezoelectric coupling factor

Z_a : acoustic impedance of the piezoelectric material

$T_i(t)$: input voltage of a delta-function

$F_o(t)$: force on the receiver crystal

S : surface area of the receiver crystal

$S(t)$: scattering impulse function

$\delta(t)$: delta function

$\xi_o(x, y)$: spatial apodization weighting across the transducer surface

Ch 1: Objectives and Motivation

1.1 Photoacoustic Microscopy

Photoacoustic microscopy is an emerging biomedical imaging technology that is capable of producing images with optical contrast and ultrasonic spatial resolution. It uses pulsed laser light to excite tissues. Optical energy absorbed by subsurface chromophores is partially converted to heat and subsequent thermoelastic expansion produces acoustic waves that are detected and reconstructed to form images. Photoacoustic signal strength is proportional to local optical absorption coefficients; however, unlike diffuse optical tomography, spatial resolution is not fundamentally limited by multiple scattering. Instead spatial resolution is limited by the diffraction limits of ultrasound. The optical contrast afforded by photoacoustic imaging is complementary to the acoustic backscatter information provided by ultrasound and can provide functional information about blood oxygen saturation. It has also been used to image gene expression, image actively or passively targeted contrast agents, including nanoparticle contrast agents, and is being actively pursued by many groups for a variety of pre-clinical and clinical applications.

Recently, Maslov et al introduced dark-field confocal Photoacoustic Microscopy (often abbreviated as PAM). Laser light was directed around a single-element high-numerical aperture focused high-frequency transducer (50MHz, 0.45 NA) so the light was loosely focused near the region of the acoustic focus. The acoustic focus was positioned below the tissue surface so that a ring illumination was incident on the tissue surface. This system demonstrated unprecedented images of the microvasculature in small animals and even in humans to depth of ~3mm with 45 micron lateral and 15 micron axial spatial resolution. Functional imaging results from the system resulted in multiple Nature articles. Despite its success this system has some key limitations. One limitation is the imaging speed: one A-scan line acquisition was acquired per laser shot, and to form a 3D data set with $N \times N$ A-scan lines of M samples depth, N^2 laser shots were required. The entire setup was mechanically raster scanned to a new incremental position for each laser shot so mechanical scanning and data transfer were also speed limitations, however, the 10Hz laser pulse-repetition rate was the most critical time bottleneck. Another limitation of this system is its limited depth of field. Images were focused only within a very limited region (~1mm) around the focal zone of the transducer.

Other embodiments of photoacoustic imaging have had some success in improving upon some aspects of these limitations (including speed and imaging depth) but

none has rivalled the image quality of dark-field confocal PAM. Systems based on linear array transducers have provided realtime imaging frame-rates, overcoming speed limitations of dark-field confocal PAM, however, these systems have lacked the numerical apertures needed to form highly focused images. They also suffer from some signal-to-noise limitations. Such linear array transducers are fundamentally limited to lateral electronic focusing with f-numbers no larger than about 2 [$NA=1/(2f_{\#})= 0.25$] due to requirements of the Fresnel approximation needed for electronic (dynamic focusing) to work effectively. Elevational focusing of linear arrays is typically even worse (f-number of ~ 4).

The goal of this thesis is to develop a dark-field confocal photoacoustic microscopy system based on custom-fabricated high-frequency and high-numerical aperture annular array transducers, which do not compromise the image quality afforded by dark-field confocal PAM but which improves upon its depth-of-field. The purpose of fabricating these transducers is to achieve the high focusing quality and spatial resolution provided by high-frequency high-numerical aperture single-element transducers while attempting to extend the depth of field by using dynamic-receive focusing. To our knowledge, our work represents the first implementation of high-frequency, high-numerical aperture annular array transducers for photoacoustic imaging.

To address this challenge we consider high-frequency annular arrays. Annular arrays are concentric rings of piezoelectric material that can be dynamically focused electronically along their concentric depth axis. High image quality using only limited number of annuli has been demonstrated for ultrasound imaging by other groups previously.

Annular arrays with annuli formed on a planar piston will be fundamentally limited to f-numbers of ~ 2 when electronic focusing is used; however, annuli can be formed on a concave surface. A concave annular array will provide a natural geometric focus and additional electronic focusing. We hypothesized that this design should permit high-numerical aperture (low-f-number) focusing with the additional advantage of dynamic receive focusing to extend the depth-of-field over fixed focus single element transducers.

One of the first patents regarding photoacoustic imaging involved annular arrays but did not involve high-numerical apertures or high frequencies as we propose. To our knowledge this is the first work regarding high-frequency high-numerical aperture annular arrays for photoacoustic microscopy.

1.2 Organization of this thesis

After this introductory chapter, Chapter 2 introduces photoacoustic imaging and some basics of light propagation in tissue, Chapter 3 introduces fundamentals of ultrasound and ultrasound transducers, Chapter 4 discusses acoustic field modeling of annular array transducers, Chapter 5 discusses fabrication and performance characterization of piezo-polymer annular arrays, Chapter 6 discusses integration of the annular arrays in a photoacoustic microscopy system, and Chapter 7 provides summary, conclusions, and future outlook. Some of the key results presented in Chapters 4-6 were presented in our SPIE Photonics West Conference paper [1].

Ch2: Background on Photoacoustic Imaging

2.1 Introduction of photoacoustic imaging

The photoacoustic effect refers to the conversion of light energy to acoustic waves and was discovered over 100 years ago by Alexander Graham Bell. Use of the photoacoustic effect for biomedical imaging, however, is relatively new. In biomedical photoacoustic imaging, a short-pulse laser illuminates tissue. The optically absorbing chromophores in the tissue partially absorb the electromagnetic energy, causing thermal expansion. Acoustic or sound waves are generated because of the thermal expansion and are detected by ultrasound transducers to form an image. The acoustic wave strength depends on the optical energy absorption of the tissue [2]. Photoacoustic imaging (PAI) can provide images with high optical contrast and high ultrasonic resolution. A variation of this technology, called optical resolution photoacoustic microscopy (OR-PAM) can also provide high optical at the expense of imaging depth. Photoacoustic imaging has been used in preclinical and clinical studies to provide images with structural, functional and molecular information. For example, it can detect tumor locations in deep tissue and monitor tumor growth [2]. Photoacoustic imaging can also visualize the total hemoglobin concentration and oxygen saturation in blood vessels with both high contrast and resolution [2]. The general process of

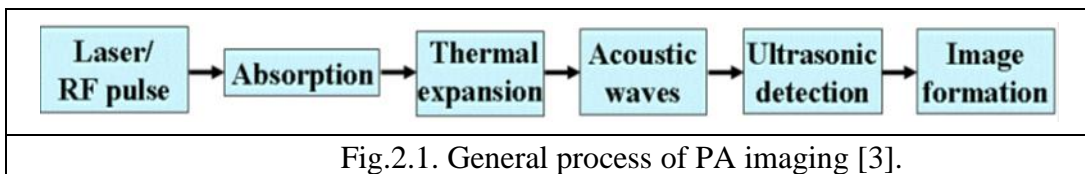
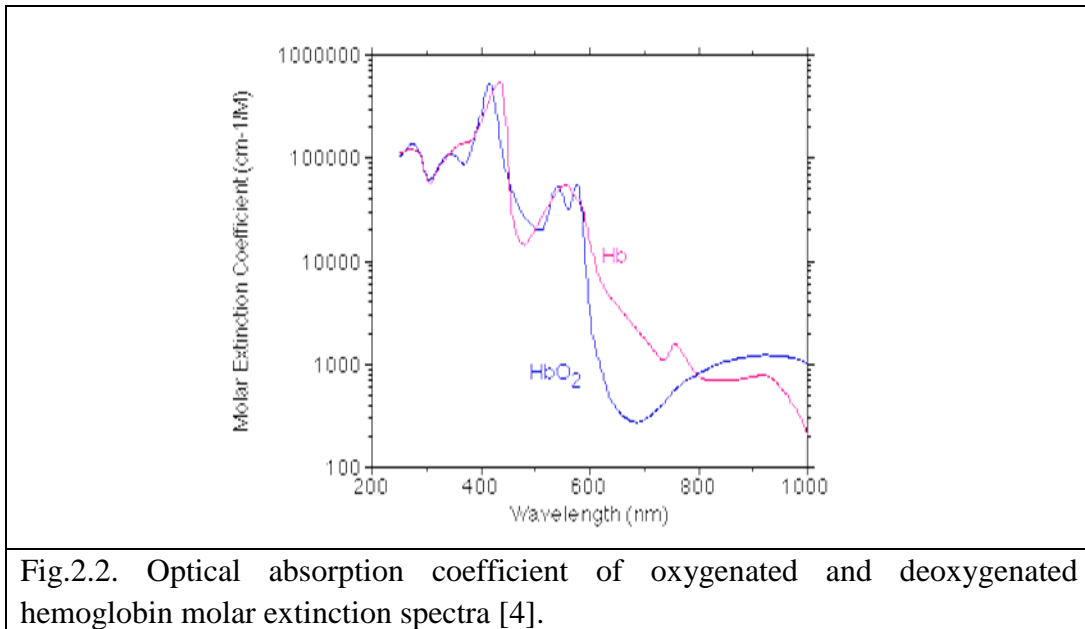


Fig.2.1. General process of PA imaging [3].

photoacoustic imaging can also be illustrated by figure 2.1 [3].

As noted, photoacoustic image contrast is determined by optical absorption properties of the tissue. The dominant endogenous optically-absorbing chromophores in tissues are oxygenated and deoxygenated hemoglobin (HbO_2 and HbR) contained in red-blood cells and melanin (primarily limited to the skin) [3]. Below wavelengths of 600 nm, oxygenated hemoglobin is a very strong absorber. It's absorption in the far-red and near-infrared (NIR) regions decreases with two orders of magnitude and stays low. Unlike oxygenated hemoglobin, although deoxygenated hemoglobin gradually decreases when wavelength increases, it always stays quite high in most wavelength regions. The relationship between oxygenated and deoxygenated hemoglobin with wavelength is illustrated in figure 2.2 [4]. Using multiple-wavelength illumination schemes, the oxygen saturation of hemoglobin (SO_2) can be imaged with PAI. SO_2 is an important

parameter related to tissue oxygenation and metabolism and may be important in early stage cancer diagnosis [2].



Photoacoustic imaging spatial resolution, including axial and lateral resolution are determined by ultrasonic detection. Generally, the axial resolution is inversely proportional to the bandwidth of an ultrasound transducer. For a 100% fractional bandwidth transducer, the resolution will essentially be the wavelength of the center frequency. For example, the speed of sound in tissue is approximately 1.5 mm/ μ s, with the sacrifice of ultrasound penetration depth, 1 MHz and 10 MHz bandwidths provide approximately 1 mm and 0.1 mm spatial resolution proportionally [2]. The lateral resolution is determined by the center frequency and focal length of the ultrasound transducer. In other words, lateral resolution can be defined as $0.61 \times (\lambda/NA)$ where λ is the wavelength and NA is the numerical aperture of the ultrasound transducer [3]. If the center frequency is high, the wavelength will be small; and if the NA is large, the final result of the equation will be small, resulting in high lateral resolution. The numerical aperture of an ultrasound transducer is determined by its active aperture and focal length, also relates to the f-number in a reciprocal proportional way; because the f-number equals to the focal length divided by the active aperture diameter. When the value of NA is greater than 0.5, this ultrasound transducer is considered to have a large numerical aperture. The axial resolution in PAI is mainly related to the radiation pulse width and bandwidth provided by the ultrasound transducer. Normally, the light source in PAI is short-pulse laser or radio frequency pulse to

ensure good axial resolution in PAI image. Ideally, ultrasound transducer with broad bandwidth is used in PAI system to also help achieve good axial resolution.

The maximum imaging depth in PAI is essentially limited by photoacoustic signal attenuation and light penetration. Acoustic attenuation is dependent on frequency. The frequency dependence of the acoustic attenuation coefficient scales with frequency as $\mu = af^b$, where μ is the ultrasound attenuation coefficient, f is the ultrasound center frequency, and a , b are two constants [5]. Ultrasound and photoacoustic systems with high-frequency transducers will offer less ultrasonic penetration compared to lower-frequency transducers, but will provide higher spatial resolution [5]. Typical values of the ultrasound attenuation coefficient for many soft tissues are approximately 0.3 to 0.6 dB cm⁻¹ MHz⁻¹.

Optical contrast provided by photoacoustic imaging can be attained by other various optical modalities; however, light scattering in tissue can be very strong,

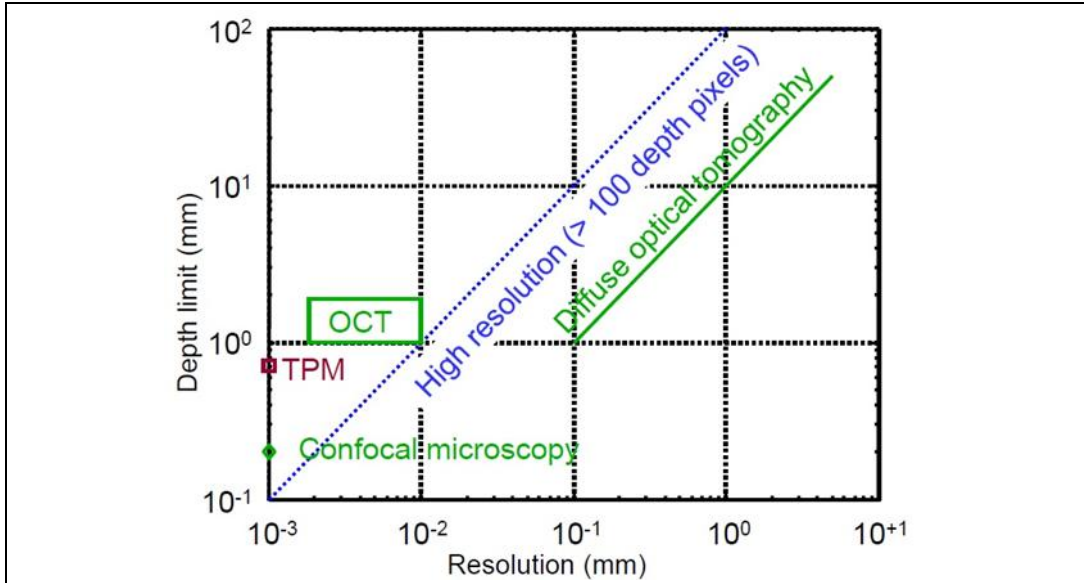


Fig.2.3. Imaging depth to resolution ratio for modern imaging techniques [6].

challenging spatial resolution. Compared with optical scattering, ultrasonic scattering cross sections are two to three orders of magnitude smaller. Because photoacoustic imaging can rely on ultrasound to provide resolution, PAI can have relatively deeper imaging depth than pure optical imaging for a desired spatial resolution [2]. Overall, PAI provides better imaging depth to resolution ratio than pure optical imaging. Figure 2.3 shows the imaging depth and resolution for several current optical imaging techniques; photoacoustic imaging follows along the blue dashed line [6]. Besides better spatial resolution and imaging depth,

photoacoustic imaging also provides images with less speckle artifacts compared to pure ultrasound B-mode imaging [3].

Photoacoustic imaging is a safe imaging modality. Short-pulse lasers or radio frequency pulses are usually used to excite tissue. These two kinds of waves fall in the non-ionizing wave category, which are not harmful to human health. The maximum permissible exposure, so-called MPE, becomes a very important parameter to regulate the electromagnetic radiation level exposed to a person without hazardous effects or changes in biological features. The MPE levels relate to electromagnetic wavelength or frequency, the exposure time, and the pulse repetition rate [2]. For a given wavelength and exposure duration, the MPE can be expressed in the unit of J/cm^2 or W/cm^2 . The MPE value is directly proportional to the wavelength and indirectly proportional to the exposure time. The IEEE Standard provides regulation values of the MPE levels with respect to human exposure to radio frequency pulse application. The American National Standard Institute (ANSI) provides regulation values of the MPE levels with respect to human exposure to laser pulse application [2]. For example, if a spot of human skin is exposed to laser for more than 10 seconds, the ANSI restricts the mean irradiance value to be under $200 \text{ mW}/\text{cm}^2$, regulating the value of maximum permissible repetition rate is approximately 30 Hz [3]. Typical ANSI limits for pulsed laser exposure are $20\text{mJ}/\text{cm}^2$ for visible light to as high as $100\text{mJ}/\text{cm}^2$ for NIR light.

2.2 Comparison between photoacoustic imaging and other imaging techniques

2.2.1 Introduction of biomedical imaging techniques

There are many traditional biomedical imaging methods that have been used to create images of human and animal subjects for medical diagnosis, disease detection, staging, treatment monitoring, and for basic and applied pre-clinical studies. Each imaging modality has respective strengths and weaknesses for a given biomedical task. Some traditional radiographic modalities use ionizing electromagnetic radiation, such as x-rays. Other radiographic techniques which do not use ionizing radiation include ultrasound, and magnetic resonance imaging. Many of these techniques provide tomographic or planar structural images of the body, but are more limited in terms of imaging function, physiology, and biochemistry. Nuclear medicine has the additional capabilities to assess in vivo biochemistry and function quantitatively by imaging radiotracer pharmacokinetics [6]. One could ask why we need a new imaging modality such as photoacoustic imaging. The following section is included to answer this question.

2.2.2 Comparison of medical imaging modalities

Some of the traditional imaging techniques have important limitations. For example, X-ray CT can cause harmful radiation that is not very safe for human body and may be causing some cancers; ultrasound imaging has poor image contrast, and pure optical microscopy and coherence-regime imaging, including confocal microscopy, two-photon microscopy and optical coherence tomography, cannot penetrate beyond approximately 1 mm due to scattering.

Table I: Comparison of different medical imaging technique properties [3]

Medical imaging method	Center frequency [Hz]	Penetration depth [mm]	Axial resolution [μm]	Lateral resolution [μm]	Primary contrast
Confocal microscopy		0.2	3-20	0.3-3	Fluorescence, scattering
Two-photon microscopy		0.5-1	1-10	0.3-3	Fluorescence
Optical coherence tomography	50M	1-2	0.5-10	1-10	Optical scattering
Scanning laser acoustic microscopy	300M	1-2	20	20	Ultrasonic scattering
Acoustic microscopy	50M	20	20-100	80-160	Ultrasonic scattering
Ultrasonography	5M	60	300	300	Ultrasonic scattering
Photoacoustic microscopy	50M	3	15	45	Optical absorption
Photoacoustic tomography	5M	50	700	700	Optical absorption

Therefore, pure optical imaging is not applied for high-resolution imaging beyond this penetration depth. Diffuse optical tomography can penetrate multiple centimeters in tissue but resolution is poor. The basic properties of traditional medical imaging methods are compared in Table I [3]. Photoacoustic microscopy is an attractive modality due to high optical absorption image contrast and high spatial resolution. From Table I, ultrasound imaging has poor contrast for early-stage tumors, and cannot be used to study oxygen saturation or hemoglobin concentration. Pure optical microscopy cannot penetrate deeper than a transport mean-free path

(~1 mm in tissue) due to optical scattering. Since ultrasound waves are 2 or 3 orders of magnitude weaker than optical waves, ultrasound can provide better resolution than optical imaging beyond depths of a few transport mean-free paths. Photoacoustic imaging combines the best properties of pure optical imaging and ultrasound imaging.

2.3 Light propagation in tissue

2.3.1 Initial photoacoustic pressure

Photoacoustic imaging is based on light absorbed by tissue being transformed to acoustic waves via thermoelastic expansion. The light source is usually short-pulse laser. In order to successfully generate photoacoustic signals, there are two important conditions to be considered, called thermal and stress confinements. They are two important timescales needed to be considered in laser heating.

The time scale for thermal diffusion or heat dissipation from electromagnetic energy absorption during thermal conduction is called the thermal relaxation time, which can be approximately expressed by [7]

$$\tau_{th} \approx \frac{L_p^2}{(4D_T)} \quad (2.1)$$

Here, L_p is the characteristic dimension of the heated tissue volume region and D_T is the thermal diffusivity of the tissue with a unit of m^2/s [7]. For most soft tissues, the value of D_T is approximately $1.4 \times 10^{-3} \text{ cm}^2/s$. The temporal laser pulse duration is expressed by τ_p ; in order to efficiently generate photoacoustic waves, thermal confinement condition must be met, where $\tau_p < \tau_{th}$, and this is when heat diffusion can be neglected during the laser pulse.

Another important time scale is stress transition in the heated region or pressure propagation time, called stress relaxation time, which can be approximately expressed by [5]

$$\tau_s = \frac{L_p}{c} \quad (2.2)$$

Where c is the speed of sound, approximately 1480 m/s in water. If $\tau_s < \tau_{th}$, it is the stress confinement condition, where stress propagation can be neglected during the laser pulse [2].

When laser is excited on tissue, the local fractional volume expansion of the heated tissue at location r can be expressed by

$$\frac{dV}{V} = -kp(r) + \beta T(r) \quad (2.3)$$

Here, k is the isothermal compressibility, which is approximately $5 \times 10^{-10} \text{ Pa}^{-1}$ for water and soft tissue; β is the thermal coefficient of volume expansion, which is approximately $4 \times 10^{-4} \text{ K}^{-1}$ for muscle; $p(r)$ is the changes in pressure at position r with unit of Pascal, and $T(r)$ is the changes in temperature at position r with unit of Kelvin. The isothermal compressibility k is expressed in the following equation [3]

$$k = \frac{C_p}{\rho c^2 C_v} \quad (2.4)$$

Here, ρ is the mass density, which is approximately 1000 kg/m^3 for water or soft tissue; C_p is the specific heat capacity at constant pressure, C_v is the specific heat capacity at constant volume and both have the unit of $\text{J}/(\text{kg K})$; it is very important to distinguish their values for gasses, but not for tissue [5].

When both thermal and stress confinement conditions are satisfied, where $\tau_p < \tau_s < \tau_{th}$, the fractional volume expansion can be neglected and the immediate pressure rise after laser excitation at location r is expressed as [8]

$$p_0(r) = \frac{\beta T(r)}{k} \quad (2.5)$$

If all the absorbed optical energy is assumed to converted to heat, the temperature rise by the short laser pulse at location r can be expressed as [3]

$$T(r) = \frac{A_e}{\rho C_v} \quad (2.6)$$

Here, A_e is the local energy deposition density or specific and volumetric optical absorption density in J/cm^3 , it can be expressed as [2]

$$A_e = \mu_a F \quad (2.7)$$

In this equation, μ_a is the absorption coefficient in cm^{-1} and F is the local light or radio frequency fluence in J/cm^2 . Therefore, the initial pressure can be expressed in a new form as [3]

$$p_0 = \frac{\beta}{k \rho C_v} A_e \quad (2.8)$$

For simplicity, a new dimensionless parameter is defined, called Gruneisen parameter, which is expressed as [3]

$$\Gamma = \frac{\beta}{k\rho C_V} = \frac{\beta c^2}{C_P} \quad (2.9)$$

So, the initial pressure has a more simplified form expressed as [3]

$$p_0 = \Gamma A_e = \Gamma \mu_a F \quad (2.10)$$

In order to better understand photoacoustic effect, a depth profiling can help to illustrate figure 4 by assuming one-dimensional plane wave propagation in a layered medium. Assuming no optical scattering, the initial pressure or stress distribution in this case due to a wide beam impulse can be expressed as [2]

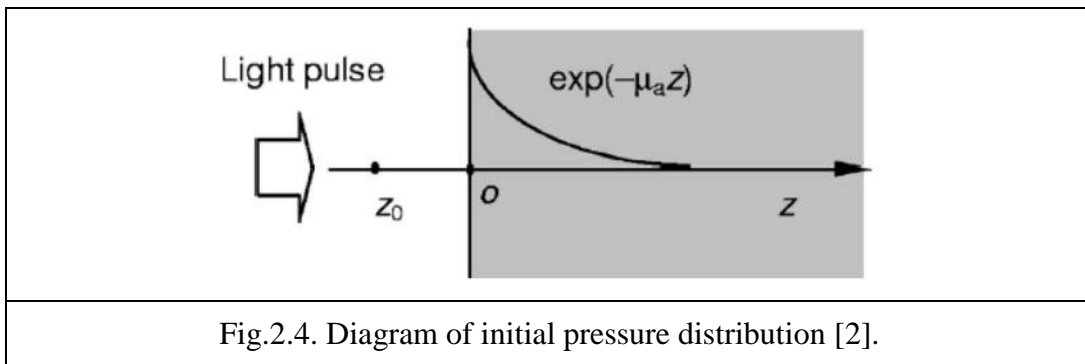
$$p_0(z) = \Gamma \mu_a F_0 \exp(-\mu_a z) \quad (2.11)$$

The acoustic wave has two components with equal amplitude that propagate in the opposite direction along positive and negative z-axis. By neglecting acoustic attenuation and reflected acoustic wave, the acoustic wave at position z_0 when $t > t_0$ is calculated by [2]

$$p_0(z_0, t) = \frac{1}{2} \Gamma \mu_a F_0 \exp[-\mu_a(ct + z_0)] \quad (2.12)$$

Since $z_0 = -ct_0$, then the above equation can be expressed as [2]

$$p_0(z_0, t) = \frac{1}{2} \Gamma \mu_a F_0 \exp[-\mu_a c(t - t_0)] \quad (2.13)$$



Here, p_0 is the pressure wave, Γ is the Gruneisen parameter, F_0 is the incident laser fluence in J/m^2 , and μ_a is the absorption coefficient in cm^{-1} . By measuring the relative profile and fitting the slope of the exponential curve in figure 2.4, the value of μ_a can be calculated [2]

If strong optical scattering is considered, the pressure wave expression is a little different; because instead of μ_a , the exponential decay term will be expressed by the effective attenuation or extinction coefficient μ_{eff} . The new pressure wave expression with μ_{eff} is shown below [2]

$$p_0 = \frac{\beta c^2}{C_p} \mu_a F_0 \exp(-\mu_{eff} z) = \Gamma \mu_a F_0 \exp(-\mu_{eff} z) \quad (2.14)$$

Here, p_0 is the immediate pressure rise or pressure wave after thermal absorption or thermal expansion due to laser excitation, β is the thermal coefficient of volume expansion, c is the speed of sound in tissue, C_p is the specific heat capacity of the tissue at constant pressure, F_0 is the incident laser fluence, Γ is the Gruneisen parameter, μ_a is the absorption coefficient, and μ_{eff} is the effective attenuation or extinction coefficient, which is expressed by [2]

$$\mu_{eff} = \sqrt{3\mu_a(\mu_a + \mu'_s)} \quad (2.15)$$

In this expression, μ_s is the tissue scattering coefficient; this is a more complicated case to study photoacoustic effect or pressure propagation phenomena. Based on the above equations, the depth profile analysis can help determine optical properties of the tissue.

2.3.2 General photoacoustic equation

After introducing the initial pressure rise due to a laser impulse, this section continues to research more on photoacoustic wave generation and propagation in an inviscid medium determined by the general photoacoustic equation [3]

$$\left(\nabla^2 - \frac{1}{v_s^2} \frac{\partial^2}{\partial t^2}\right) p(r, t) = -\frac{\beta}{k v_s^2} \frac{\partial^2 T(r, t)}{\partial t^2} \quad (2.16)$$

Here, $p(r, t)$ represents the acoustic pressure at location r and time t ; $T(r, t)$ is the temperature rise or increase at location r and time t . v_s represents the speed of sound. The left-hand side of the general photoacoustic equation expresses the information of wave propagation, and the right-hand side of equation describes the source term [3].

For thermal confinement condition, the thermal equation is expressed by [3]

$$\rho C_v \frac{\partial T(r, t)}{\partial t} = H(r, t) \quad (2.17)$$

Here, $H(r, t)$ represents the heating function defined as the thermal energy converted per unit time and per unit volume. It relates to the optical absorption

coefficient μ_a and fluence rate Φ , expressed by $H = \mu_a \Phi$. By substituting equation (2.17) into equation (2.16), we can obtain the simplified form of the general photoacoustic equation [3]

$$\left(\nabla^2 - \frac{1}{v_s^2} \frac{\partial^2}{\partial t^2}\right)p(r, t) = -\frac{\beta}{C_p} \frac{\partial H(r, t)}{\partial t} \quad (2.18)$$

From equation (2.18), the right-hand side of the general photoacoustic equation is the source term expressed by the first derivative of H , describing that only time-variant heating produces a pressure wave, not the time-invariant heating [3].

If we want to avoid the time derivative of H term, a new parameter called velocity potential ϕ_v is introduced and its relationship with pressure wave is expressed as [9]

$$p = -\rho \frac{\partial \phi_v}{\partial t} \quad (2.19)$$

By submitting equation (2.19) into equation (2.18), after removing the derivative of H term, the general photoacoustic equation is expressed by [9]

$$\left(\nabla^2 - \frac{1}{v_s^2} \frac{\partial^2}{\partial t^2}\right)\phi_v = \frac{\beta}{\rho C_p} H \quad (2.20)$$

All the parameters in equation (2.20) are already defined previously.

2.3.3 General forward solution [3]

The Green's function is a general approach to solve the general photoacoustic equation, because it is the expression for spatial and temporal impulse response of source term [10]. The Green's function is expressed as [3]

$$\left(\nabla^2 - \frac{1}{v_s^2} \frac{\partial^2}{\partial t^2}\right)G(r, t; r', t') = -\delta(r - r')\delta(t - t') \quad (2.21)$$

Here, r is the source location and t is the source time. For an infinite space, when there is no boundary, the Green's function is expressed as

$$G(r, t; r', t') = \frac{\delta(t - t' - |r - r'|/v_s)}{4\pi|r - r'|} \quad (2.22)$$

Equation (2.22) describes an impulse diverging spherical wave and the reciprocity property is shown as

$$G(r, t; r', t') = G(r', -t'; r, -t) \quad (2.23)$$

By using the Green's function to solve the general photoacoustic equation expressed in equation (2.18), the result is shown as

$$p(r, t) = \int_{-\infty}^{t^+} dt' \int dr' G(r, t; r', t') \frac{\beta}{k v_s^2} \frac{\partial^2 T(r', t')}{\partial t'^2} \quad (2.24)$$

Equation (2.24) describes the pressure response to a random source term. By putting equation (2.23) into equation (2.24), the pressure response is expressed as

$$p(r, t) = \frac{\beta}{4\pi k v_s^2} \int dr' \frac{1}{|r - r'|} \frac{\partial^2 T(r', t')}{\partial t'^2} \Big|_{t'=t-\frac{|r-r'|}{v_s}} \quad (2.25)$$

For thermal confinement condition, the thermal equation is expressed in equation (2.17); by submitting it into equation (2.25), then the pressure response is expressed as

$$p(r, t) = \frac{\beta}{4\pi C_p} \int dr' \frac{1}{|r - r'|} \frac{\partial H(r', t')}{\partial t'} \Big|_{t'=t-\frac{|r-r'|}{v_s}} \quad (2.26)$$

or

$$p(r, t) = \frac{\beta}{4\pi C_p} \frac{\partial}{\partial t} \int dr' \frac{1}{|r - r'|} H(r', t - \frac{|r - r'|}{v_s}) \quad (2.27)$$

If the heat function has the property expressed as $H(\vec{r}', t') = H_s(\vec{r}') H_t(t')$ or $H(\vec{r}', t') = A_e(\vec{r}') H_t(t')$, then equation (2.27) can be simplified as

$$p(r, t) = \frac{\beta}{4\pi C_p} \frac{\partial}{\partial t} \int dr' \frac{A_e(r')}{|r - r'|} H_t(t - \frac{|r - r'|}{v_s}) \quad (2.28)$$

When both thermal and stress confinement conditions are satisfied, where $\tau_p < \tau_s < \tau_{th}$, the heating function is a delta function, $H_t(t') = \delta(t')$; the pressure function describes the delta heating response of a random absorbing object as

$$p(r, t) = \frac{\partial}{\partial t} \left[\frac{\beta}{4\pi C_p} \frac{1}{v_s t} \int dr' A_e(r') \delta\left(t - \frac{|r - r'|}{v_s}\right) \right] \quad (2.29)$$

The content in the square bracket expresses the step heating response. From equation (2.10), the initial pressure response of delta heating can be expressed as

$$p_0(\vec{r}) = \Gamma A_e(\vec{r}) \quad (2.30)$$

By combining equations (2.9) and (2.30) and submitting them into equation (2.29), the result can be used to describe the photoacoustic pressure generated by a random absorbing object, which is expressed as

$$p(r, t) = \frac{1}{4\pi v_s^2} \frac{\partial}{\partial t} \left[\frac{1}{v_s t} \int dr' p_0(r') \delta\left(t - \frac{|r - r'|}{v_s}\right) \right] \quad (2.31)$$

2.4 PA imaging systems and reconstruction algorithms

2.4.1 Introduction of PA imaging systems

Many embodiments of photoacoustic imaging systems have been reported in the literature. Most of them can be classified into one of two types: photoacoustic microscopy (PAM) and photoacoustic tomography (PAT). PAM systems can further be classified as conventional or ultrasonic-resolution PAM and optical-resolution PAM (OR-PAM). The first reported conventional PAM systems (subsequently referred to as simply PAM) scanned a focused single-element ultrasound transducer with dark-field confocal dark-field light delivery over tissue and images were formed directly from the raster-scanned data to form 3D or maximum-amplitude-projection C-Scan 2D image so it does not require additional reconstruction algorithms. Since PAM systems rely on focused ultrasound transducers, imaging depth is limited to the focal zone of the transducer and is additionally limited by ultrasonic and optical attenuation. The axial resolution of PAM relates to the center frequency and the bandwidth of ultrasound transducer; higher center frequency and broader bandwidth will achieve high axial resolution. PAM has been used for measuring oxygen saturation and hemoglobin concentration in blood vessels which have high optical absorption coefficient. PAT system is usually used to image complicated tissue structures. It often uses a pulse laser as the light source and an unfocused ultrasound transducer to detect photoacoustic signal in a circular or spherical motion. The acquired data of optical absorption distribution at different tissue location is transformed to image by using reconstruction algorithm. PAT imaging system has deep penetration ability, for example, it can reach 1 cm depth when the wavelength is 580 nm with an axial resolution of less than 100 μm , and when the wavelength is 1064 nm, and it can reach 7.5 cm and can image 2 mm blood vessels with 1 mm lateral resolution and 0.4 mm depth resolution. PAT is often applied for breast cancer diagnosis, hemodynamics monitoring, and brain lesion detection.

2.4.2 Dark-field Confocal PAM

First reported by Maslov et al, Dark-field Confocal PAM uses dark-field illumination of pulsed-laser light around a high-NA focused ultrasound transducer for detection. In conventional dark-field microscopy, an opaque disc is put in between the condenser lens and the light source in order to reject the ballistic light and only allow the nonballistic light to come through. The tissue sample scatters the

nonballistic light and the ultrasound transducer detects the signal. There is a donut-shaped cross section in the excitation laser beam so that it minimizes the photoacoustic signal from the tissue surface in the field of view. Figure 2.5 illustrates a photoacoustic microscopy system [11]. It uses a tuneable dye laser pumped by an Nd:YAG laser to produce 6.5 ns laser pulse for generating photoacoustic waves. This short laser pulse can generate photoacoustic waves with bandwidth greater than 100 MHz. Through an optical fiber, the laser light is delivered to the scanner. The delivered laser light from the fiber passes through a conical lens to form a ring-shaped pattern which is coaxially aligned with the focused ultrasound transducer. The donut-shaped optical focus is 2 mm in diameter and is much wider than the ultrasound focus.

The photoacoustic signals are received at each location due to each laser-pulse excitation as a function of time by an ultrasound transducer, which are amplified by low-noise amplifiers and digitally recorded. The ultrasound transducer is scanned in a raster motion to produce a 3-D image without any signal averaging. For acoustic coupling, the ultrasound transducer is placed in water in a plastic container, whose bottom has a small opening that is sealed with thin layer of disposable polyethylene membrane [9]. PAM is good for imaging biological tissue with high

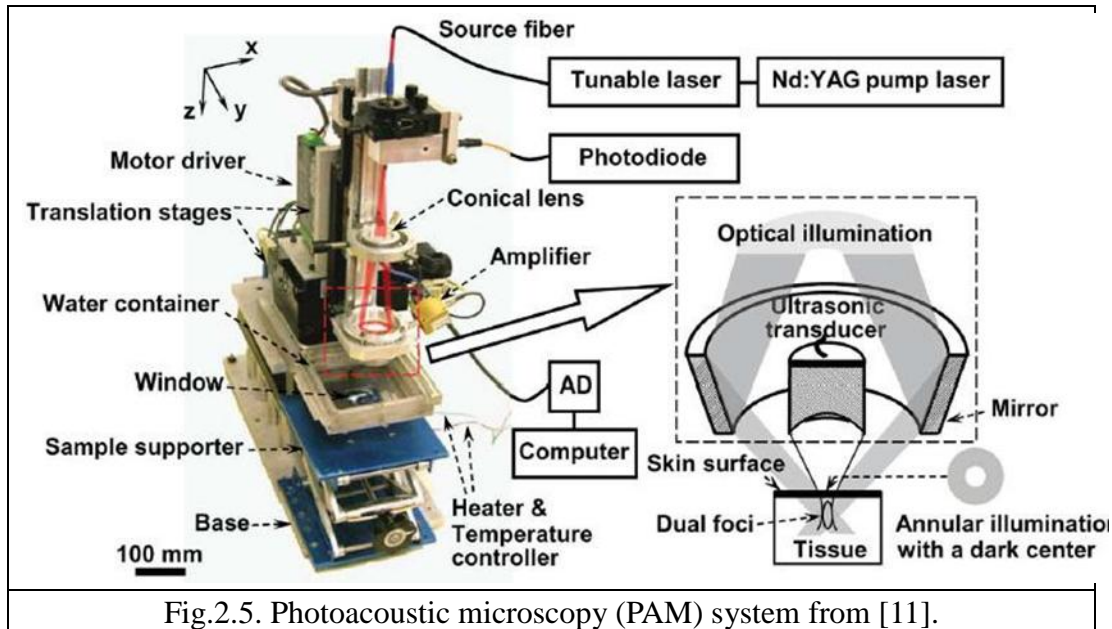


Fig.2.5. Photoacoustic microscopy (PAM) system from [11].

optical absorption coefficient in the quasi-diffusive regime. As noted, the spatial resolution of PAM relates to the ultrasound transducer parameters, not the optical excitation parameters. In order to achieve high spatial resolution in PAM, the ultrasound transducer should have high center frequency, large numerical aperture (NA), and broad bandwidth. For soft tissue, the imaging depth of PAM is not only

limited by light penetration, but also ultrasound penetration, which is inversely proportional to acoustic attenuation. The PAM system shown below uses a high-frequency 50-MHz ultrasound transducer capable of 45 micron lateral resolution, 15 micron axial resolution for ~3mm penetration depths. This depth represents depths significantly beyond the transport-mean-free path but not yet into the full diffusion-regime. Other techniques have a difficult time imaging these depths because it represents the transport regime, where the radioactive transport equation must be used as photon trajectories are not sufficiently randomized to use simpler diffusion theory [11]. ANSI safety limits for maximum permissible exposure are observed. Its acquisition time is limited by the 10 Hz laser pulse repetition rate. Each A-scan line is acquired in 2 μ s, which is equivalent to image 3 mm in depth with speed of sound of 1.5 mm/ μ s.

Traditional photoacoustic microscopy (PAM) imaging speed is limited by laser repetition rates and mechanically scanning. Recently, a research group uses a 30 MHz high-frequency linear array ultrasound transducer and KHz-repetition-rate

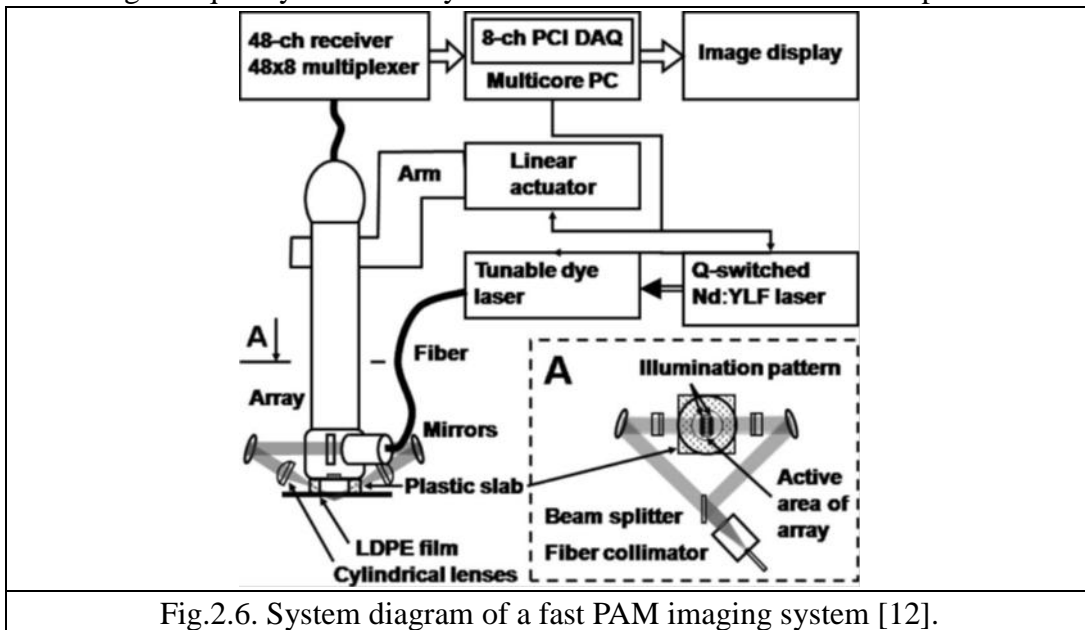


Fig.2.6. System diagram of a fast PAM imaging system [12].

laser for realtime frame-rate PAM. The multi-element array eliminates the need of mechanical scanning and permits dynamic focusing. This linear array ultrasound transducer provides approximately 25 μ m axial and less than 100 μ m lateral resolution. The PAM system using such an array transducer can provide real-time B-scan imaging. Mechanical scanning in the elevation direction can extend view to 3D. The laser beam is delivered by optical fiber and collimated by a fiber collimator; a free space optic setup associated with the linear array ultrasound transducer to further guide the laser beam. This optical setup helps achieve high signal-to-noise ratio. Since less hardware communication is used in this PAM system, it only takes

about 3 s to view an MAP image, and achieves cross-section (B-scan) real-time imaging with beamforming at 50 Hz, 3-D imaging with 166 B-scan frames with postbeamforming at 1 Hz, demonstrating the fast imaging system in all reported photoacoustic imaging systems and figure 2.6 shows a system diagram of this fast PAM system [12].

2.4.3 PAT system

Photoacoustic computed tomography (PAT) is based on using reconstruction algorithms to form an image by acquiring photoacoustic signals from a number of detector locations and using reconstruction algorithms to create tomographic images. Some of the first PAT systems used a single element ultrasound transducer scanned in circular trajectory. After a laser pulse, an ultrasound transducer (typically an unfocused transducer) will receive the acoustic pressure around the tissue where is absorbed the heat and result in thermal expansion. The acoustic pressure at location r and time t , is expressed in equation (2.12). In PAT, the unfocused ultrasound transducer, which is the detector, is usually scanned in spherical, cylindrical, and planar paths so that the initial acoustic pressure is enclosed by the detection surface. Figure 2.7 shows a typical PAT system, where an Nd:YAG laser is operated at 532 nm wavelength with a 6.5 ns pulse width and 10 Hz repetition rate to produce a tuneable dye laser [13]. The laser beam provides less than 10 mJ/cm² uniform incident fluence on the mouse head. An unfocused ultrasound transducer with 10.4 Hz center frequency, whose active aperture diameter is 2 mm, is placed in the water and scanned over the mouse head in a 3 cm radius circular motion to detect the emitted photoacoustic signals. The received photoacoustic signals by the unfocused ultrasound transducer are amplified and digitized for image reconstruction. In most PAT systems, the scanning is in a spherical fashion and the reconstruction algorithm is usually expressed as [14]

$$p_0(r) = \frac{1}{\Omega_0} \int_{S_0} \left[2p(r_0, t) - \frac{2t\partial p(r_0, t)}{\partial t} \right] \frac{\cos \theta_0}{|r - r_0|^2} dS_0 \quad (2.32)$$

Here, S_0 is the detection surface, p_0 is the initial acoustic pressure, Ω_0 is 2π when the scanning is in circular geometry, Ω_0 is 4π when the scanning is in either spherical or cylindrical geometry, and θ_0 represents the angle between the detection surface normal and the vector facing to the reconstruction point r [14]. This scanning contour involving the parameters in equation (2.32) is illustrated in figure 2.8 [14].

By applying the reconstruction algorithm expressed in equation (2.32), using a 10 MHz transducer, Y. W. Wang et al [13] permit imaging of the mouse brain with

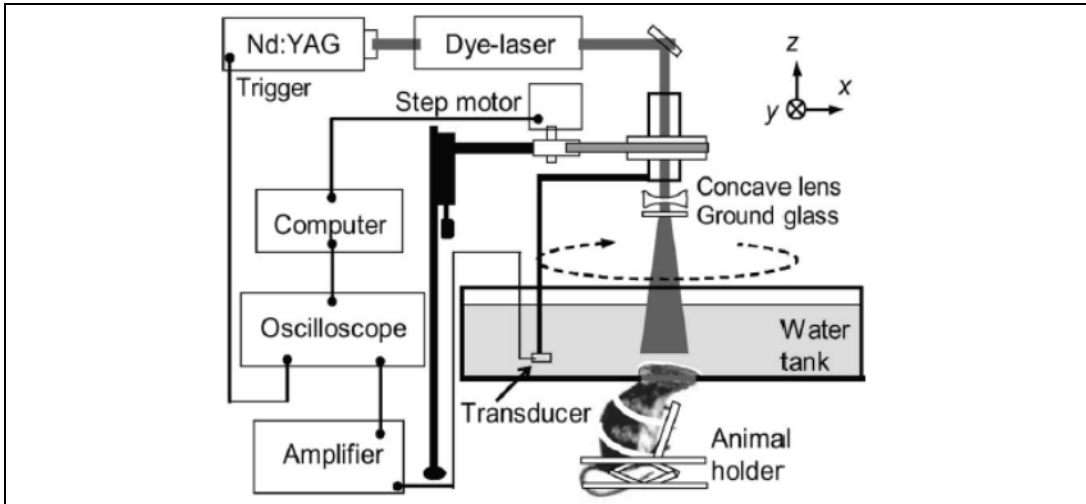


Fig.2.7. System diagram of PAT imaging system for imaging small animals [13].

approximately $60 \mu\text{m}$ in-plane spatial resolution and 2 mm out-of-plane spatial resolution.

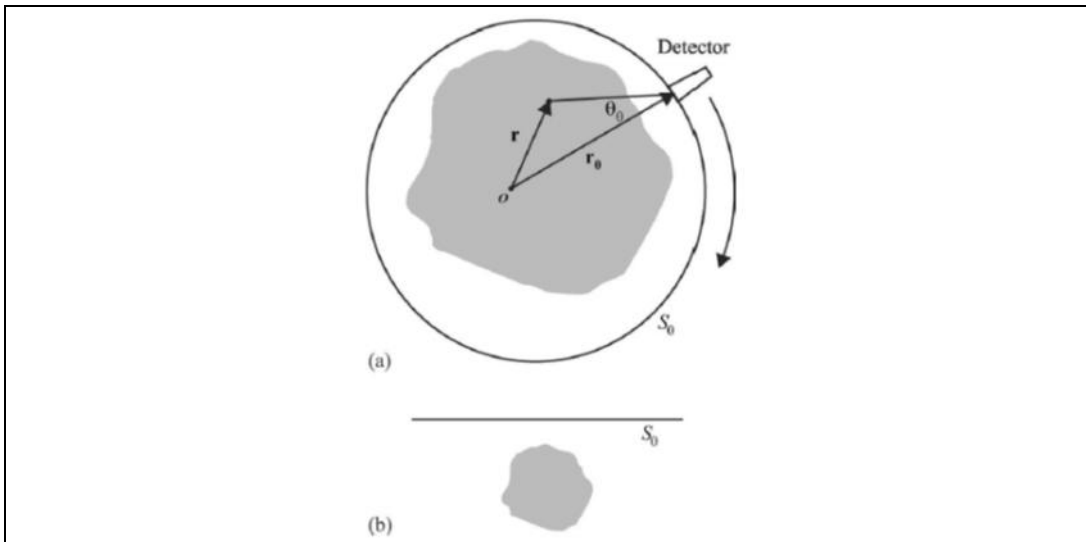
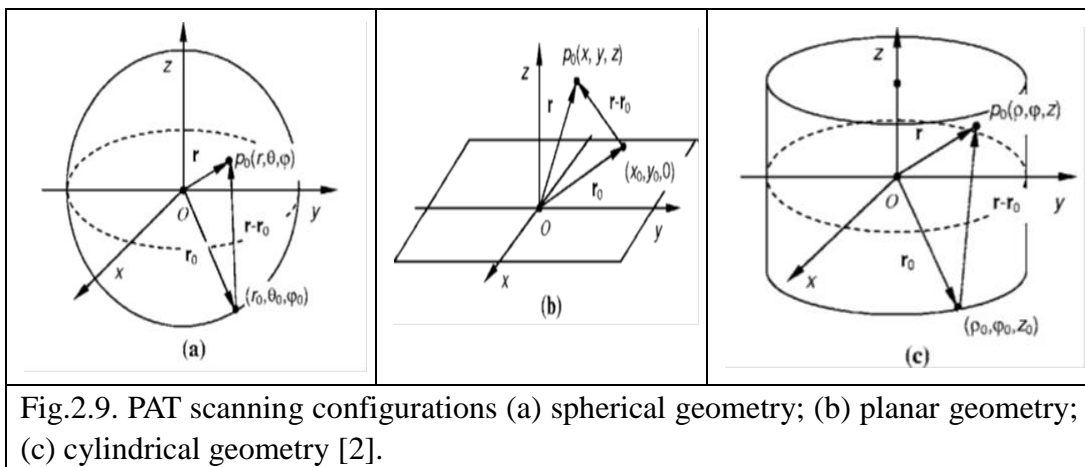


Fig.2.8. PAT system based on reconstruction algorithm (a) Spherical or cylindrical detection configuration; (b) Planar detection configuration [14].

2.4.4 Reconstruction algorithm for different geometry

Better out-of-plane resolution and 3-D imaging can be obtained by using transducers distributed on surfaces in 3D. Three types of scanning geometries: spherical, cylindrical and planar, which are shown in figure 2.9 were discussed in detail by M. Xu et al. [2]. Modified back projection and Fourier-domain reconstruction algorithms for such scanning configurations have been developed. Model-based reconstruction method where regularized matrix inversion is performed is a computationally burdensome approach to image reconstruction, but may offer some image quality advantages [15].



2.5 Application of photoacoustic imaging (literature review of PAI)

2.5.1 Application of PAT system

Recently, a research group has designed PAT system that could image at 5.2 cm depth and provided a resolution less than $780 \mu m$. The contrast of the image was improved by using Indocyanine Green (ICG) contrast agent, whose absorption peak was at the same level as the laser wavelength. This PAT system applied four ultrasound transducers to scan over the sample simultaneously to acquire data, balancing the image resolution quality and detection sensitivity. Only one of the ultrasound transducer was a concave transducer with a focal length of 3.2 cm and 3.5 MHz center frequency, the other three were flat ones with different frequencies. The laser system provided 15 ns near-infrared laser pulses with 800 nm wavelength at 10 Hz repetition rate. This near-infrared laser beam could penetrate deeply into the tissue. By using their PAT system, they have successfully imaged blood tube

samples embedded at 5 cm deep of chicken breast tissue with resolution less than $780 \mu\text{m}$. Therefore, they proposed that their PAT system could image vasculatures in the deep part of the breast or other organs [16].

Several groups have used PAT for *in vivo* structural imaging, such as brain and tumor imaging of small animals. The laser supply in X.D Wang et al. [17] was

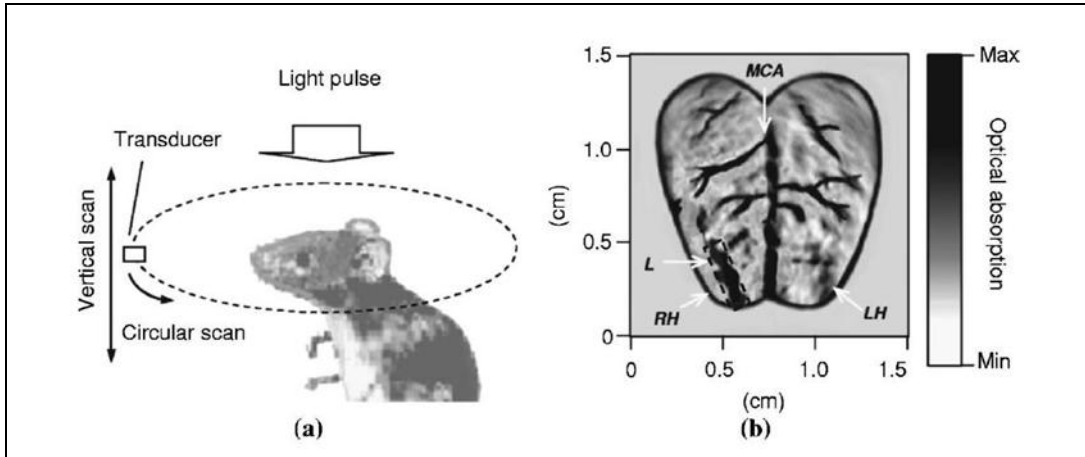


Fig.2.10. (a) Diagram of PAT system for imaging rat brain in a cylindrical scan; (b) Photoacoustic image of the cross-section of a rat brain [17].

Nd:YAG laser, which provided 532 nm wavelength with 6.5 ns pulse duration at 10 Hz repetition frequency. The blood vessels were imaged with high contrast at 1 cm

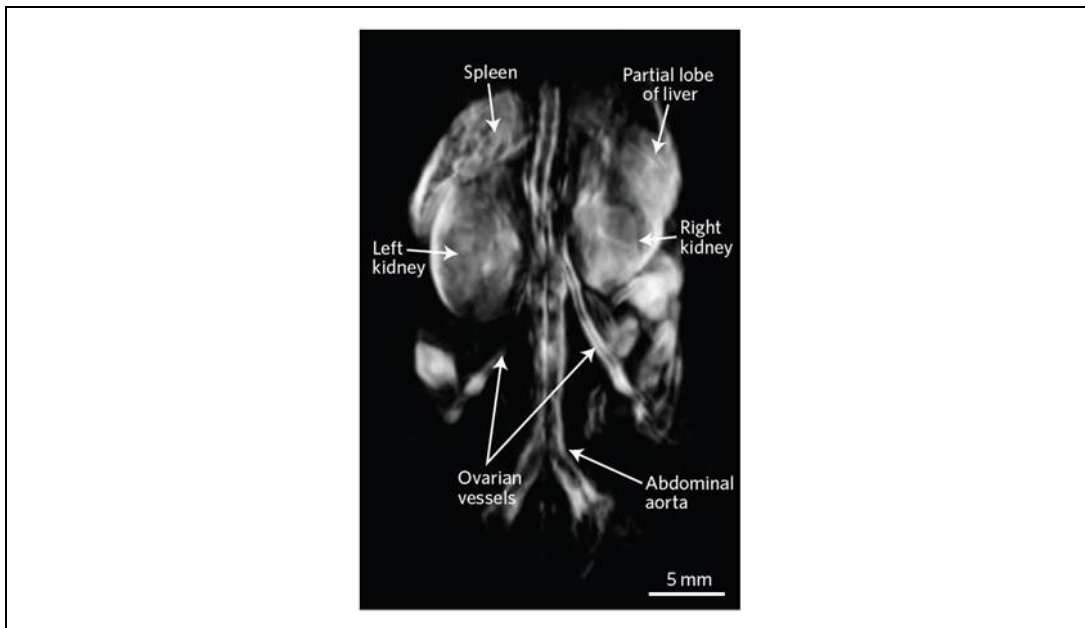


Fig.2.11. Whole mouse body *in vivo* image by PAT imaging technique [20].
depth by a 3.5 MHz high-sensitivity ultrasound transducer scanned in a circle over

a rat head. Other brain structures like cerebellum, hippocampus, and ventriculi lateralis were also imaged by a small aperture ultrasound transducer whose active element was 2 mm with 10.4 MHz center frequency with a 2.8 cm radius scan. Figure 2.10 shows an image of rat brain by using their PAT system [17].

Using the same PAT system, the brain tumors of the rat were also imaged by applying multiple laser wavelengths for function brain imaging [18]. Kruger's group designed a similar PAT system for body imaging of small animals. They used a Nd:YAG laser or tuneable optical parametric oscillator through a set of four fiber optic bundles to deliver the laser beam on the sample. This light source provided near infrared light which could help image deeper. They used a 128 elements arc array ultrasound transducer with a cylindrical surface of 40 mm radius of curvature. Each element dimension was $1.8 \times 2.0 \text{ mm}^2$ with 2.5 MHz peak response. By alternating the light wavelength between 800 nm and 1064 nm, vascular anatomy was studied based on the optical absorption ability of hemoglobin in the blood at different wavelength [19]. By combining with thermo-acoustic imaging technique, these PAT systems could also image breast cancer and help diagnose early stage cancer. This group also has constructed a whole mouse body *in vivo* image using their PAT system, as shown in figure 2.11 [20].

PAT is also used for molecular imaging based on exogenous contrast. Because the molecular imaging probes can be designed for sensing certain molecular biomarkers, such PAT systems can potentially accelerate molecular-targeted cancer therapeutic development [21]. Kruger's group has demonstrated in their PAT phantom experiments using a dual-wavelength subtraction method to measure 5 fmol of a near-IR (indocyanine green, ICG) in 1 μl volume [22]. Li hong Wang's group has found that indocyanine green polyethylene glycol (ICG-PEG) had a slower clearance rate than the traditional ICG near-IR dye [23]. Researchers have also discovered that gold nanoparticles [24] and/or nanoshells [25] became effectively new contrast-enhancing agents for *in vivo* PAT applications. Compared with other existing molecular imaging techniques, PAT uses nonionizing light sources and ultrasound detection to achieve relatively high sensitivity and spatial resolution. Researchers have applied deep penetrating high-resolution PAT systems for imaging reporter gene [26] lacZ expression in living rats [27] and dual-wavelength photoacoustic microscopy imaging of lacZ-marked tumors [28].

2.5.2 Application of PAM system

PAM systems in the literature can be divided into categories of dark-field illumination confocal PAM and high-frequency array-system based PAM systems.

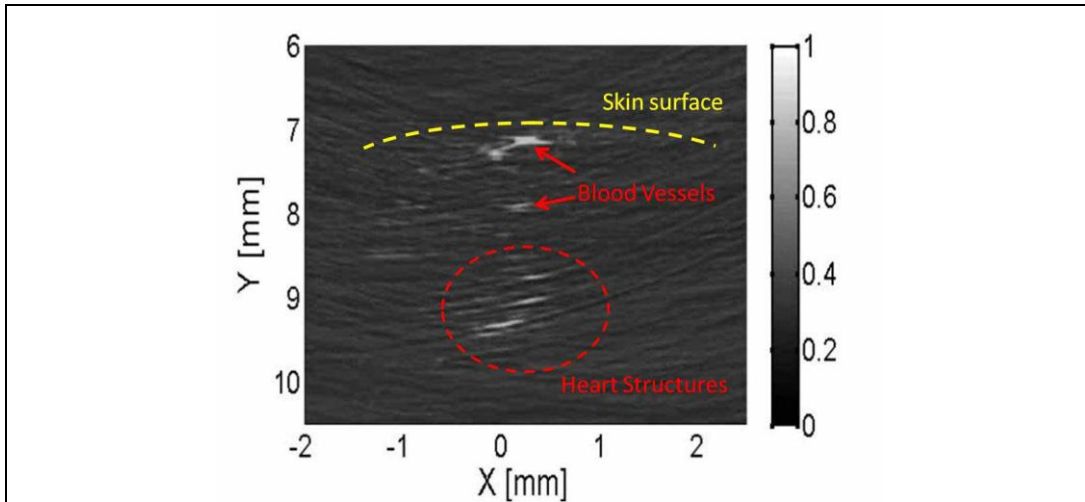


Fig.2.12. Photoacoustic image of microvascular structures in the upper thoracic region of a nude mouse [32].

Dark-field confocal PAM has been used to image microvascular structure, blood oxygen saturation, nanoparticle contrast agents extravasation and targeting, melanoma, tumor neovascularization. Future uses may include imaging in

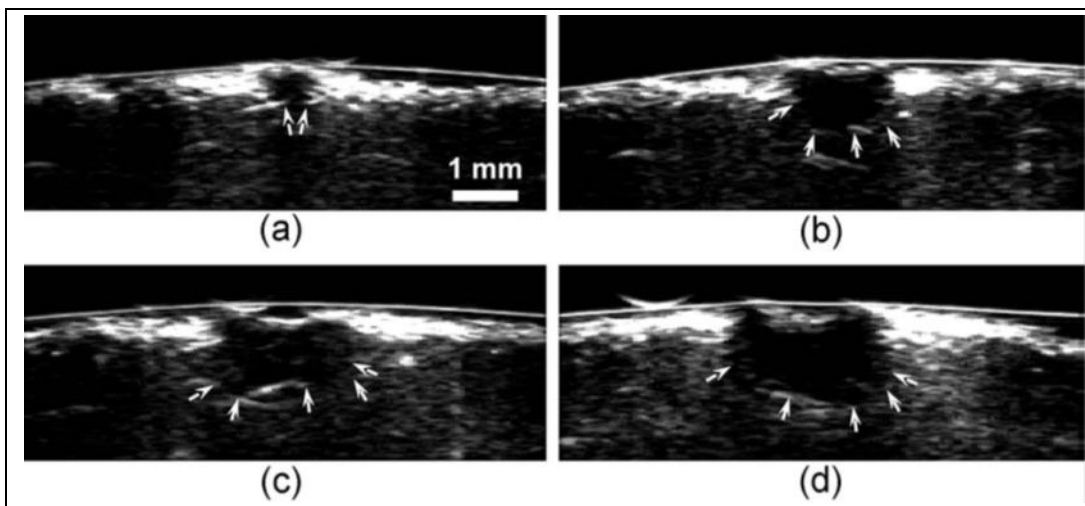


Fig.2.13. Photoacoustic images of serious skin burns at different depths by changing the burning durations (a) 5 s; (b) 10 s; (c) 20 s; (d) 30 s [33].

dermatological applications, intra-surgical applications including micro-vascular surgery, imaging pressure sores and the diabetic foot.

The first high-frequency array systems used for PAM were custom built and real-time imaging using a 30 MHz high linear array transducer as described by Zemp et al [29]. By applying dynamic receive beam-forming, no mechanical scanning is required. A 30 MHz linear array ultrasound transducer containing 48 elements with 100 μm pitch, which was fabricated from piezo-composite material, is used to receive the photoacoustic signals [30]. The piezo-composite material had high piezo-electric properties that highly improved its acoustic impedance. This system measured two 6 μm diameter carbon fibers to assess spatial resolution, measured as 72 μm lateral resolution and approximately 30 μm axial resolution. Using this system, the microvascular structures in the upper thoracic region of a nude mouse were imaged at the depth up to 3mm and real-time images were produced [31]. Figure 2.12 shows the result. Murine cardiac dynamics were also demonstrated at rates of 50 frames per second. [32].

Zhang et al. [33] applied PAM imaging to study the depth of acute thermal burns. This was accomplished by imaging the total concentration of hemoglobin in the blood accumulated at the injury boundaries because of the thermal burns. In their system, a 50 MHz ultrasound transducer with 40 MHz bandwidth whose numerical aperture was 0.44 was used to provide photoacoustic images with 45 μm lateral resolution and 15 μm axial resolution. A Nd:YAG pumped a tunable dye laser with 6.5 ns pulse duration at 10 Hz repetition rate. The optical wavelength was 584 nm, where the molar extinction coefficients of oxyhemoglobin and deoxyhemoglobin were identical at this wavelength. Figure 2.13 illustrates the PAM images of the skin burns at different depths. In this case, the optical absorption was only sensitive to the total concentration of hemoglobin, which helped to determine the thermal burn depth. By using this PAM system, it could detect and measure the acute thermal burn up to approximately 1.73 mm depth [33].

2.5.3 OR-PAM applications

Unlike traditional photoacoustic microscopy, optical resolution photoacoustic microscopy (OR-PAM) can provide photoacoustic images with high optical resolution rather than ultrasound resolution. It can achieve micrometer lateral resolution by focusing light into a tiny spot on the target. A research group has developed an OR-PAM system; they used objective lens to achieve a light focal spot of 3.7 μm . By imaging horse hair and carbon fiber, they have achieved photoacoustic images with lateral resolution of 5 μm and axial resolution of 15 μm . They also applied their system to image the microvascular structures in a nude mouse ear, as shown in figure 2.14 [34].

Edward. Z. Zhang et al. recently developed an OR-PAM system that also combined with PAT and OCT imaging modes. They used an ultrasound sensor made by Fabry-Perot (FP) polymer film. By imaging carbon fibers with 7 μm diameter, they have demonstrated that the lateral resolution in OR-PAM mode is around 7 μm and the axial resolution is 10 μm . The FP polymer film of the ultrasound sensor allows more optical imaging modes based on its transparent property [35]. Takashi Buma's group has developed an OR-PAM system by using a highly repetitive

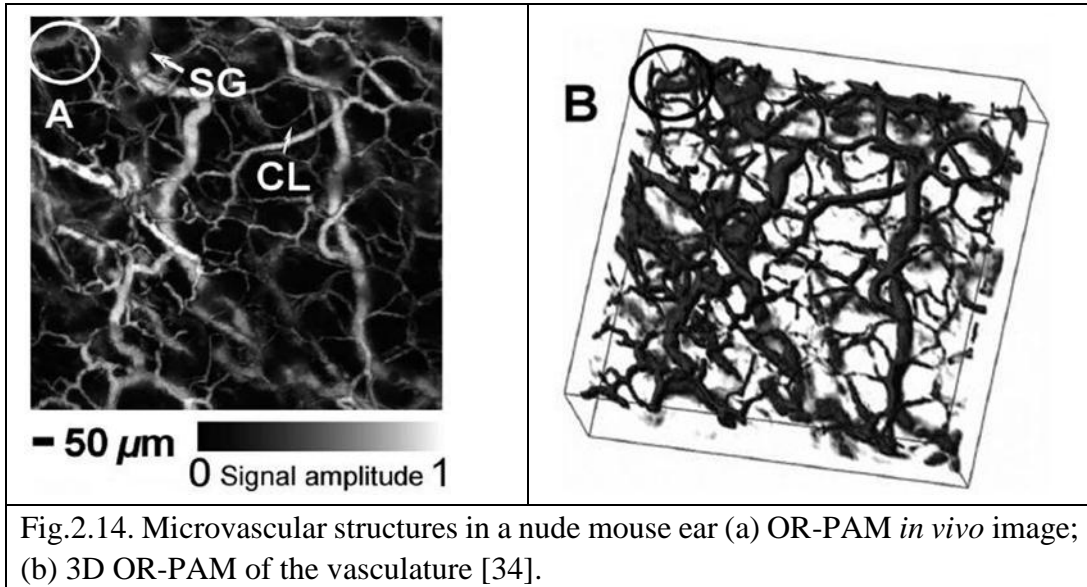


Fig.2.14. Microvascular structures in a nude mouse ear (a) OR-PAM *in vivo* image; (b) 3D OR-PAM of the vasculature [34].

pulsed optical source. At 1064 nm wavelength, their Q-switched Nd:YAG microchip laser generates 0.6 ns pulse duration with energy of 8 μJ and at 6.6 KHz pulse repetition rate. With such optical source with rapid wavelength tuning ability, their group has improved the acquisition speed of their OR-PAM system [36].

In our group, my colleagues have developed a real-time OR-PAM system with special designed handheld probe (HH-OR-PAM), including fast scanning mirrors, an image guide with 30,000 fiber pixels, a refocusing lens and a custom probe to reduce the footprint. They applied the HH-OR-PAM system to image the microvasculature in a mouse ear and achieved approximately 7 μm lateral resolution. They have improved the usability of traditional OR-PAM system so that their system can have more clinical applications [37].

The same group in our lab have also designed a fiber-based optical-resolution photoacoustic microscopy (F-OR-PAM) system, based on image guide fibers and a

unique fiber laser system. The image guide fibers included 30,000 single fibers bundled together in 800 μm diameter to provide high optical resolution laser spot. This system allows label-free real-time *in vivo* photoacoustic microscopy imaging with such feasibility for the first time [38]. They also developed an OR-PAM system with combination optical sources of passively Q-switched fiber laser and microchip laser. After phantom experiments, their system achieved approximately 15 μm lateral resolution with the fiber laser and approximately 7 μm with the microchip laser [39]. In 2011, my colleagues have upgraded the OR-PAM system with a high-repetition-rate nanosecond fiber-laser source to improve the overall acquisition speed. They used a diode-pumped nanosecond-pulsed Ytterbium-doped 532 nm fiber laser with pulse repetition rate up to 600 kHz. Using fast-scanning mirrors, they have demonstrated 3D and C-scan images of capillary-scale microvasculature of live mouse ear with more than 4 frames per second (fps) acquisition frame rate and achieved approximately 6 μm lateral resolution [40].

2.5.4 Flow imaging and oxygen metabolism:

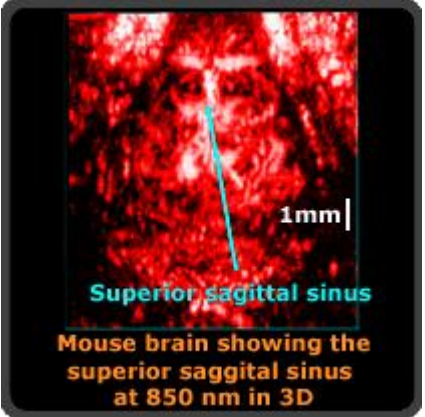
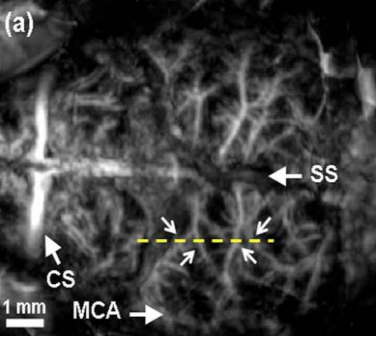
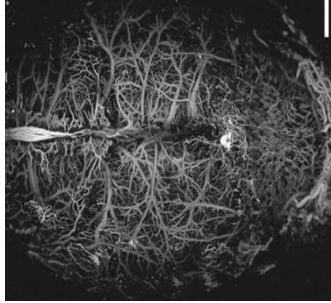
Progress is currently being made to use photoacoustic imaging for flow estimation. These methods are based on the photoacoustic Doppler effect. Most of the progress *in vivo* has been with OR-PAM at superficial depths, although others are investigating deeper penetration applications. The ability to measure both flow and blood oxygenation is leading to oxygen consumption estimation with OR-PAM systems. Our group is developing ultrasound flowmetry techniques combined with photoacoustic oxygen saturation methods to estimate oxygen flux and oxygen metabolism [41,42].

2.5.5 Optical property estimation:

Photoacoustic image contrast is primarily due to optical absorption. Quantitative estimation of optical properties is challenging because subsurface laser fluence is unknown and function of the unknown optical properties. Little information is directly available regarding optical scattering. A number of papers in the literature are trying to augment the non-quantitative absorption information of photoacoustic imaging with techniques for quantitative absorption and scattering estimation. Dr. Roger Zemp was involved in one experimental technique in our group, first-authored by J. Ranasinghesagara which involved a photoacoustic method for estimating optical scattering coefficients. Other works in the literature include multi-spectral methods, multiple-illumination methods, and various inverse

problems for quantitative estimation of optical properties [43]. These are ongoing research problems that have not fully been solved.

2.6 Motivation to use high-frequency annular arrays

		
<p>Mouse brain image acquired using VisualSonics system (high frequency linear array transducer with fiber-based light delivery).</p>	<p>Photoacoustic Microscopy image acquired using high-numercial aperture transducer (from Lihong Wang's group [44]).</p>	<p>Optical-Resolution PAM image of the brain cortex. (from Lihong Wang's group [44]).</p>
<p>Fig.2.15. These images are meant to illustrate the potential for improvement in the current image quality available using the VisualSonics system. We believe we can even attain further improved image quality by development of high numerical aperture annular arrays. We aim to achieve this in a form factor readily supported by VisualSonics [44].</p>		

The highest-quality acoustic-resolution photoacoustic images reported to date have been formed using a single-element high-frequency ultrasound transducers. While this method has slow image acquisition due to one laser pulse per A-scan being required, image quality is significantly higher than linear array-based systems. To illustrate this consider figure 2.15 which shows images of a mouse brain acquired using a commercial linear-array-based photoacoustic imaging system from VisualSonics, a dark-field confocal PAM system, and an OR-PAM system.

The highest image quality of the cortical surface vessels is seen from the OR-PAM system but this required removal of the scalp and thinning the skull,

whereas the other techniques did not. This is because the OR-PAM system is limited to imaging depths of ~ 1 transport mean-free path (~ 1 mm in tissue).

Some reasons that dark-field confocal PAM provides better-quality images compared to the linear array-system based image include the lack of high-NA elevational focusing of such linear arrays. Another reason may be due to smaller sensor elements leading to lower signal-to-noise ratio. Even in-plane focusing is electronically limited to f-numbers of about 2 for the linear arrays, whereas much lower f-numbers (higher NAs) are possible with single-element transducers with mechanically machined lenses or surfaces. Additionally, linear array element pitch is not always as small as may be desired, and this can lead to grating lobes. When element count is low, sidelobes are worse. High-frequency array transducers have only recently been commercialized due to fabrication challenges. Additional reasons why image quality is higher for dark-field confocal PAM may include illumination. Rough optical focusing is achieved with PAM whereas with the array-based system, illumination is over a large area, worsening off-axis clutter and signals away from the desired electronic focus.

While image quality of PAM using single-element focused transducers has been higher than array-system image quality, depth-of-field of array-based systems is superior to focused single element transducers. We would like the dynamic depth-of-field advantages of arrays while enjoying the high resolution and image quality of high-NA, high-frequency focused single element transducers.

High-frequency annular arrays are investigated in this thesis as a candidate technology to realize these desired improvements. They offer the promise of hybrid geometrical and electronic focusing for high numerical aperture imaging, yet with dynamic focusing. They also offer isotropic lateral spatial resolution, and can accommodate dark-field confocal illumination. It is noteworthy that one of the first patents on photoacoustic imaging used annular array transducers; however, these discussed low-frequency annular arrays with little or no geometric focusing. Our proposed work aims to develop high-frequency annular arrays for high-resolution photoacoustic imaging. More about annular arrays and their potential improvements will be discussed in subsequent chapters.

Ch3: Background on Ultrasound and Transducers (including annular array)

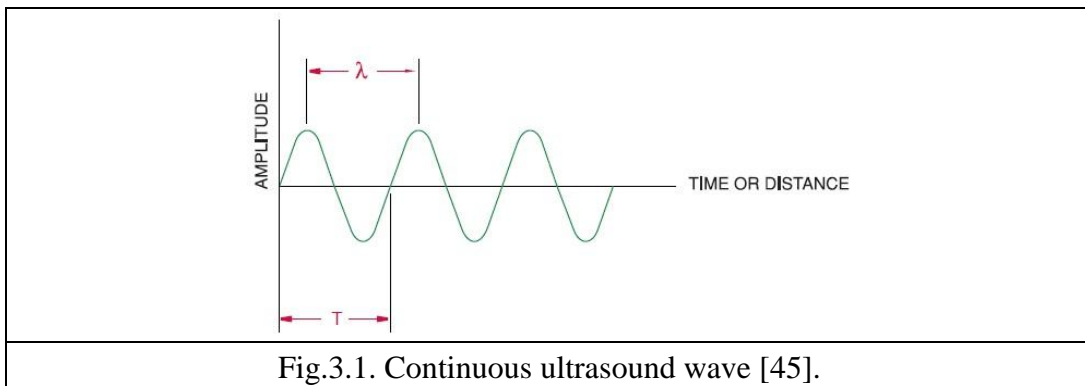
3.1 Introduction of ultrasound

3.1.1 Physical principles

Unlike audible sound, ultrasound has a much higher frequency and a shorter wavelength. For audible sound, the frequency range is below 20 kHz. For diagnostic ultrasound, the frequency range is typically between 1 to 12 MHz. For high resolution, low penetration ultrasound imaging, ultrasound frequencies are typically in the range of 20 MHz to 100 MHz. Ultrasound is often used for non-destructive imaging of tissues for medical and diagnostic purposes.

Ultrasound has two general wave propagation forms. One is the longitudinal wave, where the particle and the wave propagate in the same direction. The other one is shear wave, where the particle motion is perpendicular to the propagation direction.

Ultrasound waves have some fundamental parameters, such as propagation frequency, wavelength, velocity, and period. Figure 3.1 shows a continuous ultrasound wave contained information of wavelength and period [45]



The relationship among material sound velocity c , frequency f , wavelength λ , and period T is expressed in the following equations [45].

$$f = \frac{1}{T} \quad (3.1)$$

$$\lambda = \frac{c}{f} \quad (3.2)$$

There are many definitions to describe intensity. Most generally the intensity of ultrasound is the amount of power per unit area, in units of watts per square

centimetre. A commonly used metric of intensity is the spatial peak temporal average intensity, described as the maximum value of intensity for an averaged ultrasound beam over the pulse repetition period [46]. It is also useful to express intensity in a relative manner in units of decibels ($10 \log$ Intensity, dB) [47]

$$\text{Relative Intensity (dB)} = 10 \log \frac{I_2}{I_1} \quad (3.3)$$

The amplitude of ultrasound wave relates to the initial energy of the ultrasound pulse. This is controlled by the pulse generator connecting with the ultrasound transducer. It can set different amplitude level for different imaging purpose. For ultrasound imaging application, it is important to know the relative amplitude of ultrasound pulses. As an ultrasound wave travels through tissue with certain thickness, its amplitude decreases gradually. The relative amplitude can be expressed [47]

$$\text{Relative amplitude (dB)} = 20 \log \frac{A_2}{A_1} \quad (3.4)$$

Since ultrasound intensity is directly proportional to the square of pressure amplitude, this brings a factor of 2 in the log scale.

3.1.2 Characteristics of ultrasound

When ultrasound wave travels in a medium, the velocity is given by the expression [48]

$$c = \sqrt{\frac{1}{k\rho}} \quad (3.5)$$

Here, k is the medium compressibility, and ρ is the medium density. For a medium, the acoustic impedance is given by [48]

$$Z = \rho c \quad (3.6)$$

When the particles of ultrasound wave travel in a medium, their displacement can cause a pressure wave, which for a plane wave is expressed as [45]

$$p(t, z) = p_0 e^{j\omega(ct-z)} \quad (3.7)$$

Here, p_0 is the pressure amplitude in excess of the atmospheric pressure, and ω is the wave number. For a plane continuous wave, the ultrasound intensity is the average energy flowing through a medium per unit area, and it is perpendicular to the wave propagation direction, defined by [48]

$$\vec{I} = \frac{p_0^2}{2Z} \quad (3.8)$$

As mentioned previously, when ultrasound wave travels through a medium, it constantly loses energy and its amplitude reduces because of absorption and scattering in the medium. The higher the frequency is, the higher the absorption will be [31]. For human tissue, the general attenuation scale is in the range of approximately 0.3 to 1dB/cm/MHz^{1.1} [48]. The attenuation factor also affects the ultrasound imaging depth and the frequency range. For most soft tissues, the frequency dependent attenuation coefficient is defined by [48]

$$\alpha = \alpha_0 f^n \quad (3.9)$$

Here, α_0 is the temperature-dependent factor, f is the frequency and n is the range from 1 to 2. Therefore, the ultrasound plane wave intensity expressed in equation (3.8) can be expressed with attenuation coefficient as [48]

$$\vec{I}(z) = \frac{p_0^2}{2Z} e^{-2\alpha z} \quad (3.10)$$

When ultrasound waves meet the interface or boundary of two media with different acoustic properties, waves are reflected and/or transmitted. Transmitted waves may also be refracted. The reflection and refraction of an incident ultrasound wave are illustrated in figure 3.2. The angle of incidence and reflection are the same, and the refracted waves are related to the incident angle by Snell's law. These relationships are expressed as [48]

$$\theta_i = \theta_r \quad (3.11 \text{ a})$$

$$\frac{\sin \theta_i}{\sin \theta_t} = \frac{c_1}{c_2} = \frac{\lambda_1}{\lambda_2} \quad (3.11 \text{ b})$$

Here, θ_i is the incident angle, θ_r is the reflected angle; c_1 and c_2 are ultrasound wave propagation velocities in two different mediums respectively. The critical angle is expressed below, where the incident ultrasound wave is totally reflected with no refraction or transmission [48].

$$\theta_{ci} = \sin^{-1}\left(\frac{c_1}{c_2}\right), c_2 > c_1 \quad (3.12)$$

Usually, the reflected ultrasound signal contains the object information, and the brightness of the ultrasound image is proportional to the reflection or echo strength. This also depends on difference between the acoustic impedance of the two mediums. This can be expressed as the amplitude ratio between the reflected

and incident ultrasound pulse regarding to the acoustic impedance values of the two mediums [47].

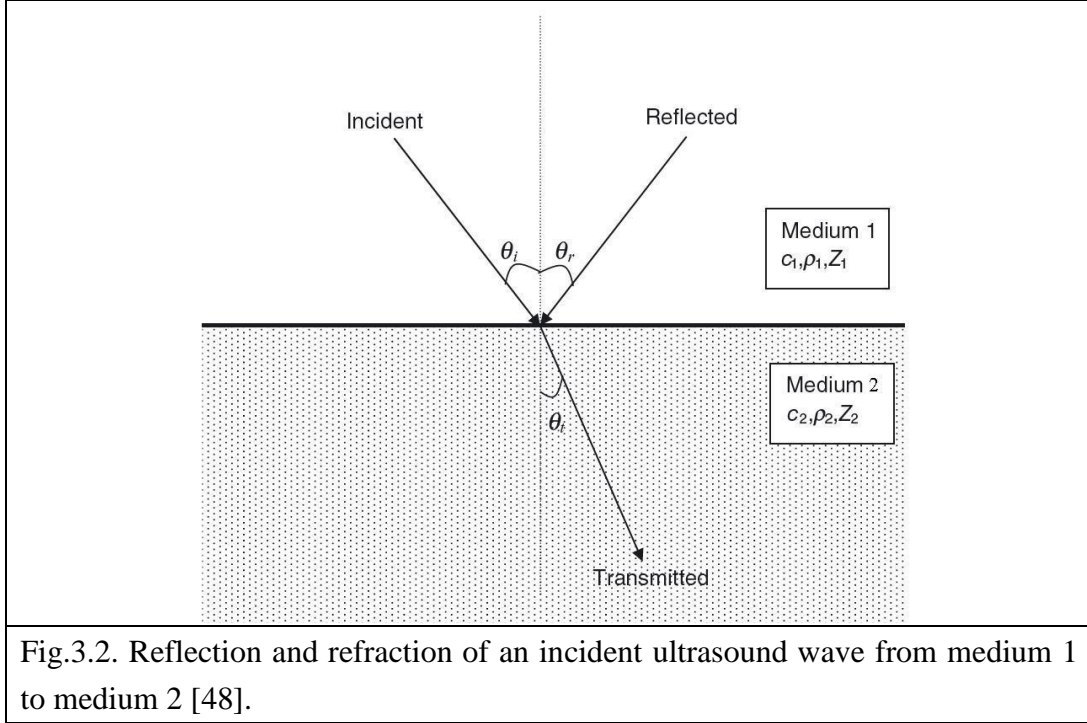


Fig.3.2. Reflection and refraction of an incident ultrasound wave from medium 1 to medium 2 [48].

$$\text{Reflection loss (dB)} = 20 \log\left(\frac{Z_2 - Z_1}{Z_2 + Z_1}\right) \quad (3.13)$$

Here, Z_1 and Z_2 are the acoustic impedances of the two mediums. The pressure reflection coefficient or reflection coefficient is expressed as [48]

$$R = \frac{P_r}{P_i} = \frac{Z_2 \cos \theta_i - Z_1 \cos \theta_t}{Z_2 \cos \theta_i + Z_1 \cos \theta_t} \quad (3.14)$$

Here, p_i and p_r are incident and reflection ultrasound wave pressure. The pressure transmission coefficient is given by [48]

$$T = \frac{2Z_2 \cos \theta_i}{Z_2 \cos \theta_i + Z_1 \cos \theta_t} \quad (3.15)$$

If the incident ultrasound wave is perpendicular to medium 2, meaning the incident angle is zero, then both the reflection and transmission coefficients become [48]

$$R_{1,2} = \frac{Z_2 - Z_1}{Z_2 + Z_1} \text{ and } T_{1,2} = \frac{2Z_2}{Z_2 + Z_1} \quad (3.16)$$

Here, $R_{1,2}$ is the reflection from medium 2 to medium 1, and $T_{1,2}$ is the transmission from medium 1 to medium 2.

By using equations (3.14) and (3.15), the intensity reflection and transmission coefficients are expressed as [46]

$$R_I = \frac{I_r}{I_i} = R_P^2 = \frac{(Z_2 \cos \theta_i - Z_1 \cos \theta_t)^2}{(Z_2 \cos \theta_i + Z_1 \cos \theta_t)^2} \quad (3.17 \text{ a})$$

$$T_I = 1 - R_I = \frac{4Z_2 Z_1 \cos^2 \theta_i}{Z_2 \cos \theta_i + Z_1 \cos \theta_t} \quad (3.17 \text{ b})$$

3.2 Introduction of transducers

An ultrasound transducer is a device that can generate and receive ultrasound. There are various technologies for creating ultrasound transducers, such as capacitive micromachined ultrasonic transducers (cMUTs) and piezoelectric transducers. Compared with piezoelectric transducers, cMUTs have a number of advantages. It is easier to produce cMUTs by using batch production method using a standard IC process to meet all the parameter specifications [49]. By using photolithographic techniques, cMUTs ensure cheap and accurate manufacturing at high frequencies [50]. cMUTs are not only more easily integrated with electronics, but are also easier to combine into transducer arrays [49]. They have a wider operating temperature range, larger relative bandwidths, and have better acoustic

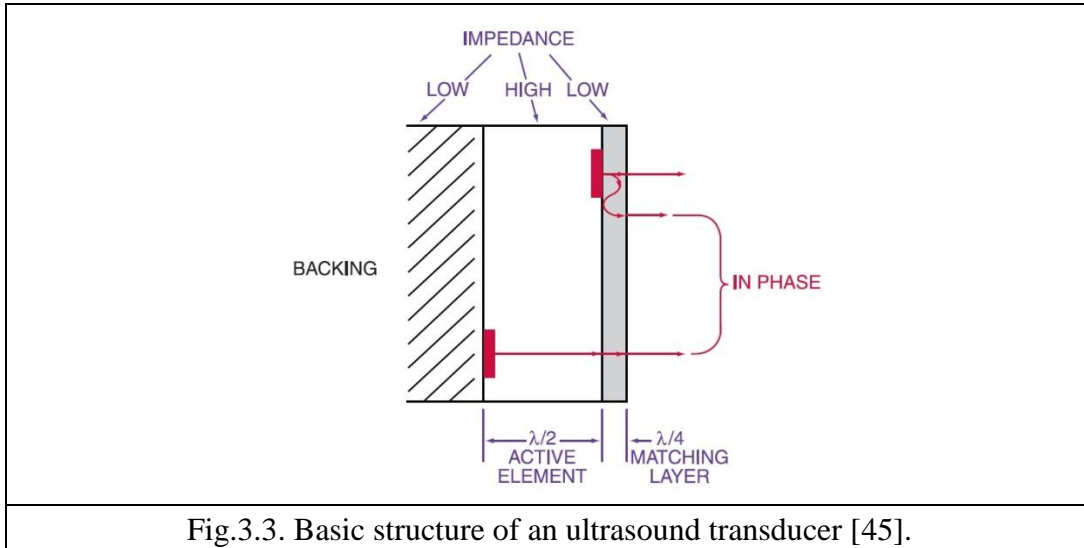


Fig.3.3. Basic structure of an ultrasound transducer [45].

impedance matching between air and water [50]. Since cMUTs have so many advantages over piezoelectrics, they have recently drawn more attention with more research conducted to improve their quality.

Piezoelectric materials are dominantly used to fabricate ultrasound transducer in practice. For our project, we choose to use polyvinylidene flouride (PVDF) piezoelectric material to fabricate a high frequency annular array ultrasound transducer. PVDF allowed us to form the front aperture of the piezoelectric material into a concave shape in order to achieve dynamic focusing and improve the imaging depth of field.

A pulse generator is used to provide the transducer excitation signals to generate an acoustic waveform. The ultrasound transducer converts the received convert mechanical oscillations (ultrasound waveform) into an electrical signal. This signal is then processed into an ultrasound image. There are three main parts of a piezoelectric ultrasound transducer structure: the active element, backing and the matching layer. This basic structure of a piezoelectric ultrasound transducer is shown in figure 3.3 [45].

The active element is the piezoelectric material. Piezoelectric material deforms when exposed to an electric pulse which produces an acoustic wave, and generates an electrical signal when its shape changes due to the reception of an acoustic wave. There are many types of piezoelectric materials with different properties, such as piezoelectric ceramics, piezoelectric polymers and composites.

The backing material chosen will affect the transducer characteristics and varies from air to high density material providing extensive acoustic attenuation which is used to absorb energy from the back of the active element. If the acoustic impedances of the active element and the backing material are the same, then the ultrasound transducer can provide good resolution images with lower signal strengths. If the acoustic impedance of the active element and the backing material are significantly different, then the ultrasound transducer has a higher signal strength and sensitivity, but poor resolution due to reverberations in the active elements [45].

The matching layer of an ultrasound transducer is not always necessary. If the acoustic impedance of the ultrasound transducer active element matches the impedance of the medium, then there is no need for a matching layer. The thickness of the matching layer is chosen to match the phase of the ultrasound waves generated from the active element and the reverberated waves from the matching layer. For a matching layer with a quarter-wavelength thickness, the matching layer impedance is expressed as $Z_{Match} = \sqrt{(Z_{Transducer}Z_{medium})}$ [45].

When ultrasound transducers generate ultrasound beams, there is a near-field transmission region and far-field transmission region. For unfocused and focused ultrasound transducers, their ultrasound beam diameters are different. A focused ultrasound transducer can produce a more focused beam or beam with smaller diameter, providing greater image resolution. For an unfocused ultrasound transducer, the beam diameter is relatively the same as the diameter of the active element in the near field, and the beam starts to diverge in the far field, resulting in larger beam diameter and less beam intensity on the central axis. Figure 3.4 illustrates the ultrasound beam configuration for both unfocused and focused ultrasound transducers [47].

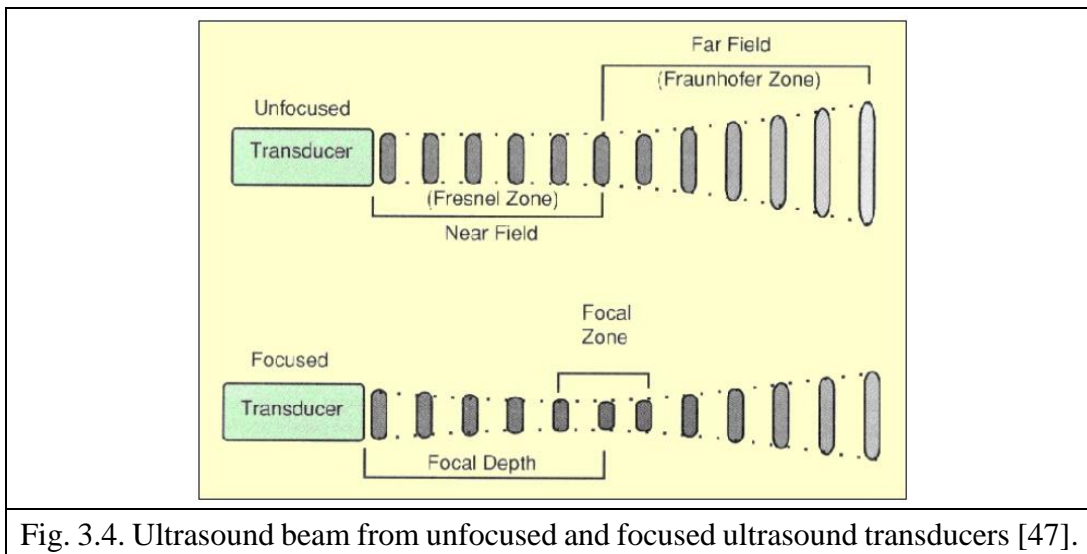


Fig. 3.4. Ultrasound beam from unfocused and focused ultrasound transducers [47].

The length of the near-field transmission region relates to the radius of the ultrasound transducer active aperture and its wavelength, which is expressed as [48]

$$L_{nf} = \frac{r^2}{\lambda} \quad (3.18)$$

The divergence angle of the far-field transmission region is given by [48]

$$\theta = \sin^{-1}\left(\frac{0.61\lambda}{r}\right) \quad (3.19)$$

3.2.1 Field profile analysis for circular ultrasound transducers

Under appropriate boundary conditions, the acoustic radiation at location r and time t , is expressed in terms of velocity potential $\varphi(r, t)$ [51].

$$\nabla^2 \varphi(r, t) - \frac{1}{c^2} \frac{\partial^2 \varphi(r, t)}{\partial t^2} = 0 \quad (3.20)$$

The acoustic pressure expression can be determined from equation (3.20), which is given by [51]

$$p(r, t) = \rho_0 \frac{\partial \varphi(r, t)}{\partial t} \quad (3.21)$$

Here, ρ_0 is the equilibrium density.

At the piston transducer surface, the time-varying velocity is known. By using the Green's function $g(|r - r_0|, t)$ of [a simple harmonic motion], the velocity potential is expressed as [51]

$$\varphi(r, t) = \int_0^t v(t_0) dt_0 \int_S g(|r - r_0|, t) dS = v(t) * h(r, t) \quad (3.22)$$

Here, $v(t)$ is the piston transducer surface average velocity; $h(r, t)$ is the impulse response, and * denotes temporal convolution. The impulse response function relates to both boundary conditions and ultrasound transducer geometry. By using the Green's function, the impulse response is given by [51]

$$h(r, t) = \int_S g(|r - r_0|, t) dS \quad (3.23)$$

Based on equations (3.21) and (3.22), the acoustic pressure is modified as [51]

$$p(r, t) = \rho_0 \frac{\partial}{\partial t} (v(t) * h(r, t)) = \rho_0 \frac{\partial}{\partial t} v(t) * \frac{\partial h(r, t)}{\partial t} \quad (3.24)$$

For focused single element transducer, the lateral resolution can be defined as the full width at half maximum, and is expressed as [5]; here a is the focal length and D is the aperture diameter. Figure 3.5 shows the relationship of focal length and aperture of a concave ultrasound transducer; the red dot line is the focal length and the blue line represents the aperture size of the transducer.

$$FWHM = 1.4\lambda \frac{\text{Focal Length}}{\text{Aperture}} = 1.4\lambda \frac{F}{D} \approx 1.4\lambda \frac{a}{D} \quad (3.25)$$

In order to distinguish two close point sources, it is useful to introduce the Rayleigh resolution expression [5]

$$R_L = 1.22\lambda \frac{\text{Focal Length}}{\text{Aperture}} \approx 1.22\lambda \frac{a}{\mathcal{D}} = 1.22\lambda \times f_{\text{number}} \quad (3.26)$$

Here, $f_{\text{number}} = \text{Focal Length}/\text{Diameter}_{\text{aperture}}$, and the numerical aperture (NA) = $1/(2f_{\text{number}})$

The axial resolution of an ultrasound transducer is inversely proportional to the transducer bandwidth.

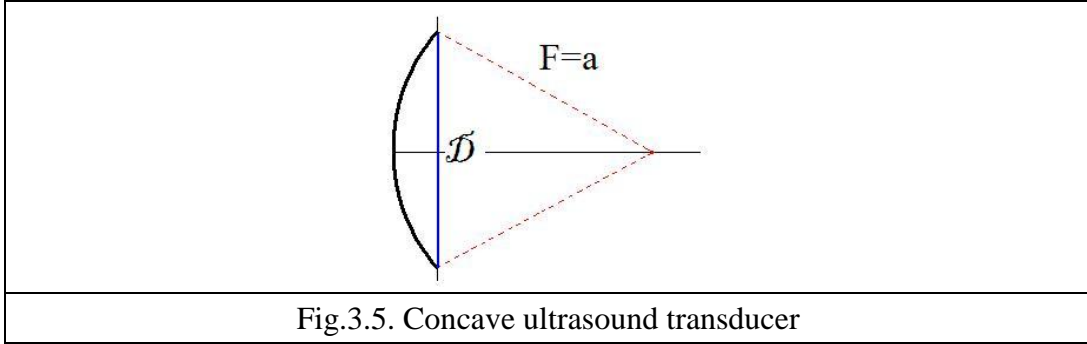


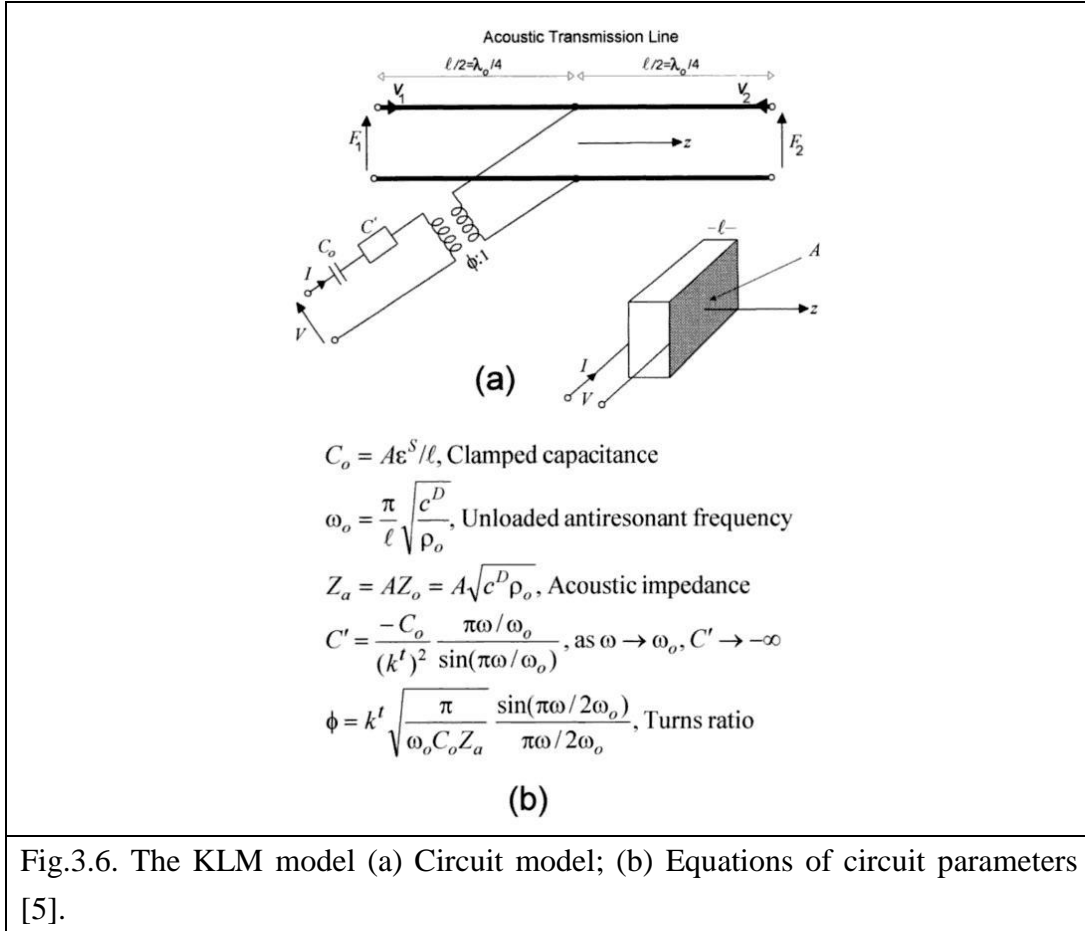
Fig.3.5. Concave ultrasound transducer

Depth of field is a very important factor in ultrasound imaging, which is defined as the maximum range to maintain acceptable image quality between the closest to the farthest objects in view. It is also a measure of partial imaging depth where the transducer keeps relatively strong focusing power. For single-element focused transducers, the depth-of-field is limited due to a single focus. To improve the depth-of-field, we propose to design an annular array concave ultrasound transducer and apply dynamic receive beam-forming method to increase the depth of field while maintaining good focusing power. With a concave aperture, signals from all these annuli can be delayed and summed using a dynamic receive beam-forming algorithm to increase the depth-of-field. The depth-of-field of an ultrasound imaging system with a given fixed f-number can be defined as the 3 dB pressure response on the axial (depth) axis [5]

$$Z_F(3dB) \approx \frac{1.8\lambda}{\sin^2\theta_T} = 7.2\lambda \times (f_{\text{number}})^2 \quad (3.27)$$

3.2.2 Equivalent electrical circuit models

A number of equivalent circuit models have been developed to describe the electrical and mechanical aspects of transducers as transmitters and receivers. The KLM model is among the most widely used models of piezoelectric transducers



and is illustrated in figure 3.6 [5]. It is constructed with two quarter-wave acoustic transmission lines and the two common terminals connect to the transformer. The KLM model can interpret different termination condition effects at the two acoustic terminals and can optimize the ultrasound transducer over performance.

The KLM model helps determine the input impedances of the piezoelectric transducer and the matching layer using the model parameters. Using the KLM model, for an ultrasound transducer with Z_B as the backing region acoustic impedance and Z_T as the transmission region acoustic impedance, the radiation resistance of the equivalent circuit is defined as [5]

$$R_{ao} = \frac{2(k^t)^2}{\pi^2 f_0 C_o} \frac{Z_a}{Z_B + Z_T} \quad (3.28)$$

Here, k^t is the piezoelectric coupling factor, and Z_a is acoustic impedance of the piezoelectric material. If the backing region is air ($Z_B = 0$) and there is a quarter-wave matching layer, the acoustic impedance of the piezoelectric material and the transmission region is the same, the acoustic impedance of the matching layer is $Z_M = \sqrt{(Z_T Z_a)}$ and the radiation resistance becomes [5]

$$R_{ao} = \frac{2(k^t)^2}{\pi^2 f_0 C_0} \quad (3.29)$$

3.3 US imaging: A-scan, B-scan, C-scan systems

3.3.1 A-scan system

A-scan systems were first used during the development of Radar, when a pulse-echo signal was displayed on an oscilloscope. It is often a single line that presents the signal amplitude over time or distance. A-scan often refers to amplitude scan, meaning the scan result shows the echo signal amplitude in one dimension. After an ultrasound beam is transmitted to a point target, the reflected pulse is received and looks like a spike with a certain height on the oscilloscope. The height of the vertical reflection or spike is determined by the intensity of the received pulse and the distance between two vertical reflections is determined by the total transmitting and receiving time. The amplitude of the signal is related to the acoustic impedance of the material and how much energy is absorbed. It is used to detect the flaws in materials and measure the thickness or depth of the material. In ultrasound imaging, an A-scan system can detect midline tissue structures in the brains, such as falx cerebri and the third ventricle [52].

3.3.2 B-scan system

By scanning an ultrasound beam over an area in a linear fashion, a sequence of A-scan lines can construct a 2-D image which is referred to as the B-scan mode. B-scan stands for brightness scan, and each bright spot indicates the amplitude of each echo signal at different scan location. The time delay from transmitting to receiving ultrasound pulses determines the lateral reflection depth position. The ultrasound transducer aperture position determines the horizontal position. In order to quickly produce a sequence of B-scan displays, the ultrasound beam is scanned repeatedly in a very fast manor. Usually, the ultrasound transducer is mounted on a mechanical scanning stage. For different parts of the imaged tissue, the received ultrasound pulses have different brightness scales based on the different received intensities. The resulting shades of grey can provide structural

information of the internal organ tissues, and is called a gray scale display. In the gray scale ultrasound B-scan image, the white and black show the solid and liquid structures accordingly. In order to improve B-scan image quality, the ultrasound beam is scanned from different angles and the received signals are combined through an averaging process to reduce image artifacts [52]. B-scan image quality can be improved by applying a time-varying gain factor on the received ultrasound signals to compensate for depth-dependent attenuation.

Phased array systems have also been applied for constructing B-scan images. When the phase array system is used for pipeline inspection, it has better capability to recognize different complicated types of defects and detects cracks. In this system, the transducer contains many individual elements that can be electrically operated separately. These elements can be pulsed in different time and the delays between each element are precisely controlled. This results in the creation of beams with different angles, different focal length, and different focal spot size. Figure 3.7 shows the resulting different wave-fronts by applying different delays to the elements. The B-scan images are constructed based on reconstruction of the acquired data according to the different beam angle, focal

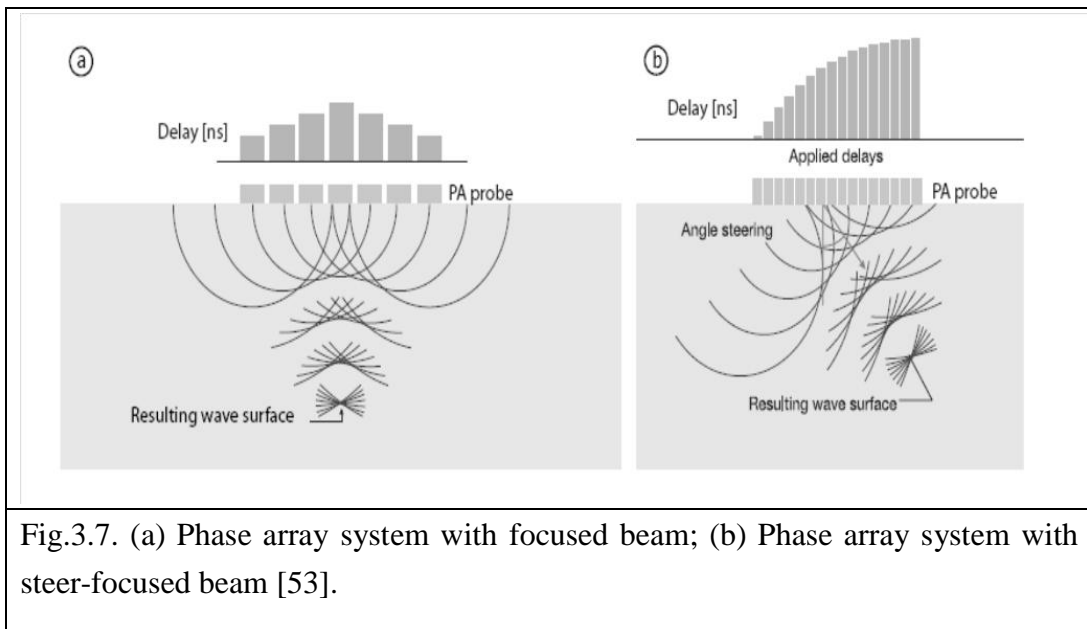


Fig.3.7. (a) Phase array system with focused beam; (b) Phase array system with steer-focused beam [53].

length and focal spot size [53]. The front aperture of the phased array transducer can be linear or curved, and the arrays can be linear or annular for different imaging applications.

In 2007, a research group used a 30 MHz linear array transducer with 64 elements to apply for B-scan and Doppler imaging. The lateral resolutions at different depths provided by the linear array transducer were from 160 μm to 310 μm .

Their imaging system could measure motion velocity in the range of 0.1 mm/s to 1 m/s [54].

3.3.3 C-scan system

C-scan imaging techniques construct images in a plane which is normal to the one in the B-scan image. For C-scans, the ultrasound beam is scanned over the entire area at certain depth of the tissue in a 2-D mode, and each A-scan line of data is sampled and recorded at each scan position to form the C-scan image. A focused transducer is often used in a C-scan system to improve the image lateral resolution [5]. The disadvantage of C-scan system is that it takes a relatively long time.

3-D imaging is more beneficial than 2-D imaging for its better visualization and reconstruction. There are many ways to construct 3-D images. Traditionally, an ultrasound transducer is mechanically scanned over a target tissue. One is to linearly scan over the tissue of interest and a 2-D image is acquired. A fast 3-D image is reconstructed by using the predefined geometry of the 2-D image planes. This method is called linear 3D scanning. Another method is called tilt 3D scanning, which is scanning a conventional transducer as before, but acquiring the 2D image at regular angular intervals. This results in a fan shape 2D image that increases the view of the tissue area of interest. The third way of scanning is rotational 3D scanning, which is scanning an array transducer in a contour to reconstruct the acquired 2D image [55].

Another method of constructing 3D image is free-hand scanning with position sensing. This method is called “articulated arm 3D scanning”. The ultrasound transducer is mounted on a mechanical arm system with multiple joints. The 3D image is reconstructed from the acquired 2D image by calculating each position and orientation of the transducer. Another approach is using three sound emitters mounted on a transducer and an array of fixed microphones over the patient to receive signals. By calculating each acquired 2D image due to the position and orientation of the transducer, a 3D image is reconstructed. This method is called “acoustic free-hand 3D scanning” [55].

All the above scanning mechanisms use conventional one dimensional transducer and rely on mechanical scanning. However, 2D array transducers have been fabricated and applied in 3D imaging removing the need for mechanical scanning using electronic scanning of the array elements [55]. Khuri Yakub’s group has developed 2D cMUT arrays with integrated circuits to make 3D images and they have also fabricated large 2D arrays with piezoelectric crystals. Their 2D cMUT

arrays have 16 by 16 elements with operating frequencies from 3 MHz to 7.5 MHz. This 2D array is flip-chip bonded to an integrated circuit for comprising front-end electronics with a 27 volt pulser and 10 MHz bandwidth amplifier for each array element. An FPGA board is used to control the system and acquired data. Their 2D arrays have been used for 3D photoacoustic imaging [56].

Visual Sonics has used their Vevo technology for 3D imaging of tumors. It

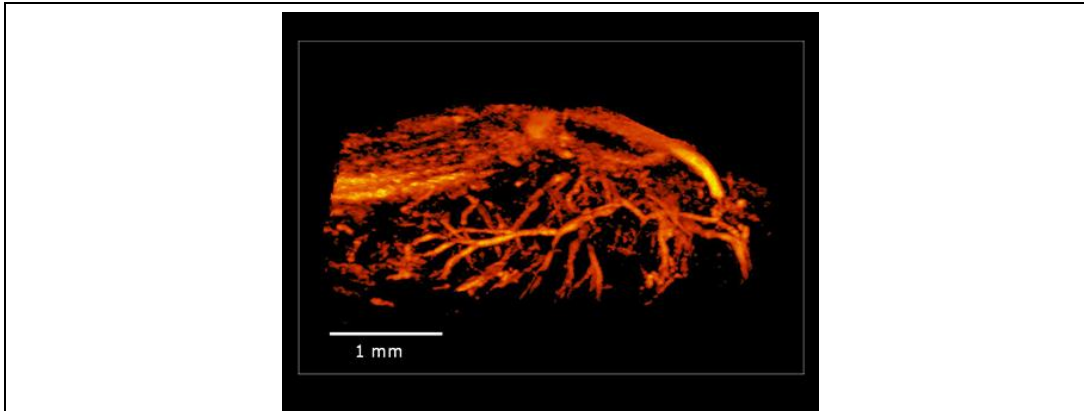


Fig.3.8. 3D power Doppler image of fibrosarcoma tumor in a mouse [44].

provides better tumor visualization than 2D images. Figure 3.8 shows a 3D power Doppler image of fibrosarcoma tumor in a mouse [44].

3.4 Fabrication of different linear array high-frequency transducers and their characteristics

A number of groups have made significant progress in fabricating high-frequency ultrasound transducers. Fabrication of these transducers is challenging and an active research area because of the small element sizes and kerfs needed, because precise control of piezoelectric material thicknesses and matching layers is required, and because interconnects, impedance matching, parasitic capacitance are non-trivial and because high-frequency electronics often require customization. A non-exhaustive list of some of the progress in the area includes the following:

In 2007, a research group made a linear array ultrasound transducer with an operating frequency greater than 30 MHz [57]. They used a sol-gel composite material rather than raw PZT material and three types of substrate materials. After testing the sol-gel PZT composite film material, it provided 2230 m/s longitudinal wave velocity and 4370 kg/m³ density, which was about 40% less than the raw PZT material [57]. This is more beneficial for fabricating high-frequency ultrasound arrays. This group tried to use three different materials as the substrates and make a comparison of their performances. The idea was to use a thin substrate; in their process, they used a 38 μm thick SS foil, 22μm thick Al foil

and 50 μm PI film as the substrate respectively. A bottom electrode was needed if the substrate was an insulator. Finally, they included a total thickness less than 100 μm of a top electrode and a sol-gel piezoelectric composite ceramic layer. The three types of arrays with different substrate materials were tested by pulse-echo measurement using an 8 mm thick aluminium alloy plate as the target. The center frequencies of SS, Al and PI ultrasound transducers were 18 MHz, 30 MHz, and 36 MHz respectively. The 6-dB bandwidths of SS, Al and PI ultrasound transducers were 12 MHz (67%), 14 MHz (47%), and 28 MHz (78%) respectively. The center frequency of the PI ultrasound transducer was close to 37.2 MHz half wavelength resonant frequency, and the center frequency of the SS ultrasound transducer was close to 18.6 MHz quarter wavelength resonant frequency. A 1 mm thick silicone rubber was used as the sample to study tissue characterization using these ultrasound transducers constructed with three different substrate materials. As a result, the high-frequency component of the PI ultrasound transducer was strongly attenuated because of the high ultrasonic attenuation in the silicon rubber and its large thickness. The result showed that PI ultrasound transducer was more suitable for tissue and tissue-like ultrasonic measurements due to its excellent acoustic coupling characteristics [57]. As well, the PI substrate provided a great acoustic impedance matching layer between the tissue and the sol-gel PZT composite when using the proper substrate thickness.

Using laser micromachining technique, a research group successfully fabricated a linear array with 64 elements, which had a 30 MHz center frequency, 74 μm pitch and 8 μm kerf. The electrical impedance of these arrays measured in air was about 120 ohms and -20 degree in phase [58]. At an axial distance of 10 mm from a transducer element, the average peak to peak pressure was measured to be 590 +/- 24 kPa. The unique part of their technique was using a laser to cut the PZT bar for fabricating these elements and defining the width of the kerfs. The laser they used was a UV laser that had an 8 μm spot width and an approximate 6 J/cm² fluence. However, it was difficult to produce an image as the array required the physical connecting and disconnecting of coaxial cables to each array element without disturbing the accurate position between the array and the sample object.

In 2005, a research group from the University of Southern California fabricated a kerfless linear array ultrasound transducer with a 30 MHz center frequency. They made a comparison between this kerfless array and a 30 MHz piezo-composite array. Based on the technique of fabricating a piezo-composite array, they added an extra 8.3 mRayl acoustic matching layer under the epoxy lens layer to achieve a broad bandwidth response [59]. This kerfless array with two matching layers had some advantages over the piezo-composite array with one matching layer, such as 7dB greater two-way single element sensitivity and higher average echo center frequency. However, the kerfless array had serious reduction in the

acceptance angle caused by the increase of electromechanical crosstalk. The -6 dB acceptance angle of the kerfless array was 22 degrees compared to the composite array of 35 degrees. This acceptance angle reduction also limited the beam steering properties of the kerfless array. The maximum crosstalk of the kerfless array was 14 dB greater than the composite array. Due to the increased crosstalk, the directivity of the kerfless array was also affected [59].

The choice of material used to fabricate high-frequency array ultrasound transducers is very critical for the overall transducer performance. A research group concentrated on producing high quality materials to construct high-frequency ultrasound transducers. They used high rate Physical Vapor Deposition (sputtering) to make high quality piezoelectric films with a metallic target in the sputtering process. They also developed photolithography and masking techniques to fabricate interlayer electrodes for small scales [60]. The sputtered PZT piezoelectric film had lower acoustic impedance values which made it easier for impedance matching in the media and also faster to fabricate. The mechanical loss tangent of the sputtered PZT film was higher. This might cause higher self-heating during the fabrication process. Using the same technique, they fabricated a 42-element linear array ultrasound transducer with a center frequency of 150 MHz by using ZnO as the substrate.

3.5 High frequency ultrasound imaging

3.5.1 High frequency ultrasound imaging methods & applications

High frequency ultrasound imaging techniques are widely used in small animal and *in vivo* biomedical studies by using high frequency ultrasound transducers in the imaging system. These systems provide real-time images with high resolution. However, the technique has limitations due to the transducer element size and signal processing issues. One research group developed improved high frequency ultrasound imaging techniques to study morphological observation and blood flow mapping in small animals. They noticed that the traditional high frequency ultrasound method, which needed to mechanically scan a single element transducer, as well as the limited dynamic range, and prevented the detection or measurement of blood flow in very small vessels. They mounted a single element transducer with a 25 MHz center frequency on a three-dimension scanning stage controlled by ultrasonic motors. They used piezo-ultrasonic motors to reduce the radio frequency interference. These motors could achieve wide dynamic scan speed range from several microns per second to 250 mm/s, providing the highest frame rate of 23 frames/s in 2 mm scanning width. This stage provided two scanning modes: B-mode and swept-scanning mode. Their system provided

high-frequency ultrasound real-time images with 150 μm resolution and a maximum dynamic imaging range over 60 dB. By applying their system, they completed tumor studies, such as tumor growth and tumor blood flow velocity in mice [61].

A research group has used a three-dimensional high-frequency ultrasound imaging system to noninvasively detect and longitudinally measure the murine liver metastases. Their three-dimensional high-frequency ultrasound system could identify areas of liquefactive necrosis inside of the metastases, monitor the therapeutic response of individual metastases, and could monitor the tumor growth during the early metastatic process. An ultrasound transducer with a 40 MHz center frequency was used, and their system provided high-resolution images with fast imaging speed [62].

A research group has applied high frequency ultrasound imaging to diagnose pupillary block glaucoma, since it could provide better resolution, which was very important in this case. They used two high frequency ultrasound transducers made from polymer and ceramic with a 50 MHz center frequency and a maximum bandwidth of 70 MHz. These two transducers were mounted on a motor-controlled stage, which was operated by computer to scan over the eye with tuneable scan width. By using high frequency ultrasound, they have concluded three important findings, and they proposed that high frequency ultrasound technique was reliable to non-invasively diagnose eye problems [63].

Another research group has used the high frequency micro-ultrasound system developed by Visual Sonics for *in vivo* cerebral hemodynamics imaging. They used two ultrasound transducers with centre frequencies at 20 and 40 MHz respectively. They have demonstrated power and color Doppler imaging, pulsed-wave Doppler imaging, and contrast-enhanced imaging on rat brains for hemodynamic measurement. Their high frequency micro-ultrasound system provided 30 to 200 μm resolution and 1000 frames per second temporal resolution [64].

Visual Sonics has developed their Vevo technology for high frequency ultrasound imaging application. The Vevo 770 high-resolution *in vivo* micro-imaging system was first developed for entry-level platform study of small animals. This system provided 30 μm resolution and 240 fps frame rates to help visualize and quantify anatomic tissues, hemodynamics and therapeutic treatment of small animals. Lately, the Vevo 2100 high-frequency, high-resolution system was developed, providing a variety of applications for small animal studies. It uses a digital

imaging platform formed by linear array and Color Doppler technologies. It is the update version of the Vevo 770 system based on the application of solid-state array transducers. These MicroScan transducers operate at different frequencies for different small animal and organ structure studies, resulting in improved frame rates, higher contrast and resolution, and larger range field of view. The Vevo 2100 system has 30 μm resolution, 2D 740 fps frame rate, and increased field of view. Both the Vevo 770 and the 2100 systems provide Power Doppler imaging, M-Mode and 3D imaging, and contrast imaging. Moreover, the Vevo 2100 system provide Color Doppler imaging, superb B-Mode imaging, VevoStrain analysis, and advanced measurement applications [44].

For cardiovascular studies, Vevo provides 30 μm resolution for biomarker and translational research in small animals. Its high frame, acquisition rate allows higher temporal and spatial resolutions compared with MRI or CT [44]. The Vevo technology is also used for real-time imaging of tumors. It can detect early stage tumors, quantify tumor size in 2D and 3D, and visualize subcutaneous or

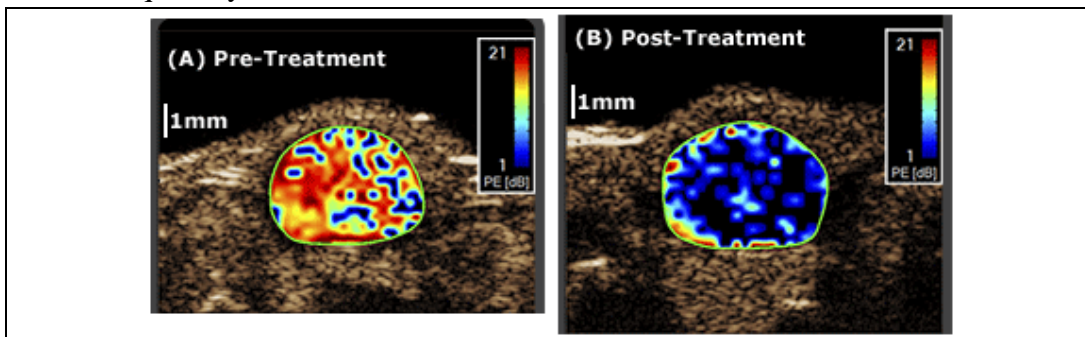


Fig.3.9. Peak enhancement parametric map of tumor contrast for a mouse model A) before and B) after treatment [44].

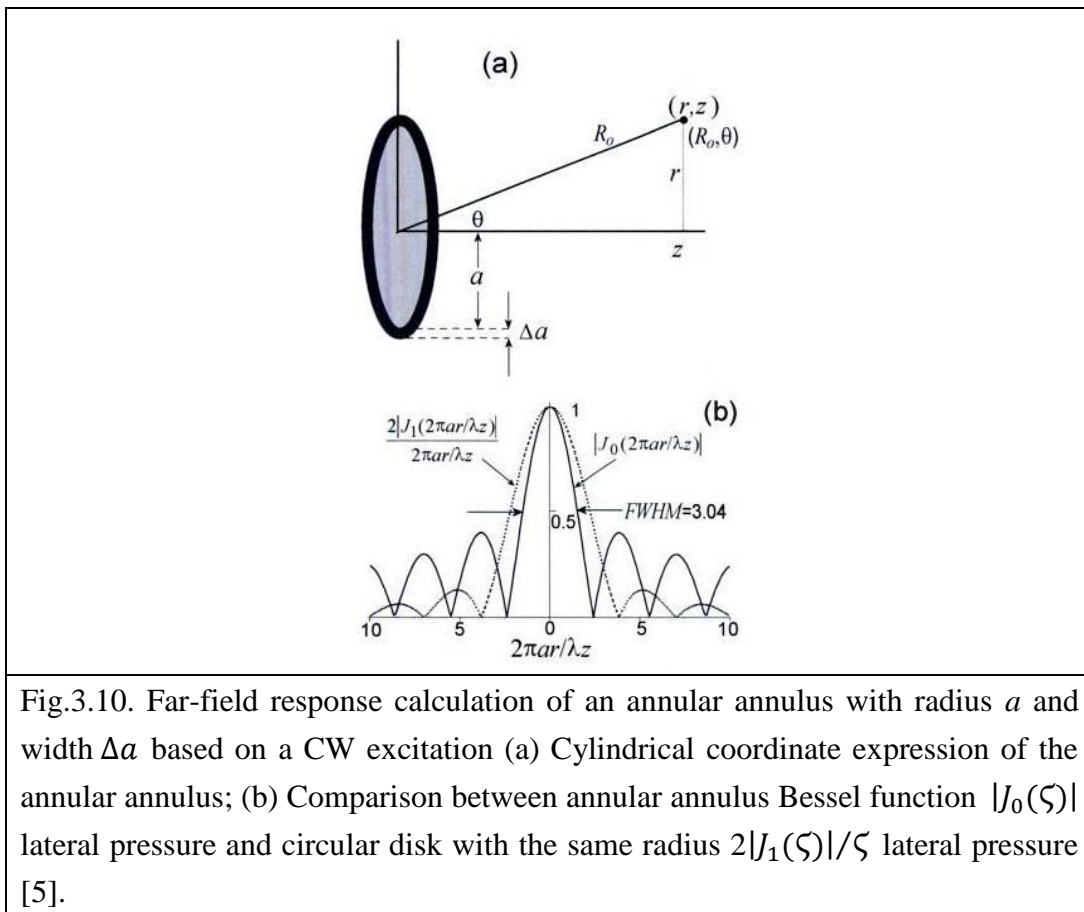
orthotropic soft tissue tumors. Figure 3.9 shows a peak enhancement parametric map of a tumor contrast for a mouse model A) before treatment and B) after treatment [44].

The Vevo high-resolution imaging system is also used to visualize early brain structures and spinal cord development, and help guide pulled glass needles used to deliver cells, drugs, and other genetic materials into embryos of small animals. Combining with the SoniGene system, the Vevo high-resolution system has contributed to non-invasive, longitudinal and repeatable delivery of genes, proteins or drugs into cells. The 30 μm spatial resolution provided by the Vevo high-resolution micro-ultrasound system has provided great delineation of renal tissues for allowing researchers to quantify and analyze renal functions of small animals for nephrology studies. With such high spatial resolution, the Vevo

system was also used for other organ studies, such as livers, pancreas, reproductive systems and eyes [44]. Some researchers have also used the Vevo system on rheumatology and musculoskeletal studies by visualizing joint tissues, muscles and connective soft tissues of small animals. Others used the same system to study tissue regeneration, including nerve damage and recovery, and stem cell studies [44].

3.6 Introduction of annular array transducers

The motivation of using an annular array transducer is to achieve dynamic



focusing rather than a single focal length offered by a single element transducer. Compared with linear arrays, annular arrays have the ability to achieve dynamic elevational focusing, which can improve the imaging depth of field. For higher operating frequencies, it is difficult to construct linear array transducers, as fine element spacing is required in order to avoid grating lobes. Annular array transducers also have the advantage of electronically pulsing or scanning the individual elements. In ultrasound imaging, the whole annular array aperture is emitted to the target, and each annulus receives the reflected signal; by applying

dynamic receive beam-forming to the received signals, signals at different depths are maximized and the imaging depth of field is achieved. Figure 3.10 shows an annular annulus whose radius is a and width is Δa , which is small compared with the wavelength [5].

In this case, the velocity impulse response for annular annulus at (r, z) is expressed as [5]

$$h(r, z) = \frac{c_0 \Delta a}{\pi r} \left\{ 1 - \frac{[a^2 + r^2 + z^2 - c_0^2 t^2]^2}{4a^2 r^2} \right\}^{-1/2} \quad (3.30)$$

when $[(a - r)^2 + z^2]^{1/2} < c_0 t < [(a + r)^2 + z^2]^{1/2}$ $h(r, z) = 0$ elsewhere

The pressure phasor is expressed as [5]

$$\underline{p}(r, z; \omega) \approx \frac{j\omega\rho_0 v_0 a^2}{R_0} e^{-jk[z+r^2/(2z)]} J_0(kar/z) \quad (3.31)$$

And the full width half maximum (*FWHM*) in this case is given by [5]

$$FWHM = 0.48\lambda z/a \quad (3.32)$$

In figure 3.10 (b), we see that the *FWHM* of the annular annulus is 25% smaller than the circular disk, but the first side lobe of the annular annulus is 3.5 times larger than the circular disk. Such large side lobes are not tolerable in medical imaging because they can affect the image quality by masking image information [5]. When using annular arrays, the signals from multiple annuli are combined in a dynamic receive focusing algorithm and this delay-and-sum procedure effectively improves the overall image quality over single element or single-annuli transducers.

3.7 Comparison of piezoelectric materials

There are many types of piezoelectric materials, such as piezoelectric ceramics, composites, and polymers. We compared the properties of three main piezoelectric materials, including ceramics and polymers, as shown in table II [5].

Table II: [Comparison of properties for PVDF, P(VDF-TrFE), and PZT5A] [5]

Parameter	PVDF	P(VDF-TrFE)	PZT5A
Speed of sound, m/s	2200	2400	4350
Density, kg/m ³	1780	1880	7750
Z _o , MRayl	3.9	4.5	33.7
Relative permittivity	6.0	5.0	1200
Mechanical Q, Q _m	10	25	75
Coupling factor, k ₃₃ ^t	0.15-0.20	0.3	0.49
Mechanical flexibility	Outstanding	Satisfactory	Poor

3.7.1 Disadvantages of certain materials for transducer fabrication

PZT5A has the greatest impedance value among these three piezoelectric materials. It does not match the tissue impedance, so additional impedance matching layer is required. The mechanical flexibility of PZT5A is poor, so it limits its application for fabricating only planar transducers rather than transducers with curved apertures. The mechanical flexibility of P(VDF-TrFE) is satisfactory, but its application is still limited for its relatively larger impedance value compared with PVDF. PVDF and other piezopolymers are in general good receivers but poor transmitters.

3.7.2 Advantage properties for transducer fabrication

PVDF has the lowest impedance value, which is the closest one to the tissue impedance, so it has the best impedance matching and may not require an additional impedance matching layer. PVDF also has outstanding mechanical flexibility, which enables it to form into different aperture shapes. This property expands its application for different transducer fabrication methods with various aperture shapes. With high mechanical flexibility property, PVDF can also be stretched to achieve certain thickness for fabricating high frequency transducers. P(VDF-TrFE) has a slightly higher impedance value, which may be considered as the second choice material for transducer construction. The coupling factor measures the efficiency of the piezoelectric material that transforms mechanical energy to electrical energy and/or vice versa. In this case, PZT5A has the highest coupling factor, which shows it has the best energy transformation efficiency. However, in our case, we are only using the fabricated transducer as a receiver. For the above reasons, PVDF is the best choice in our case to use for fabricating high frequency concave annular array transducer.

3.8 Different fabrication methods of annular array transducers

The first annular array transducer was designed and fabricated by Dennis R. Dietz and patented on August 27 1985. This annular array transducer was made of piezoelectric material with a concave aperture including four annular array elements. In the near field regions, it had an f-number range from three to five. The widths of these annuli were calculated for phase error tolerance when they were energized in the corresponding depth of field. Along the z-axis, the minimum and maximum depth of field achieved were 40 mm and 170 mm. Figure 3.11 shows a configuration of the annular array transducer and its front aperture with four annuluses. The labels numbered from 11 to 14 represented the transmit and receive channel connections for the four annuluses. This annular array transducer was fabricated for the purpose of realizing dynamic depths of focusing and applied in an ultrasound diagnosis system [65].

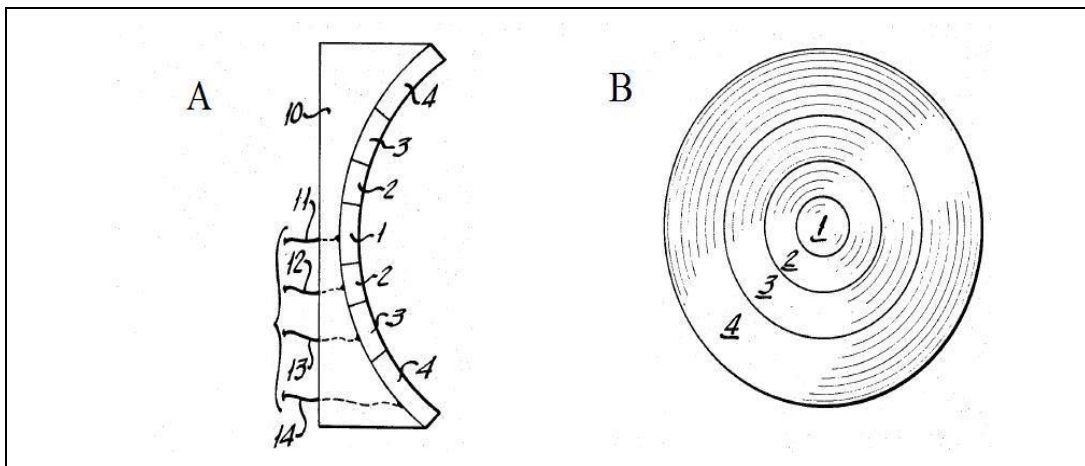


Fig.3.11. (a) Configuration of the annular array transducer (b) Front aperture [65].

More recently, a high-frequency annular array ultrasound transducer was fabricated using a 9 μm P(VDF-TrFE) film bonded to gold annuli electrodes on a two-sided polyimide flexible circuit top layer [66]. This annular array ultrasound transducer had a center frequency of 55MHz and 47% bandwidth for each element. The P(VDF-TrFE) copolymer was chosen to be the material for annular array fabrication because it had a low acoustic impedance about 4.3 mRayls and a low lateral piezoelectric strain constant of about 12 pC/N, requiring no additional matching layers and ensuring overall performance of the annular array. By using two-sided flexible circuit interconnection, it had the advantage of using micro vias to connect the top and bottom electrodes to each element [60]. After testing, the lateral resolution of the annular array ultrasound transducer in the depth of field was greatly improved by applying dynamic focusing, and its sensitivity was also improved by using a zero phase at resonance and a 50 ohm impedance matching to each element electrically. This high-frequency annular array ultrasound

transducer fabrication technique was concluded to have the potential for future mass production based on its reliability and repeatability.

Snook et al. group from Pennsylvania State University has successfully fabricated an annular array ultrasound transducer with a 50 MHz center frequency by using fine grain lead titanate (PbTiO_3) as the piezoelectric material. Previously, the lead titanate material was fully characterized by the resonance techniques. This material was then formed to an array with a 5 mm diameter containing six equal area elements. They also used a laser micromachining technique to dice each element [67]. The laser they used was a tripled YAG laser that could cut the kerf in a very small scale and also helped achieve isolation of each array element. In comparison with PVDF annular arrays, it had better sensitivity and lower lateral coupling due to crosstalk reduction. By comparing with arrays made from PbTiO_3 , PVDF, and PZT, the PbTiO_3 arrays performed with the highest center frequency and had relatively low peak crosstalk values and high thickness coupling values. Furthermore, lead titanate (PbTiO_3) has the advantage of having high thickness coupling and low lateral coupling values and relatively low permittivity, allowing design for larger aperture arrays. After being modeled, the result showed a side lobe level reduction with an apodized excitation pattern.

Brown et al. group has fabricated a 50 MHz planar annular array transducer with 2 mm aperture diameter and 7 equal area elements. The elements were formed using photolithography onto the PZT substrate coated with a 2 μm aluminum layer. 25 μm aluminum wires were bonded to each annular element for electrical contact. This annular array transducer had a -6 dB bandwidth of more than 50%, 75 μm two-way beam width, and a -16 dB insertion loss [68]. Another research group applied the similar fabrication technique to make a 45 MHz annular array transducer with 6 equal area elements. The piezoelectric material they used was lead titanate for its lower planar coupling compared with PZT ceramics [69]. These two groups have successfully fabricated high frequency annular array transducers using photolithography techniques, which was the inspiration for our project.

Ketterling and Lizzi [70] applied a photolithography method to pattern 5 annular arrays onto a copper-clad polyimide film, which was then bonded to a 9 μm single sided PVDF film with a drop of non-conductive epoxy. The front aperture was formed into a concave shape by using a designed press-fit assembly. This concave annular array transducer with 5 equal area elements had a 40 MHz center frequency, 6 mm aperture diameter, and 12 mm focal length. They also designed a PCB to provide an electrical connection to each annular array element [70]. For our project, we followed a similar fabrication procedure to make our high frequency 8-element concave annular array transducer.

Ch4: Annular Array Simulations

In this chapter we perform acoustic field simulations of annular arrays to model the expected performance to understand trade-offs in our proposed designs to optimize image quality in our proposed annular array photoacoustic imaging system. We begin by reviewing the basic theory behind the simulations we will use, starting with ultrasound then photoacoustic point-spread function simulation methodology.

4.1 Ultrasound pulse-echo impulse response

Here we discuss linear system models of ultrasound systems as presented by Tupholme and Stepanishen [71]. We consider an illustration to analyze the pulse-echo impulse response of a transmitter-receiver pair interrogating a point-scatterer as shown in figure 4.1.

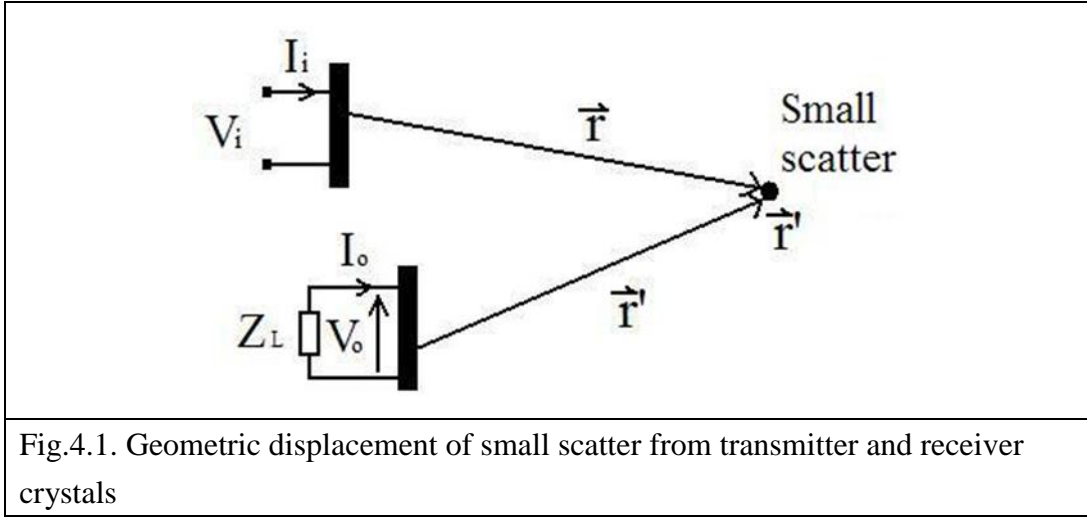


Fig.4.1. Geometric displacement of small scatterer from transmitter and receiver crystals

The velocity potential at location \vec{r} due to the transmitting transducer producing a delta-function velocity is given as [5]

$$h_t(\vec{r}, t) = \int_S \frac{\delta(t - \vec{r}/c)}{2\pi\vec{r}} dS \quad (4.1)$$

and is called the spatiotemporal impulse response. The integration area S is over the face of the transmitter. The corresponding pressure at field point \vec{r} is $\rho \frac{d}{dt}(h_t(\vec{r}, t))$. If instead we use a velocity waveform $v_i(t)$, the pressure field at \vec{r} is given by [72]

$$P_i(\vec{r}, t) = \rho v_i(t) * h'_t(\vec{r}, t) \quad (4.2)$$

The transmitter electromechanical impulse response for an input voltage of a delta-function was denoted by $T_i(t)$, then the velocity waveform was expressed as equation (4.3), and the pressure field was redefined as equation (4.4)

$$v_i(t) = V_i(t) * T_i(t) \quad (4.3)$$

$$P_i(\vec{r}, t) = \rho V_i(t) * T_i(t) * h'_t(\vec{r}, t) \quad (4.4)$$

The force $F_o(t)$ on the receiver crystal and the open circuit output voltage were related by the expression [72]

$$V_o(t) = F_o(t) * T_o(t) \quad (4.5)$$

Here, $T_o(t)$ is the electromechanical impulse response of the receiver or the output voltage caused by a delta-function of force on the surface.

As shown in figure 27, as a point source, the scatter is positioned away from the receiver crystal at \vec{r}' . When the scatter emitted a delta-function pressure, the total force on the surface of the receiver crystal was expressed as [72]

$$h_r(\vec{r}', t) = \int_S \frac{\delta(t - r'/c)}{2\pi r'} dS \quad (4.6)$$

Here, S is the surface area of the receiver crystal. In this case, the total force caused by a pressure waveform $P_o(t)$ emitted by the scatter was given by [72]

$$F_o(t) = P_o(t) * h_r(\vec{r}', t) \quad (4.7)$$

In an isotropic scattering case, the pressure waveform was defined as [72]

$$P_o(t) = S(t) * P_i(t) \quad (4.8)$$

Here, $S(t)$ represented the scattering impulse function, often modeled as a delta function $\delta(t)$. By combining equations (4.5), (4.7), and (4.8), the output voltage from the receiver crystal could be expressed as [72]

$$V_o(t) = S(t) * P_i(t) * h_r(\vec{r}', t) * T_o(t) \quad (4.9)$$

By substituting equation (4.4) into equation (4.9), the output voltage was redefined as [72]

$$V_o(t) = S(t) * \rho V_i(t) * T_i(t) * h'_t(\vec{r}, t) * h_r(\vec{r}', t) * T_o(t) \quad (4.10)$$

Equation (4.10) represented the ultrasound pulse-echo voltage. For the typical case where transmitter and receiver were the same and built-in as one ultrasound transducer, then the following condition holds [72].

$$h_t(\vec{r}, t) = h_r(\vec{r}', t) \quad (4.11)$$

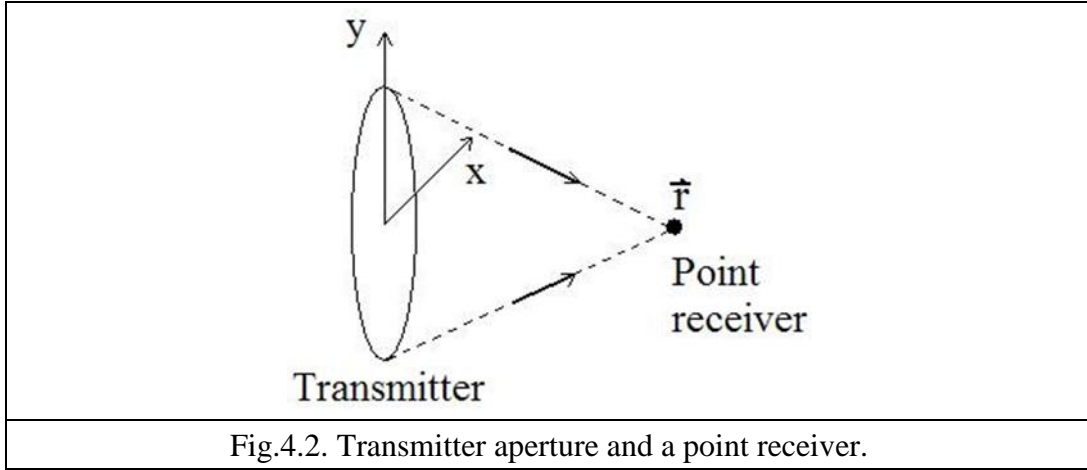
4.2 Simulation software

Acoustic field simulations are used to understand the effect of transducer design parameters on expected imaging performance. All the simulations in this project were designed using the simulation program Field II [73,74]. This software used a Matlab environment to simulate both pulsed and continuous wave ultrasound transducer fields and ultrasound imaging based on the concept of spatial impulse responses. It was developed by J.A. Jensen and used the Tupholme-Stepanishen method to calculate spatial impulse responses assuming linearity. When an ultrasound transducer was excited by a Dirac delta function, the emitted ultrasound field would have an impulse response at a specific position in space as a function of time. This excitation field could be found by convolving the excitation function with the spatial impulse response. Since it was different to calculate the spatial impulse responses of different transducer geometries, this software divided the transducer aperture surfaces into many small square elements, and the final impulse response was the sum of these small square impulse responses. Field II could simultaneously calculate a series of point spread functions to examine dynamic focusing properties of the imaging system [75].

Note that for the task of simulating point-spread functions from annular rings and even annuli on a concave surface, there are analytical expressions for spatio-temporal impulse-responses as outlined by Cobbold [5]. However, these analytical expressions rely on the Fresnel and Fraunhofer approximations which are not always suitable for the high-NA transducers we aim to develop. For this reason, we chose to use Field II simulations which were less limiting. FIELD II has previously been used to simulate annular array performance for low-frequency arrays for ultrasound pulse-echo imaging but never for high-frequency photoacoustic imaging to our knowledge.

4.3 Modeling photoacoustic point-spread functions and reciprocity

Field II is designed to simulate ultrasound but not photoacoustic imaging system performance. Here we discuss our method for adapting the simulation power of FIELD II to be used for photoacoustic imaging, based on the principle of reciprocity. We have been modeling the pressure due to a transmitting aperture as shown in figure 4.2 and given by the following expressions [5].



$$P(\vec{r}, t) = \rho_o h(\vec{r}, t) * \frac{\partial v_{no}(t)}{\partial t} = \rho_o v_{no}(t) * \frac{\partial h(\vec{r}, t)}{\partial t} \quad (4.12)$$

Here,

$$h(\vec{r}, t) = \iint_{S_o} \frac{\xi_o(x, y) \delta(t - R/c_o)}{2\pi R} dS_o$$

where $\xi_o(x, y)$ is a spatial apodization weighting across the transducer surface. Usually, for a uniformly excited piston transducer $\xi_o(x, y)$ is assumed to be 1.

In photoacoustic imaging, optically absorbing targets through a volume emit photoacoustic signals due to a laser pulse effectively all at the same instant of time. This assumption is reasonable considering the speed of light is five orders of magnitude faster than the speed of sound. So in this case we consider a point absorber emitting an ultrasound impulse due to a laser pulse occurring at time $t=0$, with the transducer acting as a receiver, as shown in figure 4.3. The initial pressure from the point source can be written as [5]

$$P = P_o \delta(\vec{r}, t), \text{ let } P_o = 1 \text{ for now} \quad (4.13)$$

The received voltage as a function of time is related to the force on the transducer. The force equalled to the multiplication of pressure and transducer aperture area, which, for a delta-function source is given by [5]

$$F(t|\vec{r}) = \iint_{S_o} \frac{\xi(x, y)\delta(t - R/c_o)}{2\pi R} dS_o = h_r(\vec{r}, t) \quad (4.14)$$

Here, $h_r(\vec{r}, t)$ was the impulse-response of the receiver. It is also the same expression as the spatiotemporal impulse-response of the same transducer used as a transmitter. This means that we can use FIELD II to calculate the photoacoustic point-spread functions by using the spatiotemporal impulse-response of a transmitting transducer.

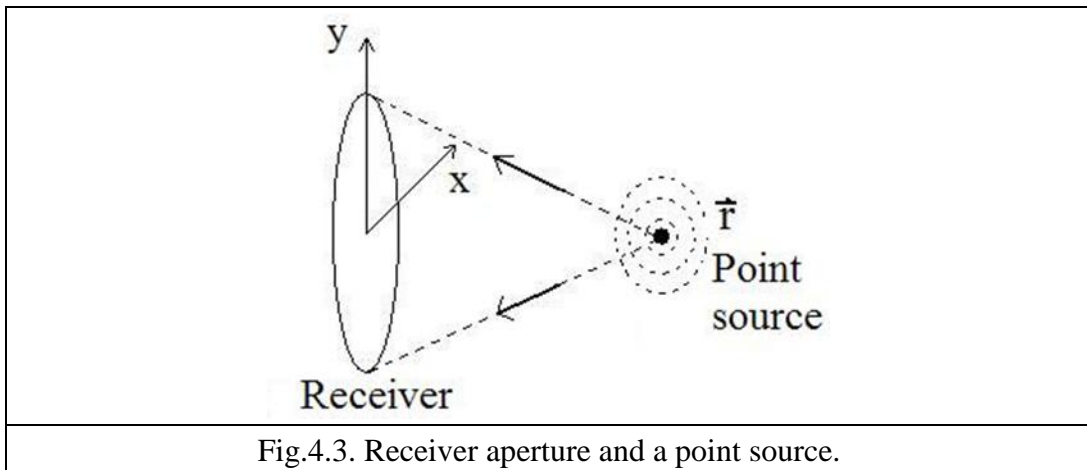


Fig.4.3. Receiver aperture and a point source.

For a point source emitting pressure waveform $P_o(t)$, the received pressure integrated over the aperture is given as [5]

$$F(t|\vec{r}) = P_o(t) * h(\vec{r}, t) \quad (4.15)$$

Therefore, the received voltage is [5]

$$V(t) = F(t) * T(t) \quad (4.16)$$

Here again, $T(t)$ is the electro-mechanical impulse-response of the transducer.

4.4 The imaging process and point-spread functions

Ultrasound images are formed by pulsing and receiving ultrasound and scanning the transducer relative to the sample, firing and receiving at each scan location.

The signal to to one pulse-echo even is called an A-scan line. Multiple A-scans from each lateral scan location are assembled to form a B-scan image. Photoacoustic images were formed via a similar process except that laser pulses are fired instead of ultrasound pulses.

A point-spread function is the image of a point-target and is a way to characterize the imaging system spatial resolution. We have simulated point-spread functions of our proposed annular array transducers, however, as a first step; we simulated point-spread functions of a single-element concave transducer.

4.5 Simulation of PSFs using single element concave ultrasound transducers

We used Field II to first simulate single-element concave ultrasound transducers. The center frequency was defined as 40 MHz. The active aperture radius was 6 mm, and the focal length was 12 mm. These transducer parameters were chosen as a reference for future annular array transducer simulations. Based on our chosen piezoelectric material PVDF, we aimed to fabricate the transducer with 40

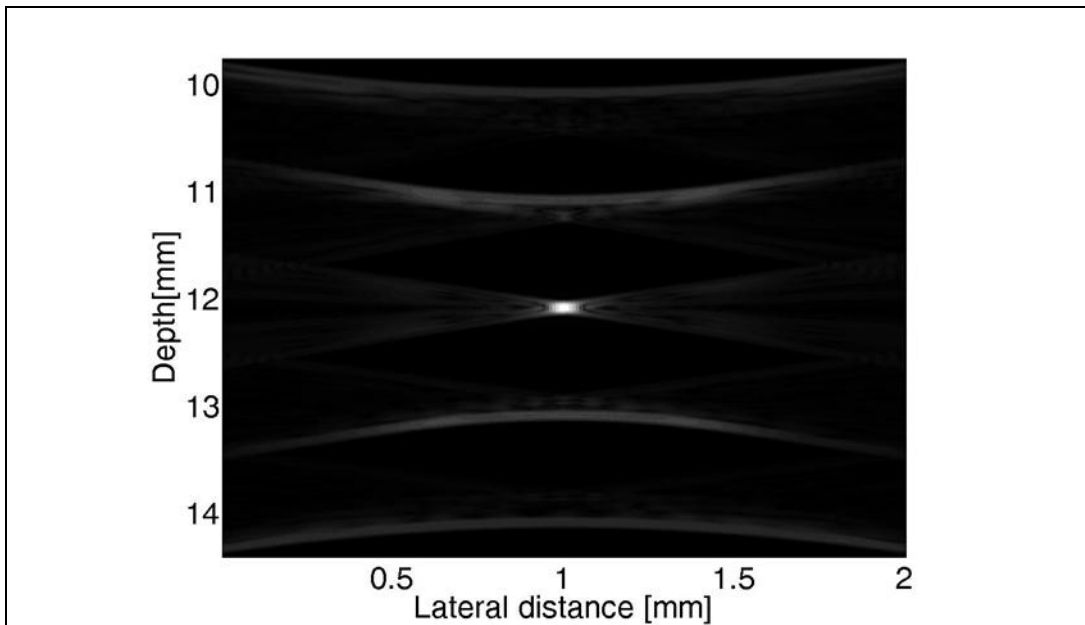


Fig.4.4. Simulation of photoacoustic image of five point-absorbers using a 40 MHz single element concave ultrasound transducer with 0.5 NA value.

MHz center frequency. The aperture size and focal length were designed to have a high numerical aperture and focusing curvature. The active aperture was divided into small squares each with 1 mm by 1 mm dimension. This concave ultrasound transducer was used to image five point-absorbers located at different depths: one at the geometric focus, two above, and two below. The first scatter point was

located at 10 mm away from the front aperture of the transducer and the space between each scatter point was 1 mm. The speed of sound in water in the simulation was defined as 1540 m/s and a 500 MHz sampling frequency was used.

The single element concave ultrasound transducer was defined by the function “ $Th = xdc\ concave(radius, focal_radius, ele_size)$ ” in the simulation. Here, “ Th ” was a pointer which indicates the specific transducer aperture; “ $radius$ ” was the radius of active aperture element, “ $focal_radius$ ” was the focal length of the transducer; “ ele_size ” was the element size of the small squares the active aperture was divided into. As mentioned, there were five point sources as the sample targets in this simulation. The two functions “ $xdc_excitation$ ” and “ $xdc_impulse$ ” were used to respectively set the excitation pulse and impulse response of the transducer aperture. The function “ $calc_scat$ ” was used to calculate the received signal from a group of points. The final received data was run through a Hilbert transform function for envelop detection and the image was based on a log-scale color map of the data [76]. Figure 4.4 showed the simulated photoacoustic point-spread functions located from 10 mm to 14 mm away from the single element concave ultrasound transducer.

From figure 30, it was noticed that the point located at the transducer focal point (12-mm depth) had the best signal strength and spatial resolution. All the other points away from the transducer focus had poor resolution. This showed that

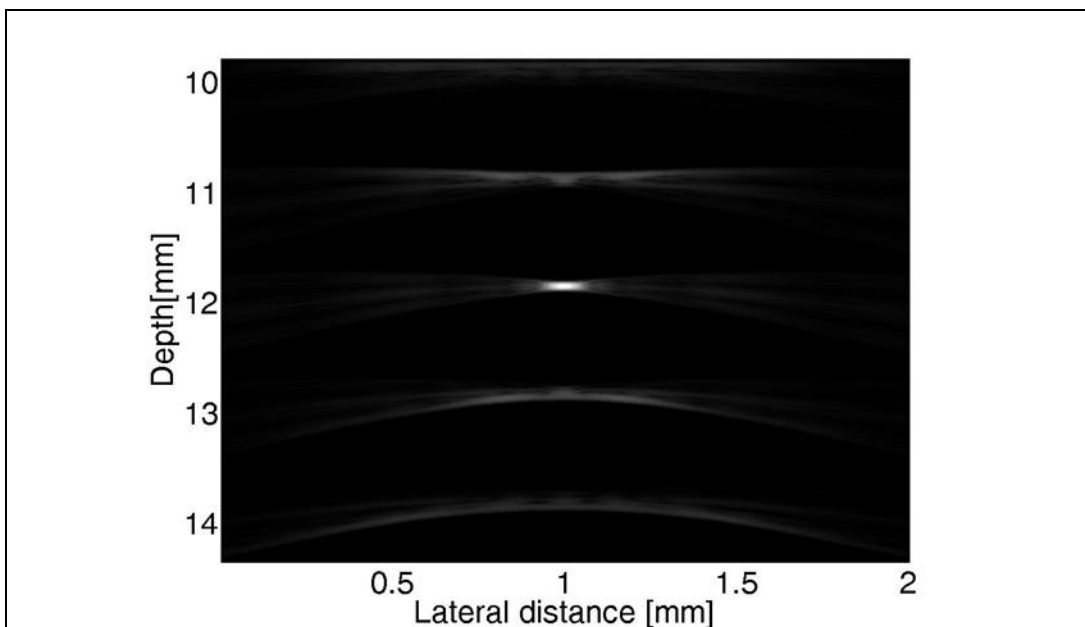
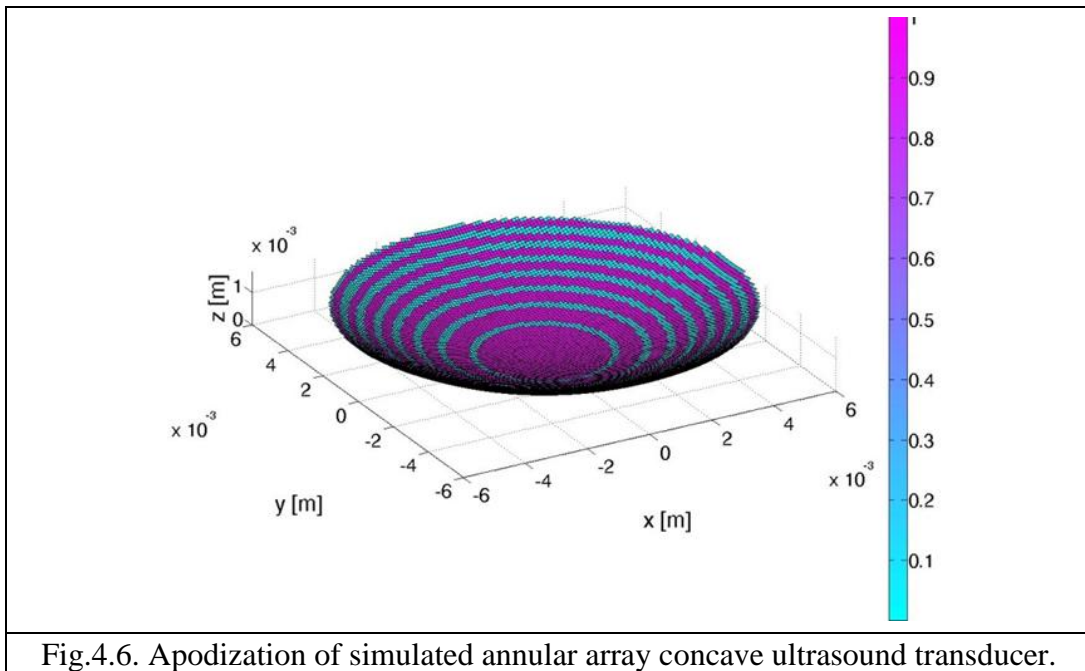


Fig.4.5. Simulation of five point-absorbers photoacoustic image by a 40 MHz single element concave ultrasound transducer with 0.33 NA value.

single element concave ultrasound transducer was limited by single focal length and thus limiting the imaging depth of field in bio-medical imaging applications.

In this case, the numerical aperture of the simulated single element concave ultrasound transducer was simulated as 0.5 based on the simulated parameters of the active aperture diameter and the focal length. Another single element concave transducer was simulated with the same center frequency and other parameters, except the active aperture radius was 4 mm instead of 6 mm. This simulated single element concave transducer was also used to receive the impulse response from the same five scatter points, as shown in figure 4.5. Compare with figure 4.4, the PSFs in figure 4.5 had larger side lobes. This was because the new simulated single element concave ultrasound transducer has a numerical aperture value of 0.33, which was smaller than the previous 0.5. It concludes that the numerical aperture of an ultrasound transducer affected the side lobe levels of the ultrasound image. The larger value of the numerical aperture was, the more side lobe levels were reduced in the ultrasound image.

4.6 Simulation of annular array concave ultrasound transducer



There were eight annuli in the active aperture with different radius and the same area, including 0.1 mm kerf space among each annular annulus. The whole active aperture was divided into small squares each with 0.1 mm by 0.1 mm dimension.

The general active aperture of the annular array concave ultrasound transducer was defined by the same concave transducer function “ $Th = xdc\ concave (radius, focal_radius, ele_size)$ ” used in the single element concave ultrasound transducer case. In addition, an apodization function was used to define such annular array aperture, which was called the “ $ele_apodization$ ”, providing a binary apodization mask for each annular annulus, where the mask was one inside the annulus and zero outside [76]. Both the excitation pulse and impulse response functions were the same as before. In figure 4.6, it showed the active aperture apodization of the simulated annular array concave ultrasound transducer.

4.7 Simulation of annular array pulse-echo ultrasound point-spread functions

This simulated annular array concave ultrasound transducer was used to ultrasonically image four point-absorbers located at 10 mm away from the front aperture of the transducer and the space between each scatter point was 1 mm as before. The speed of sound in water in the simulation was defined as 1540 m/s and a 500 MHz sampling frequency was used. In This case, a Field II function called “ $calc_hhp$ ” was used to

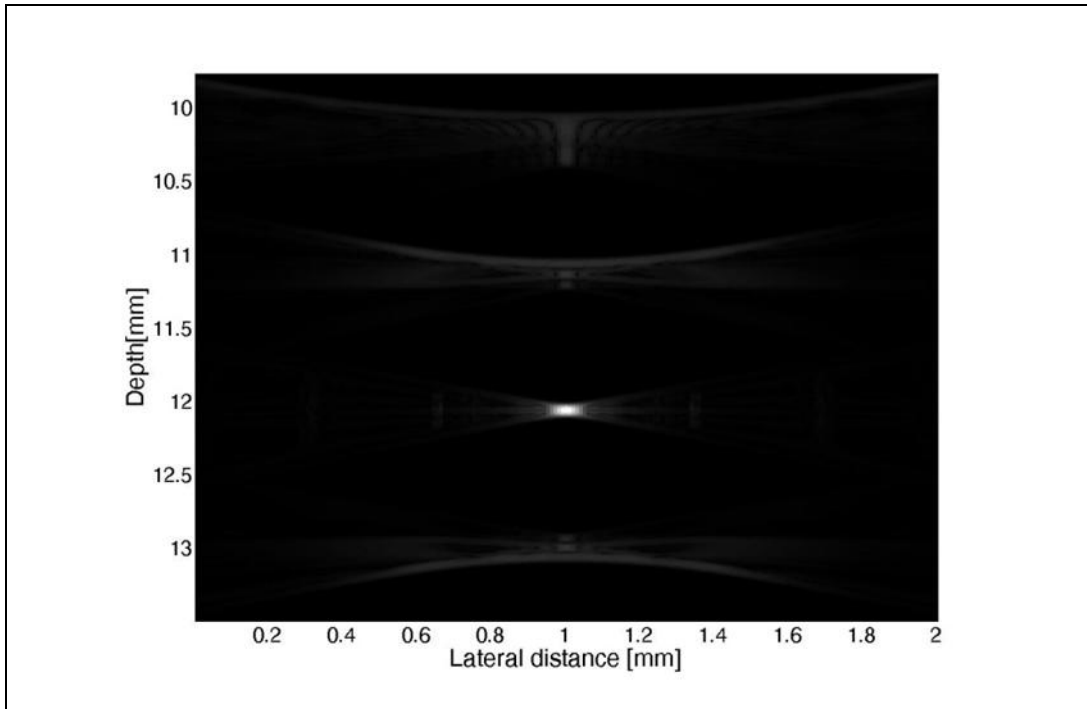


Fig.4.7. Ultrasound image of four point-absorbers acquired by simulated annular array concave ultrasound transducer before applying DR beam-forming.

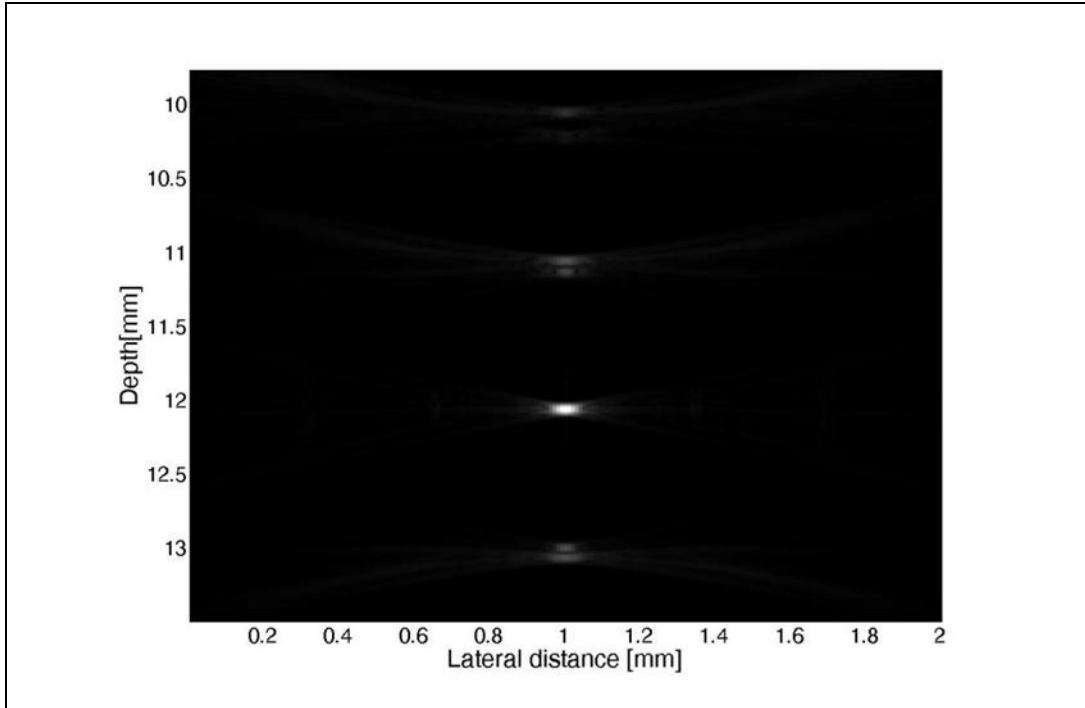


Fig.4.8. Ultrasound image of four point-absorbers acquired by simulated annular array concave ultrasound transducer after applying DR beam-forming.

calculate the pulse echo field from the four point-absorbers [76]. Figure 4.7 showed the ultrasound image of the four point-absorbers before applying the dynamic receive (DR) beam-forming algorithm (i.e. by simply summing annuli signals together). After applying the DR beam-forming algorithm, the ultrasound image of the four point-absorbers was shown in figure 34. The function of beam-forming was to achieve narrow and uniform signals with strong amplitude and low side lobe levels [77]. We developed a dynamic receive beam-forming algorithm, which was applied to the received signals by different annuli to reconstruct images of the four scatters for achieving improved depth-of-field as shown in figure 4.8.

4.8 Simulation of annular array photoacoustic point-spread functions

We also simulated the imaging performance of the annular array transducer using photoacoustic imaging. Five point-absorbers were imaged using the same annular array transducer. Absorbing point targets were located at identical positions to the scatterers used in the ultrasound simulations above. The speed of sound in water in the simulation was defined as 1540 m/s and a 500 MHz sampling frequency was used. In this case, a Field II function called “*calc_hp*” was used to calculate the emitted field from the five point-absorbers [76].

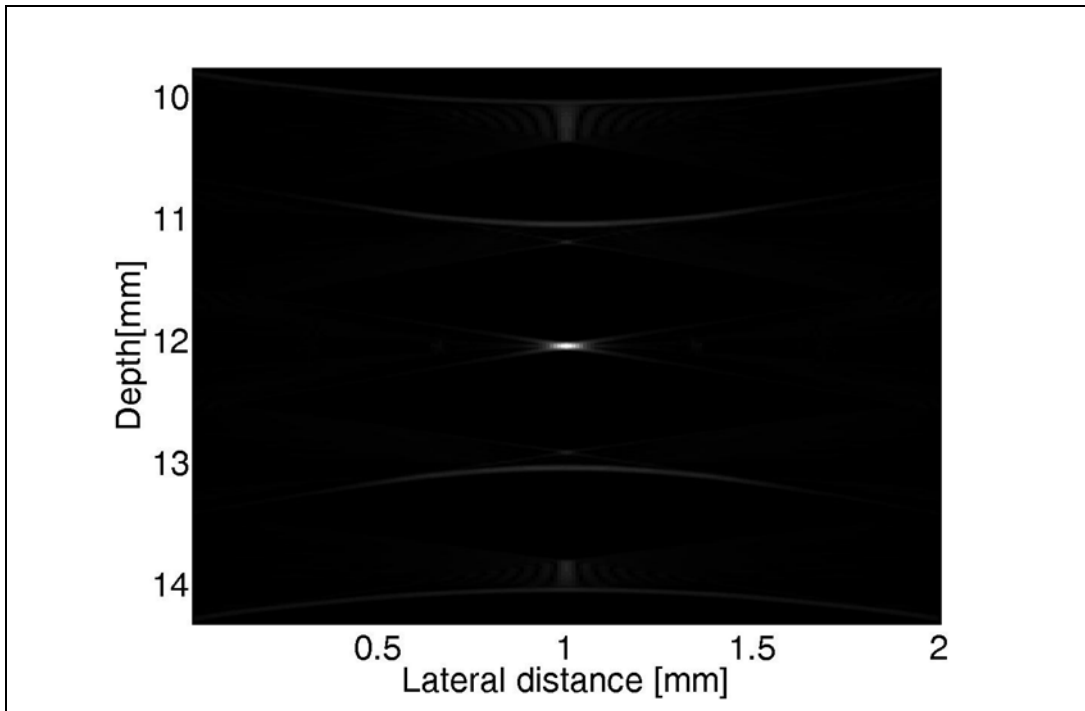
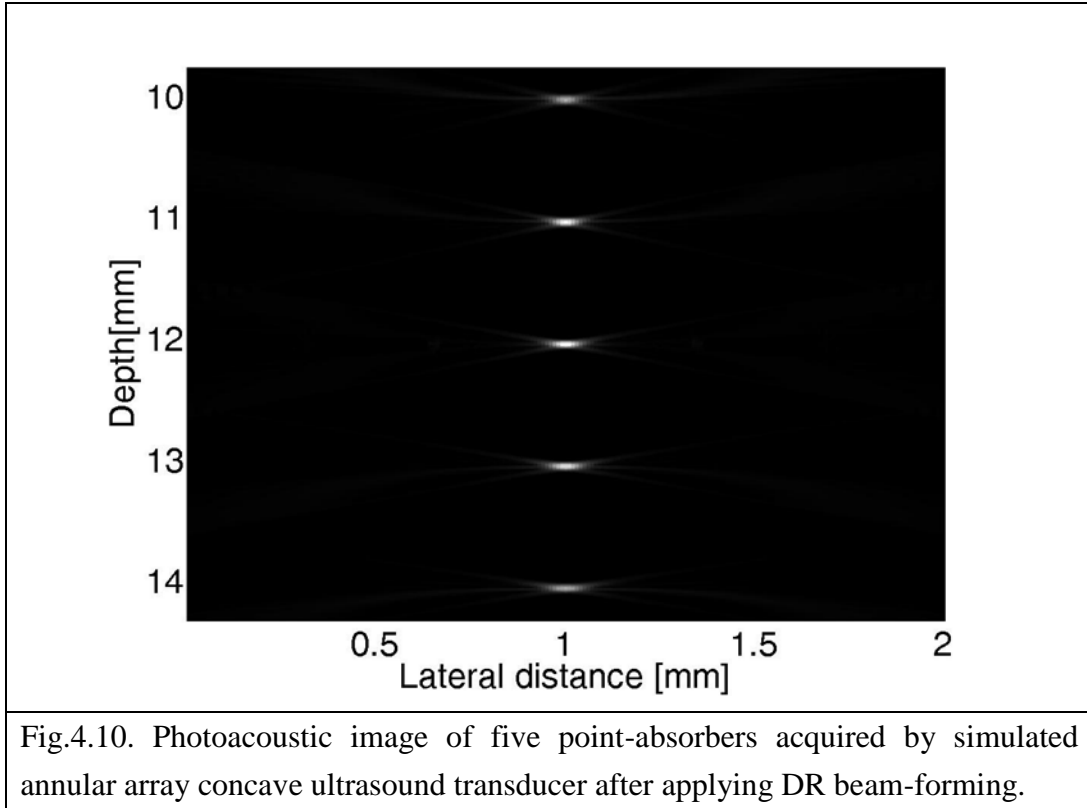


Fig.4.9. Photoacoustic image of five point-absorbers acquired by simulated annular array concave ultrasound transducer before applying DR beam-forming.

The whole active aperture of the annular array concave ultrasound transducer was first excited with ultrasound pulse, and the final image was constructed by summation of the impulse response from the five point-absorbers received by each annular array after applying dynamic-receive (DR) beam-forming algorithm. In order to emphasize the DR beam-forming algorithm functionality, photoacoustic image of the five point-absorbers before applying the dynamic beam-forming algorithm was firstly illustrated in figure 4.9. After applying the DR beam-forming algorithm, the photoacoustic image of the five point-absorbers was shown in figure 4.10.



4.9 Dynamic receive (DR) beam-forming (algorithm & equations)

From figure 4.9 and 4.10, it was obvious to see how effective the functionality of dynamic receive (DR) beam-forming algorithm was. In both ultrasound and photoacoustic images, all the point-absorbers were more focused after applying the DR beam-forming algorithm. For each received signal by different annuli, the received data was reconstructed to reach the maximum value or signal amplitude. The final image was based on summing up the reconstructed received data by different annuli. The DR beam-forming algorithm increased the signal strength or amplitude and reduced the side lobe level by having more focusing power. Keeping uniform signal amplitude and resolution, it improved the image depth-of-field.

A diagram of the dynamic focusing geometry is shown in figure 4.11. In order to figure out the dynamic receive beam-forming algorithm, the image target was assumed on the z-axis for simplicity. Point F was the true geometric focal point and f was the focal length of the true transmitting aperture; point B was the image target or signal source and Z_B was the distance between the origin and the signal source. Point S_i indicated the coordinate of annulus i for the true

transmitting surface, and S'_i was the new coordinate of annulus i for the desired transmitting surface in order to focus right on the signal source B .

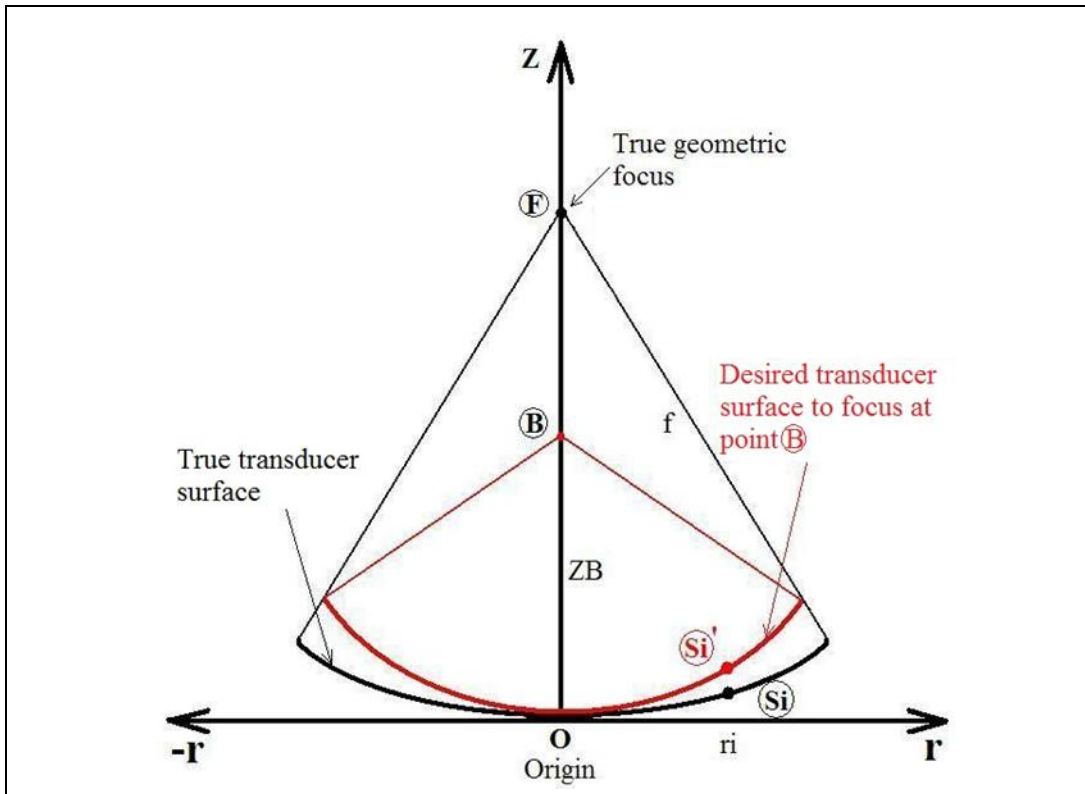


Fig.4.11. True and desired transmitting apertures of annular array concave ultrasound transducer.

From figure 4.11, it is observed that the signal source B was not located at the true geometric focus of the annular array concave ultrasound transducer, so if there were no delays applied, after the received signals from all the annuluses were summed up, the final received signal would not be the strongest or most focused. Therefore, in order to properly focus the signal source, a new virtual transducer surface is required, with a smaller radius of curvature, which was shown as the red color in figure 4.11. Figure 4.12 illustrated a more detailed graph in order to include more information for calculating the true delays. Here, the length a and $\Delta Z_f(r_i)$ were expressed as

$$a = \sqrt{(f^2 - r_i^2)} \quad (4.17)$$

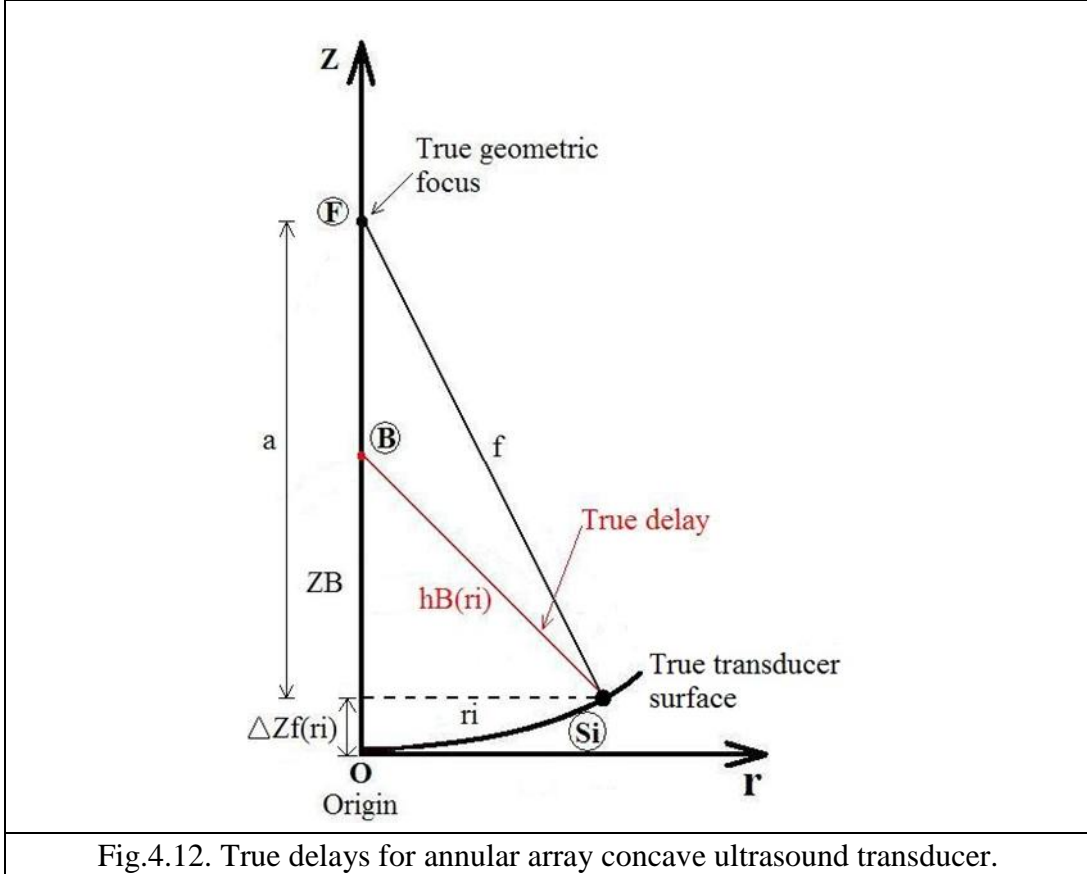
$$\Delta Z_f(r_i) = f - \sqrt{(f^2 - r_i^2)} \quad (4.18)$$

The coordinates of annulus locations S_i was expressed as

$$S_i = \{(r_i, \Delta Z_f(r_i)), i = 0,1,2,3,4,5,6,7\} \quad (4.19)$$

The true delays were defined by

$$\text{True delays} = \frac{\overline{BS_i}}{c} = \frac{h_B(r_i)}{c} \quad (4.20)$$



Here, the true delays $h_B(r_i)$ were expressed as

$$h_B(r_i) = \sqrt{[Z_B - \Delta Z_f(r_i)]^2 + r_i^2} \quad (4.21)$$

The difference between the true delays and the required delays in terms of the path lengths was given by

$$\Delta h_B(r_i) = h_B(r_i) - Z_B = \sqrt{[Z_B - \Delta Z_f(r_i)]^2 + r_i^2} - Z_B \quad (4.22)$$

Therefore, the fixed delays for annulus r_i could be applied in order to focus at point B , such fixed delay were given by

$$\text{fixed delays} = \Delta h_B(r_i)/c \quad (4.23)$$

In the dynamic focusing case, the delays to each annulus would be a function of time. This was because the shallower targets, including ultrasound scatters and photoacoustic absorbers, would return signals to the annular array concave ultrasound transducer earlier than the deeper locations. For ultrasound imaging, the dynamic receive beam-forming was given by

$$\Delta t(t, r_i) = \frac{\sqrt{(ct/2 - \Delta Z_f(r_i))^2 + r_i^2} - (ct/2)}{c} \quad (4.24)$$

Where the signal transit time along the z-axis was given by

$$t_{2-way} = \frac{2Z_B}{c} \quad (4.25)$$

$\Delta t(t, r_i)$ was a dynamic time delay applied to the received signals from annulus i ; $\Delta Z_f(r_i)$ was the height of the annulus, and r_i was the radius of annulus i .

For photoacoustic imaging, the dynamic receive beam-forming algorithm was given by the following equation,

$$\Delta t(t, r_i) = \frac{\sqrt{(ct - \Delta Z_f(r_i))^2 + r_i^2} - ct}{c} \quad (4.26)$$

Where the signal transit time along the z-axis was given by

$$t_{1-way} = \frac{Z_B}{c} \quad (4.27)$$

4.10 Main lobe relative to maximum side lobe level

It should be noted that dynamic-receive beam-forming alone without the aid of geometric focusing cannot achieve high-NA/low-f-number focusing without image-quality-degrading sidelobe artifacts. Our simulations above demonstrate that high-resolution, good depth-of-field imaging is possible, facilitated by both high-NA geometric focusing and dynamic-receive focusing. However, we wanted to quantify how sidelobe levels are affected by choices of geometric focus. By applying the dynamic beam-forming algorithm mentioned before, we studied the main lobe relative to maximum side lobe level at different point-absorber locations by simulating annular array transducers with different geometric focal lengths for photoacoustic imaging. All these simulated annular array transducers had eight annuli and the same aperture size, but they all had different focal lengths.

There was one simulated piston annular array transducer with infinite focal length and the other concave annular array transducers had focal lengths of 8 mm, 10 mm, 12 mm, 14 mm, and 16 mm respectively. These simulated annular array transducers were used for photoacoustic imaging scatters located at different position. At each scatter position, the value of main lobe relative to maximum side lobe level was plotted in figure 4.13.

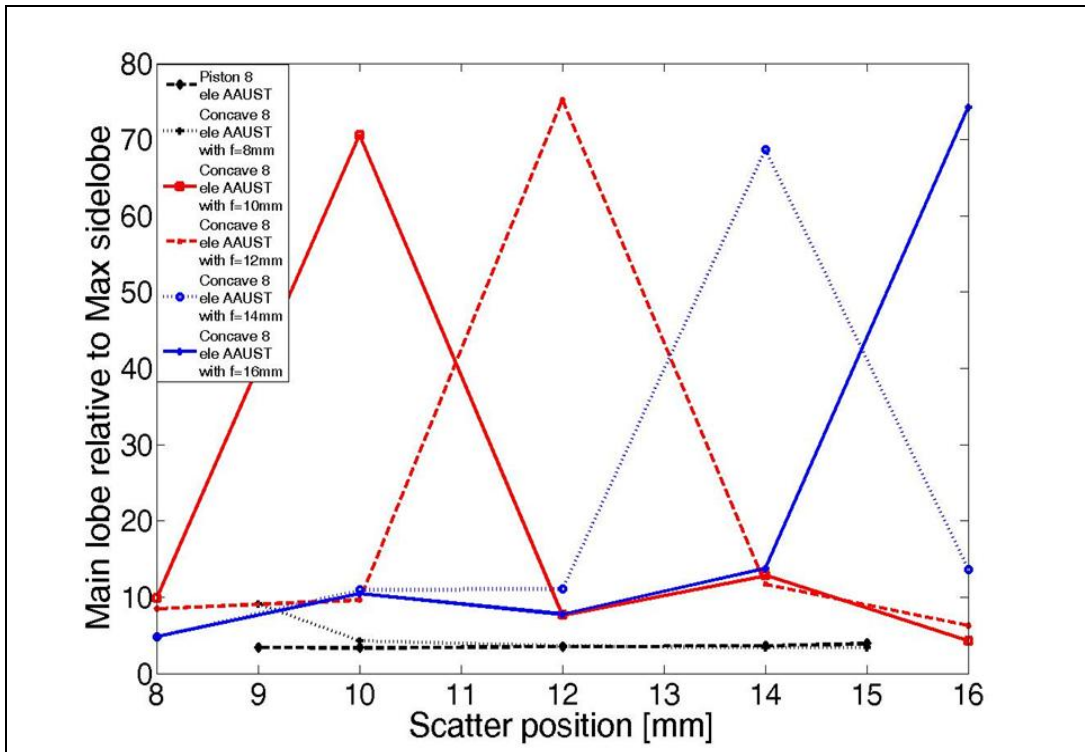
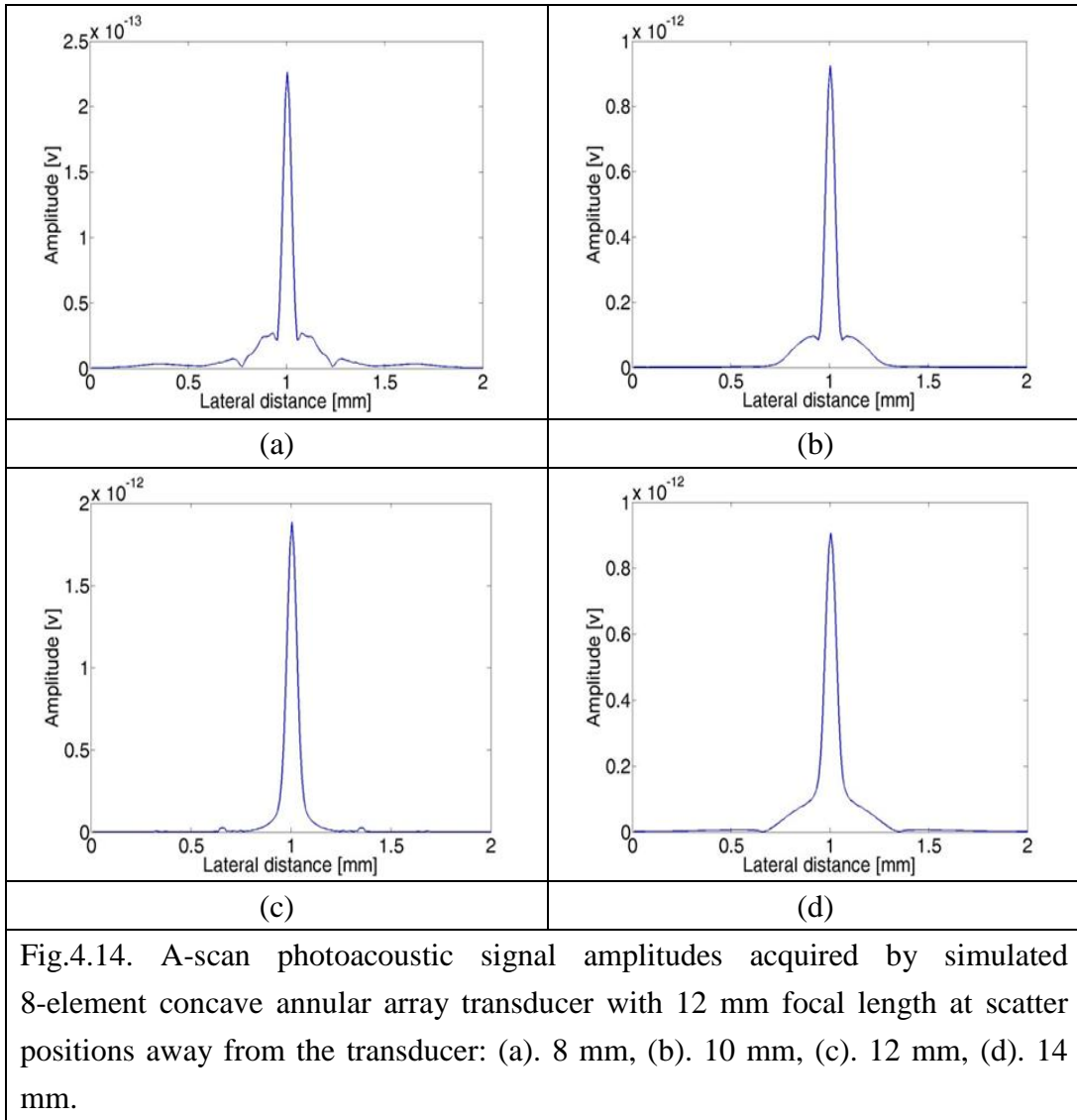


Fig.4.13. Main lobe relative to maximum side lobe for each scatter location by simulated annular array transducers with different focal lengths.

At each scatter position, these main lobe and side lobe values were chosen based on the plots shown in figure 4.14. Here the y-axis represents the maximum cross-range amplitude while the x-axis is the lateral distance. Maximum sidelobe levels were chosen by estimating the amplitude of the largest local maximum away from the mainlobe.

Fig.4.13 shows that even though a large depth-of-field may be possible using the annular arrays, the sidelobe levels quickly degrade away from the geometric focus of the transducer. Sidelobe levels for planar annular arrays with no geometric focus have quite poor sidelobe levels. We decided to fabricate annular arrays with 12mm focus because mainlobe-to-sidelobe levels are comparable with other focal depths, while high resolution is possible, facilitated by the large NA. To our

knowledge, this is the first study of its kind which has analyzed simulated performance of high-frequency annular arrays for photoacoustic imaging, and the principles and methodology used here may be applicable to many other systems.

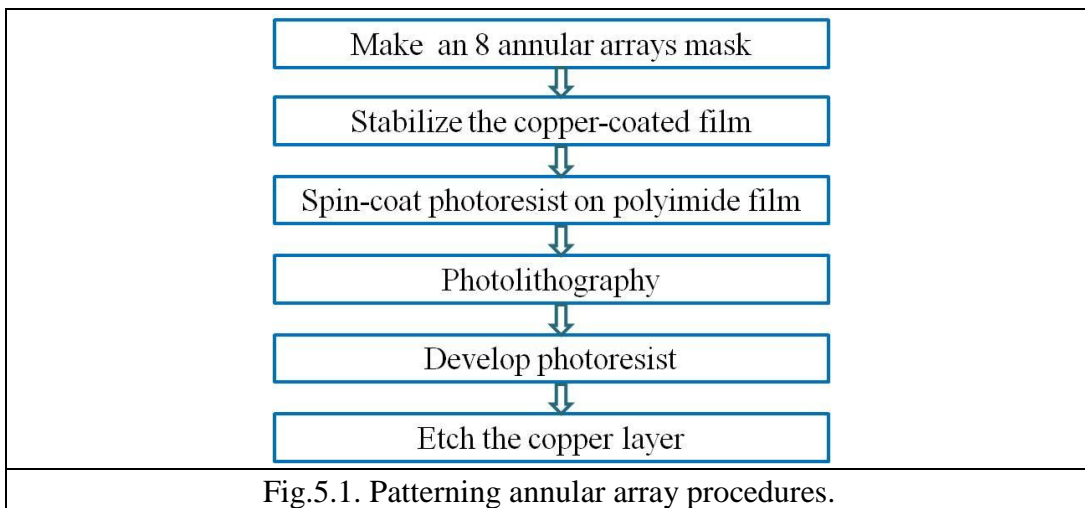


Ch5: Annular Array Concave UT: Fabrication and Characterization

We chose to fabricate our high-frequency high-numerical aperture annular array transducers using an approach similar to Ketterling and Lizzi. We discuss our fabrication process in this chapter and discuss differences between our work and theirs.

5.1 Pattern (copper-coated) Polyimide film

Photolithography was the key method used to form the annular array pattern on the one side copper-coated polyimide film. An annular array with eight elements mask was fabricated first and used later in the lithography process. The general patterning process of the annular array is illustrated in figure 5.1.



5.1.1 Annular array mask design

Based on the annular array active aperture simulation, all the radiuses of the annular annuluses were calculated to ensure that each annulus had the same area. In the mask, the most outer annulus diameter was 12 mm, the lead width was 75 μm and lead space was 100 μm . The contact pads were 5 mm long and 1 mm wide, and the space between them was 250 μm . The annular array mask was designed using L-Edit (Tanner Research, Monrovia), which is a software program used for mask design with multiple layers. In this case, only one mask layer was needed for patterning the annular array shape on the polyimide film. L-Edit has many basic shape icons in its tool bar for drawing different design shapes. L-Edit has a unique property called hierarchal design, which allows inserting or reusing the simple design in one cell 1 in other cells if they are higher in the design

hierarchy. This function was very beneficial and efficient in the construction of the mask, as only the initial cells needed to be changed for modifying the design in the final cells. All the mask designs were created in the cells with specific names. All the design shapes could be moved, stretched, edited, and deleted like other Windows programs. The mask design must be placed at the center of the substrate.

The following functions and procedures were used in L-Edit software. “Show cells and hierarchy” was used to quickly review all the created cells and the inserted cells. The “instance command” was used to insert a previous cell design into the present cell and future cells. If the original cell was modified, all the other cells containing this cell were modified automatically.

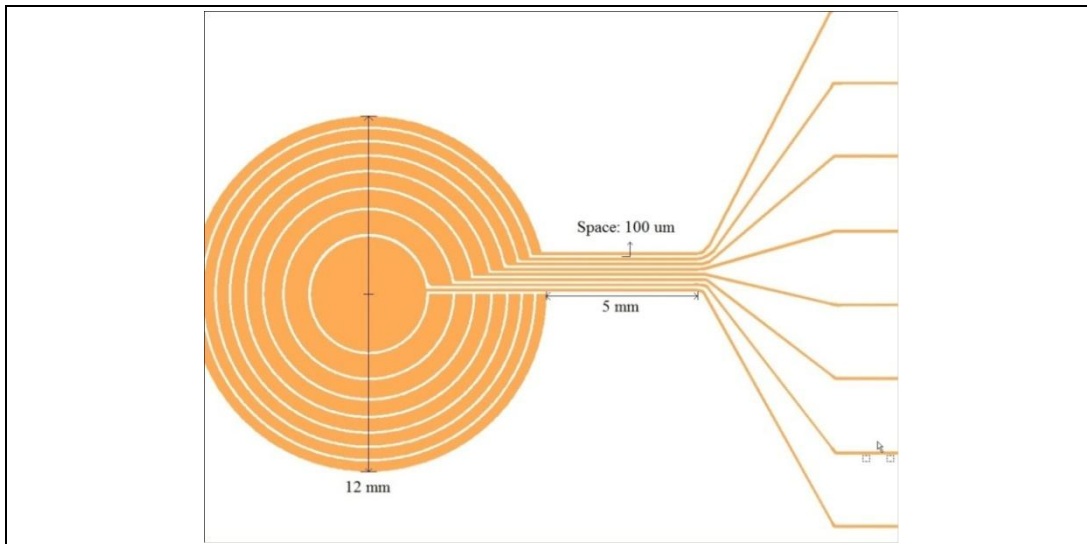


Fig.5.2. Main aperture of the annular array mask.

The “show design units” was used to illustrate the distance between each object in a specified unit, showing the accurate value. As mentioned, there were “seven basic building shapes” used for drawing the final mask design. There were other useful functions like zoom in and out. It was important to never use the “wires, lines and dots” functions, because the GDSII format could only accept 3 or more vertexes shapes [78].

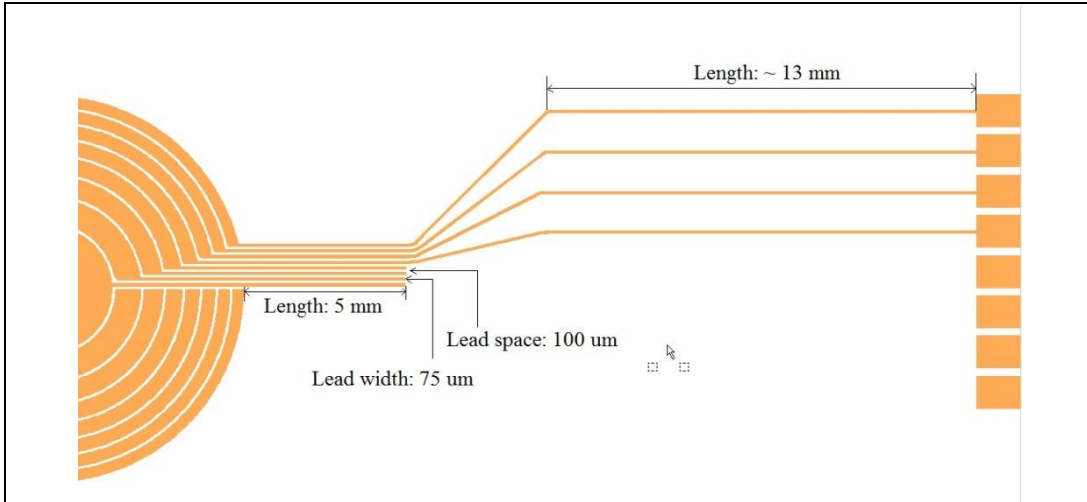


Fig.5.3. Annular array lead width and space.

After the mask design was finished in L-Edit, the design .tdb file was exported to a .gds file. This was done by selecting the “export mask data” in the file menu and setting the “export file type” to the GDSII format. At this stage, the mask design was ready for fabrication. Figure 5.2 shows the main aperture of the annular array mask with a 12 mm aperture diameter. Figure 5.3 shows the lead width and space of the annular array mask.

The ground pads were added among each power lead to prevent cross talk, as shown in figure 5.4.

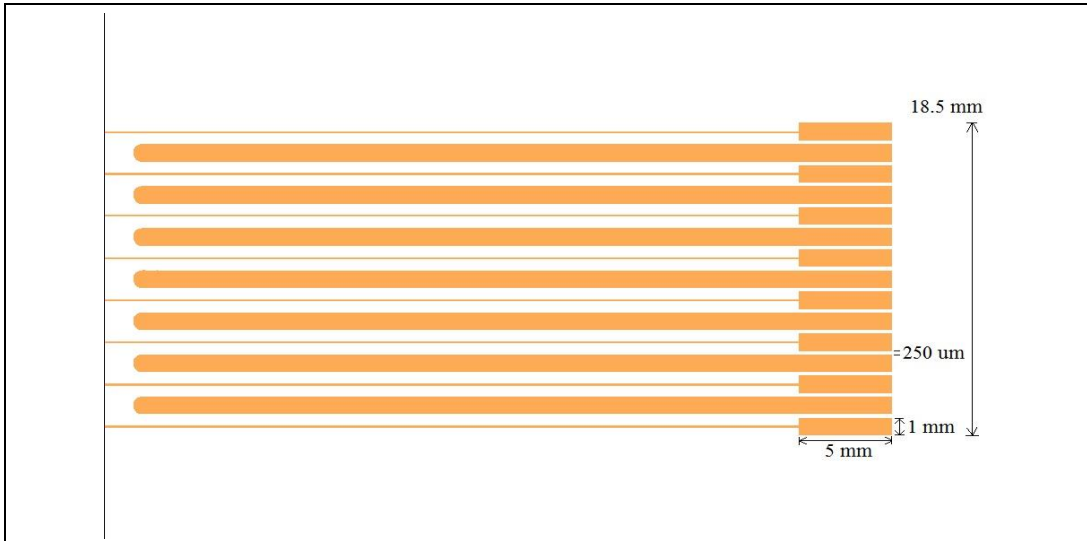
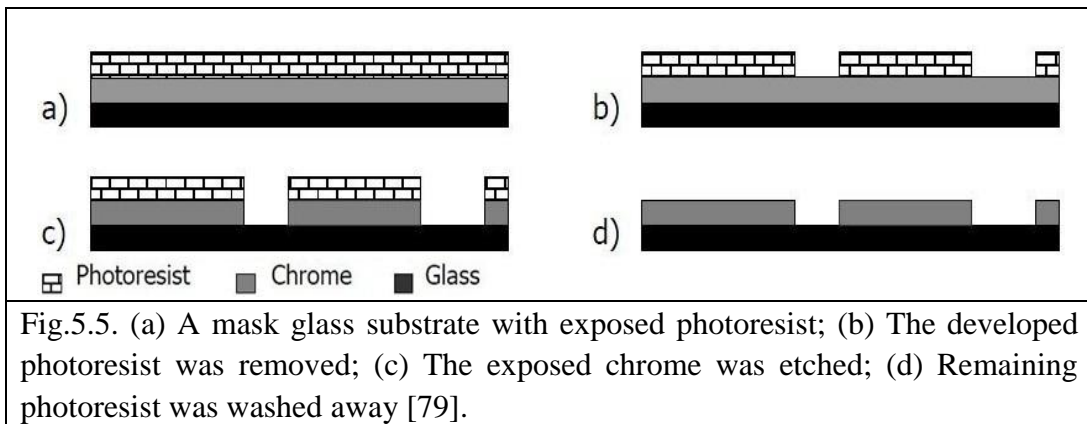


Fig.5.4. Annular array ground pads and connector pads.

The Heidelberg direct write laser (DWL) 200 Pattern Generator was used to fabricate the annular array mask. This system can quickly produce high quality

photo masks precisely and accurately. It uses four Krypton-Ion laser beams at a wavelength of 413 nm to write the mask pattern using a raster scolding motion. It saves time by skipping the areas that do not need be written. The minimum feature size this system can write is in the range of 0.7 to 0.8 μm . A piece of glass with a chrome layer and a pre-coated photoresist layer was usually used as the photo mask substrate. In this case, the minimum feature size was 75 μm . Due to isotropic chemistry during the developing and etching processes, the actual design feature size was always smaller than the one on the mask. Usually, the difference was $\pm 0.7 \mu\text{m}$. The annular array mask GDSII file was converted to LIC file that could manage the DWL 200 Pattern Generator for controlling laser movement. Based on the converted file, the annular array was chosen to be a positive mask [79].

After the adding photoresist, the chrome layer of the mask was exposed using a Krypton-Ion laser (Infinite Graphics, Minneapolis, CA) which altered the chemical property of the exposed part. After developing, the laser exposed photoresist was removed. In order to prevent removing feature sizes less than 5 μm , the photoresist was typically developed every 20 seconds and was inspected for a satisfactory finish. After the developing process, the mask substrate was put through the etching process. The remaining photoresist would prevent etching of the chrome beneath it, and the exposed chrome was etched away, forming the designed mask pattern. The final step was to properly clean the mask before using it in traditional lithography. The remaining photoresist was totally removed by acetone and IPA. Figure 5.5 illustrates all the steps for fabricating a mask [79].



Following the mentioned mask fabrication steps, our 8-element annular array mask was fabricated by the Nanofab in University of Alberta and was shown in figure 5.6.



Fig.5.6. Fabricated annular array mask.

5.1.2 Photoresist deposit

The flex circuit material (3 Fu Technology, Shenzhen, China) was 25 μm thick polyimide film with a 14 μm thick copper layer coated on one side. The flex circuit material was taped on a standard size silicon wafer for supporting purposes, copper side up. The positive broadband HPR 504 photoresist (OCG Microelectronic Materials, New Jersey, USA) was spin-coated (Solitec Wafer Processing, Milpitas, CA) on the copper layer of the polyimide film as shown in figure 5.7 [80]. The silicon wafer was placed on the chuck of the Solitec spinner and a vacuum grasp was used to stabilize the wafer. The spread speed was set at 500 rpm for 10 seconds and the spin speed was at 4000 rpm for 40 seconds. By using these parameters, the final photoresist thickness was approximately 1.5 μm [81].

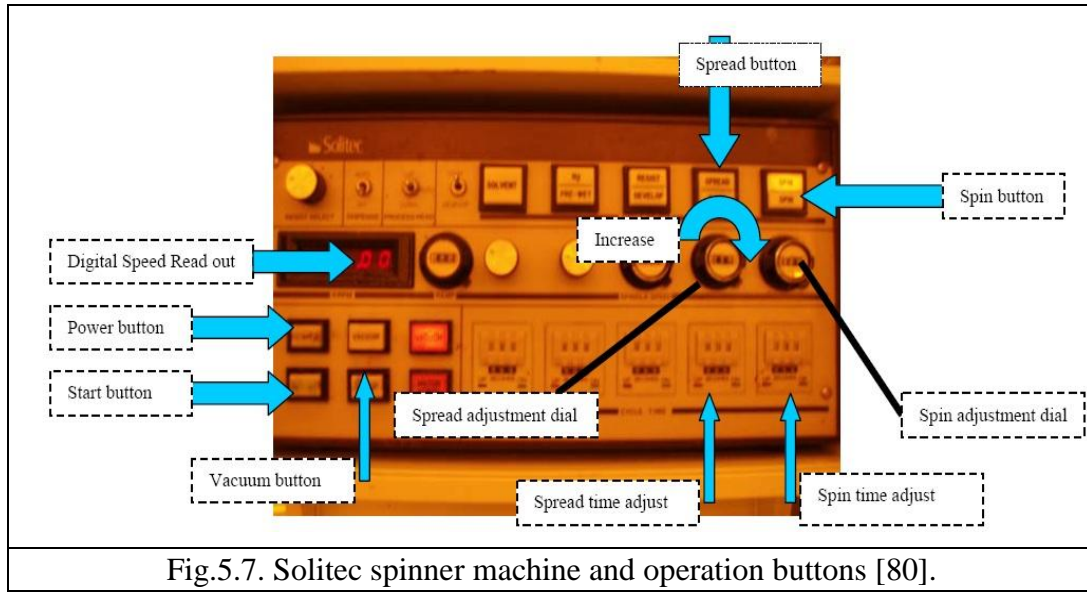


Fig.5.7. Solitec spinner machine and operation buttons [80].

5.1.3 Photoresist baking process

After spin-coating the photoresist, the one side copper-coated polyimide film was placed on the Solitec vacuum hotplate to bake the photoresist. Figure 5.8 shows a photo of the Solitec vacuum hotplate [82].



Fig. 5.8. Solitec vacuum hotplate [82].

This step is used to evaporate the solvent component from the photoresist which improves the adhesion on to the substrate. After the solvent was removed, the photoresist became hard and uniform which is ideal for patterning [83]. The hotplate was set to 115 °C and it takes approximately 30 minutes to warm up. The photoresist was baked for 90 seconds at this temperature. After baking the photoresist, the polyimide film was removed from the hotplate and placed on the metal rack to cool for 15 minutes. This cooling step was very important in

ensuring an effective lithography process for proper exposure and developing performance [84]. This step also allowed the photoresist to re-hydrate. The required rehydration time depended on the humidity of the environment.

5.1.4 Photolithography

The annular array mask was inspected for cleanliness prior to use in the photolithography step. It was placed onto the ABM mask aligner (ABM, Scotts Valley, CA) and the mask vacuum was turned on to hold the mask tightly. Figure 5.9 shows the ABM mask aligner system [85].

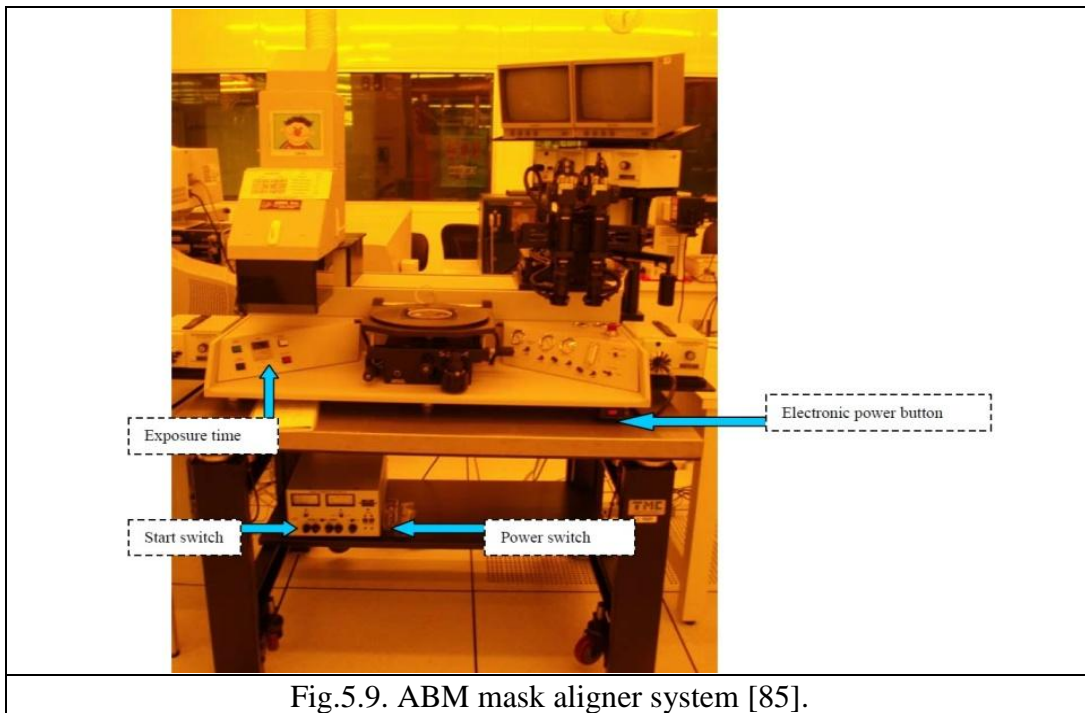


Fig.5.9. ABM mask aligner system [85].

Lifting the mask frame, the polyimide film on the silicon wafer was placed on the wafer chuck center. The substrate vacuum was turned on in order to stabilize the wafer during the lithography process. The control buttons of the mask aligner are shown in figure 5.10 [85].

The mask frame was then lowered and the substrate position was adjusted by the x and y dials to let the annular array mask completely cover the polyimide film surface so that the mask could be fully patterned. After the nitrogen flow was activated, the substrate was slowly raised while pressing the self levelling button until the wafer reached the maximum height close to the mask. By turning the small adjustment knob until the adjustment skipped, the silicon wafer made soft contact with the annular array mask.

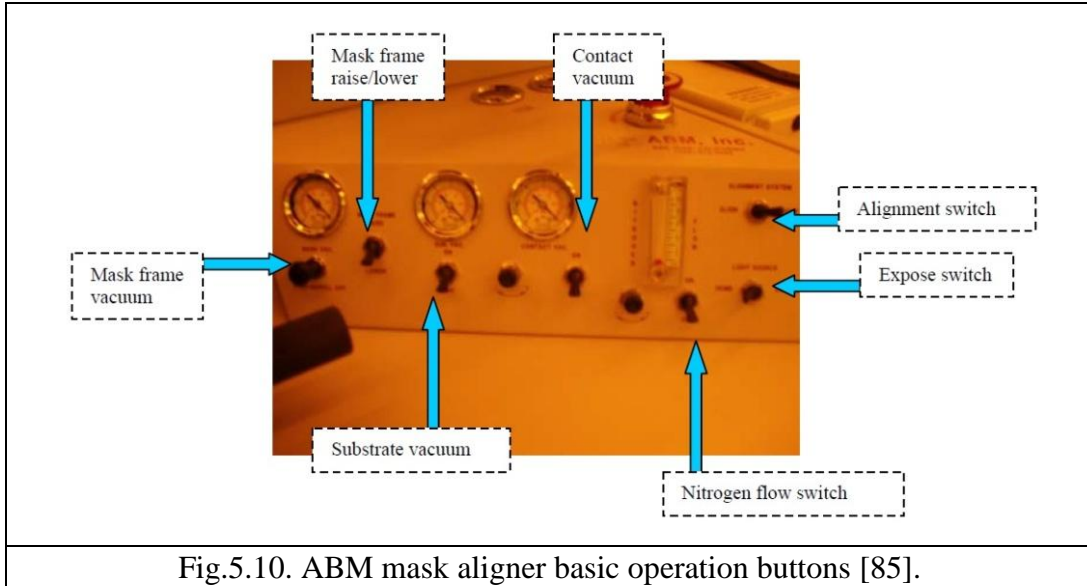


Fig.5.10. ABM mask aligner basic operation buttons [85].

Two additional turns of the small adjustment knob were made to ensure the proper contact. These x and y dials and knobs are shown in figure 5.11 [85].

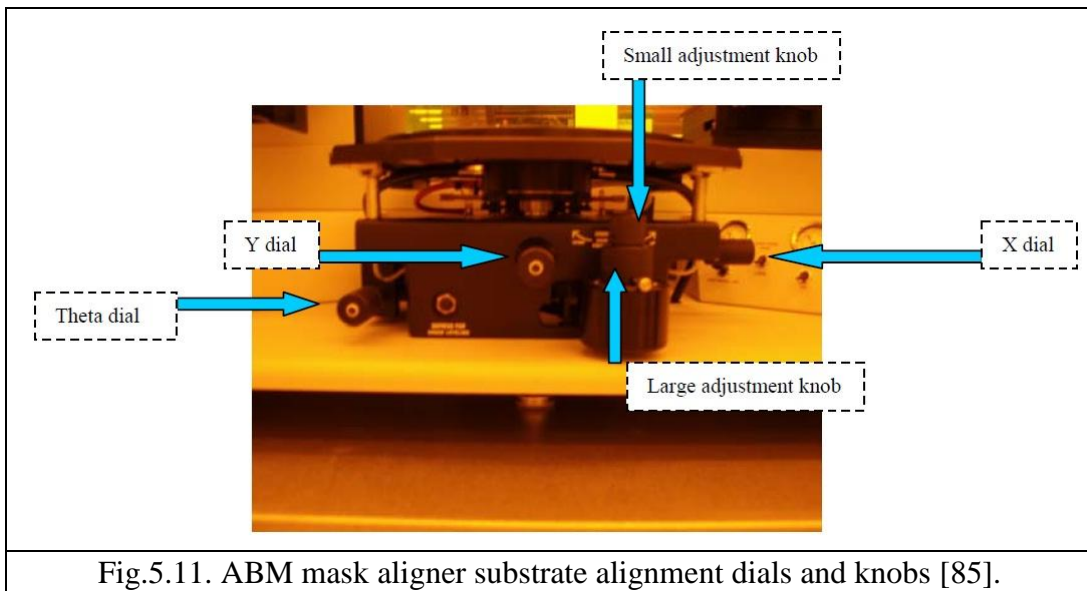


Fig.5.11. ABM mask aligner substrate alignment dials and knobs [85].

The substrate vacuum was cycled off and on to achieve a hard contact indicated by Newton's rings spreading across the wafer [85]. The exposure time was set for 3 seconds and the wavelength of the UV light was in the range from 350 to 500 nm [84]. When the exposure ends, the contact vacuum was turned off to release the contact between the wafer and the mask. The substrate vacuum was turned on to hold the released wafer. The smaller knob was used to gently lower the exposed polyimide film on the wafer first in case the film might stick to the mask. When the film was no longer in contact with the mask, the large knob was used to

completely separate the two. The substrate vacuum was turned off and the mask frame was raised up. After turning off the nitrogen flow and the mask vacuum, the annular array mask was removed. Using this process, the annular array mask was fully patterned on the one side copper-coated polyimide film.

5.1.5 Developing

The patterned polyimide film was put through the developing process to remove the photoresist previously exposed to the UV light. The developer used, Shipley Microposit 354 Developer, (Shipley, Coventry, United Kingdom), is a solution of water, sodium tetraborate, and sodium hydroxide [81]. The one side copper-coated polyimide film on the silicon wafer was put into the developer solution for approximately 10 seconds and taken out immediately, rinsed with water and dried with nitrogen gas. It was very important to remove the polyimide film substrate from the developer as soon as the annular array pattern was clearly visualized to prevent over developing, as the developer solution on the polyimide film surface still removes the photoresist that was exposed to UV light, resulting in loss of functional features. The developed polyimide film was inspected under the microscope to check the patterning and photoresist developing qualities. The features should have sharp and straight edges and there should be no undeveloped photoresist residues [83].

5.1.6 Etching

After the photoresist was well developed, the polyimide film was etched in an



Fig.5.12. Wet process for general use - WD Aisle #1 [86].

Iron (III) chloride, a standard copper etching solution. The patterned polyimide

film was soaked in the Iron (III) chloride etching solution for approximately 11 minutes. During the etching process, the dish container was gently agitated to help evenly etch the copper layer on the polyimide film. The etching process was operated at wet deck (WD) Aisle #1 as shown in figure 5.12 [86].

5.1.7 Stripping photoresist

When the copper layer on the polyimide film was properly etched, any remaining photoresist was completely removed using acetone and then rinsed with isopropyl alcohol (IPA). As the final step, the polyimide film was washed with water and dried with nitrogen gas. A digital impedance meter was used to test the connectivity between each pad and the annular array and to ensure no electrical shortages. Figure 5.13 shows two annular array patterned polyimide films.

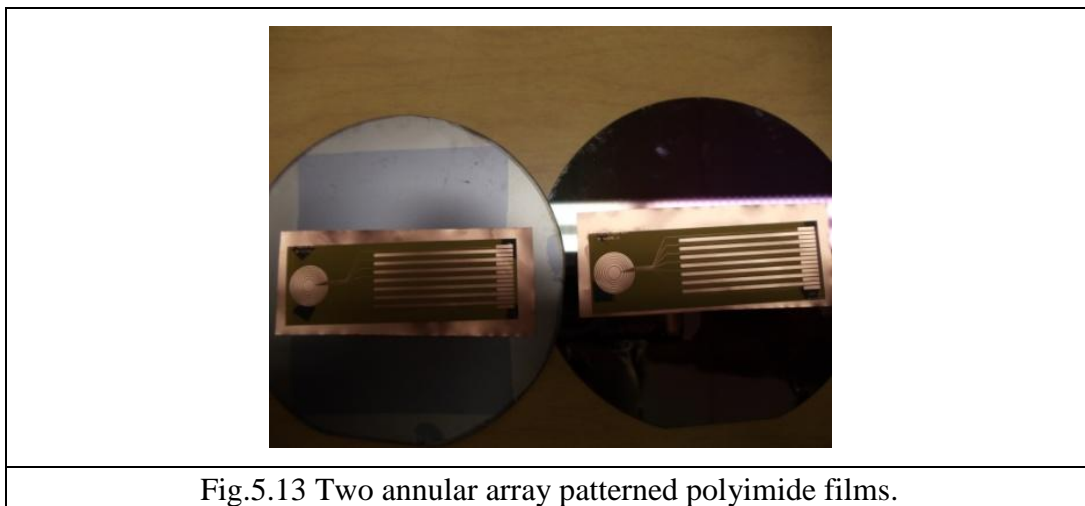


Fig.5.13 Two annular array patterned polyimide films.

5.2 Annular array concave ultrasound transducer fabrication

It was important to review the general structure of an ultrasound transducer before fabrication so that all the design parameters could fit into the blue print. Figure 5.14

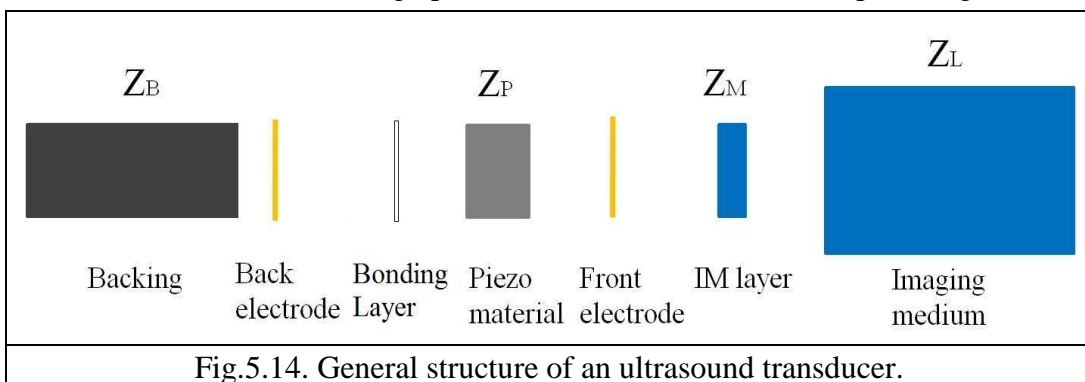
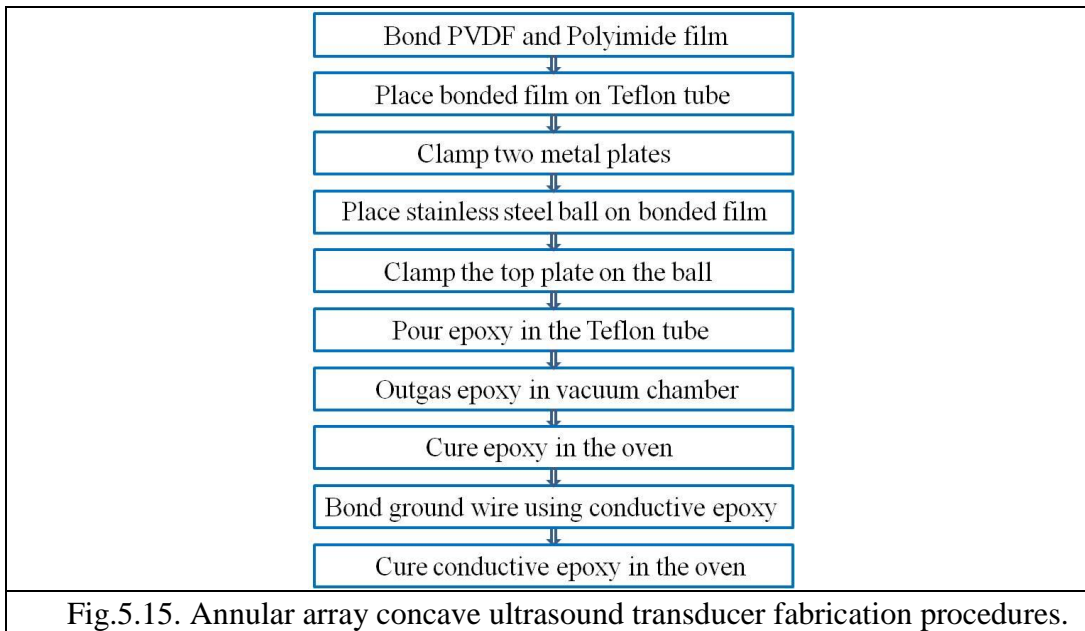


Fig.5.14. General structure of an ultrasound transducer.

shows the general structure of an ultrasound transducer and the imaging medium.

In our case, the backing material for the fabricated annular array concave ultrasound transducer was epoxy whose acoustic impedance was 2.9 Mega Rayleigh (MRay). The high frequency piezoelectric material was chosen to be PVDF film whose acoustic impedance was 3.9 MRay. Since the acoustic impedance of the backing material and the piezoelectric material was quite similar, half wavelength excitation of the piezoelectric material was assumed and used to calculate the piezoelectric material thickness for the desired centre frequency of interest. In order to achieve ultrasound frequency above 40 MHz, the thickness of the PVDF film should be less than 27.5 μm . The one side-coated polyimide film was patterned with the annular array shape and acted as the back electrodes. It is assumed that the limited thickness of this layer would not affect the backing impedance. The front electrode was the nickel layer on the PVDF film and also due to its thickness, assumed acoustically transparent. The small copper wire was used as an electrical connection to the front electrode). Because the acoustic impedance of PVDF was similar to the water imaging medium 1.5 MRay acoustic impedance, there was no need of an impedance matching (IM) layer. The annular array concave



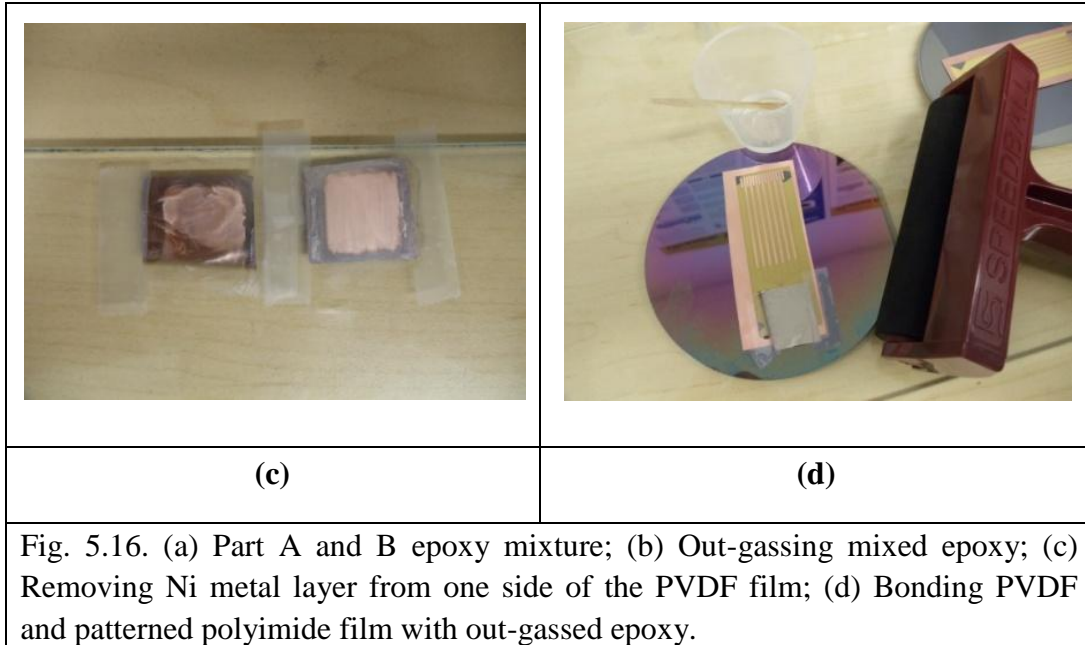
ultrasound transducer fabrication method was similar to the one used by a previous research group [70]. The most important construction tool consisted of three aluminum metal plates forming a press-fit system in order to press the film into a concave shape. Figure 5.15 illustrates the annular array concave ultrasound transducer fabrication procedures.

5.2.1 Fabrication materials

PVDF and one side copper-coated polyimide film were the two materials used for annular array concave ultrasound transducer fabrication. PVDF is a good acoustic receiver that has a low acoustic impedance and has been widely used as a piezoelectric material for making high frequency transducers with large bandwidth and good impedance matching properties [70]. The PVDF used in this study (1003702-7, Piezo Sensors, Inc., Hampton, USA) was 9 μm thick and both sides were coated with a 1 μm thin layer of nickel. In order to use the array copper as the second electrode, the Ni metal layer from one side of the PVDF film was removed using acetone to leave only one Ni metalized side as the ground plane. The polyimide film was 25 μm thick. The copper layer coated on one side of the polyimide film was 14 μm thick and was patterned and etched to form the bottom electrodes with the annular array shape as described previously. These two films were bonded together with a thin layer of out-gassed epoxy to form the core material for the annular array concave ultrasound transducer.

5.2.2 Film bonding





Non-conductive and conductive epoxies used in the procedure were purchased from Paisley Products, Toronto, Canada. The non-conductive epoxy (Epotech 301-2, Epoxy Technology, Billerica, USA) part A was mixed with part B in a certain ratio and a vacuum chamber was used to outgas the epoxy mixture at 1250-mTorr. A tiny drop of the out-gassed epoxy was used to bond the PVDF (Ni-removed side) and the patterned one side copper-coated polyimide film together. A roller was used to minimize the epoxy thickness between the two films. The Teflon tube with 12 mm inner diameter was inserted through the center hole of the sample holding plate. The combined film was centered on the Teflon tube and was diagonally stretched by four pieces of plastic tape to ensure a flat surface. A Teflon ring embedded in the membrane clamping plate was placed on the combined film and the two plates were tightened together by three bolts and nuts. A stainless steel ball was placed on the combined film through the center hole of the membrane-clamping plate to form the concave shape of the transducer. The top plate was placed on the stainless steel ball and was tightened together with the other two plates. Figure 5.16 illustrated these steps.

5.2.3 Press-fit assembly

The fabrication method used was based on a previous research group's fabrication process of a 40 MHz annular array transducer [70]. To form the piezoelectric film into a concave shape, a similar press-fit assembly was used. The press-fit system included three aluminum plates, a Teflon ring and a Teflon tube. The three

aluminum plates were: 1 - sample holding plate; 2 - membrane or film clamping plate, and; 3 - a top plate. Note, each plate had three clearance holes in a triangle

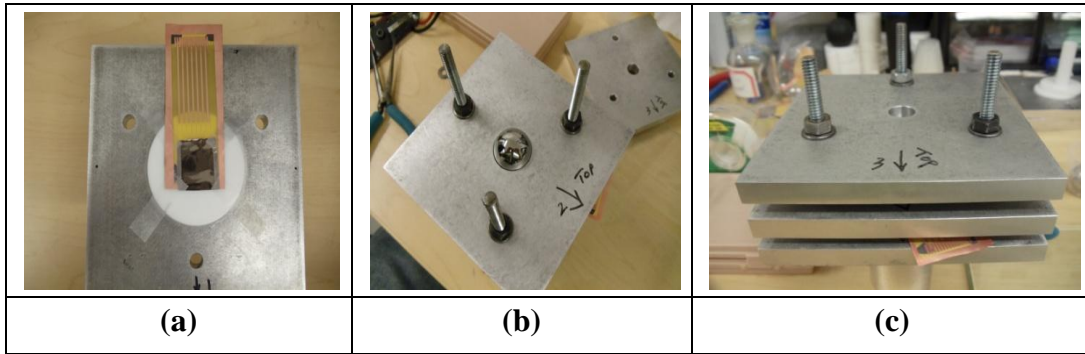


Fig.5.17. (a) Bonded film stretched on the Teflon tube; (b) Stainless steel ball pressing on the boned film; (c) Top plate clamping the ball.

configuration. There were two counter sinks at the center of the sample plate and the film clamping plate for fitting the Teflon tube and the Teflon ring respectively. The Teflon tube was inserted in the sample plate hole and the Teflon ring in the membrane clamping plate could clamp the film tightly, preventing epoxy from leaking out. A stainless steel ball was used to form the concave shape in the PVDF/polymide film by clamping the ball between the top metal plate and the second plate. Using this press-fit assembly, a concave ultrasound transducer front aperture was finally achieved as well as a cylindrical epoxy backing with a concave front. Figure 5.17 showed the press-fit assembly system and three fabrication steps.

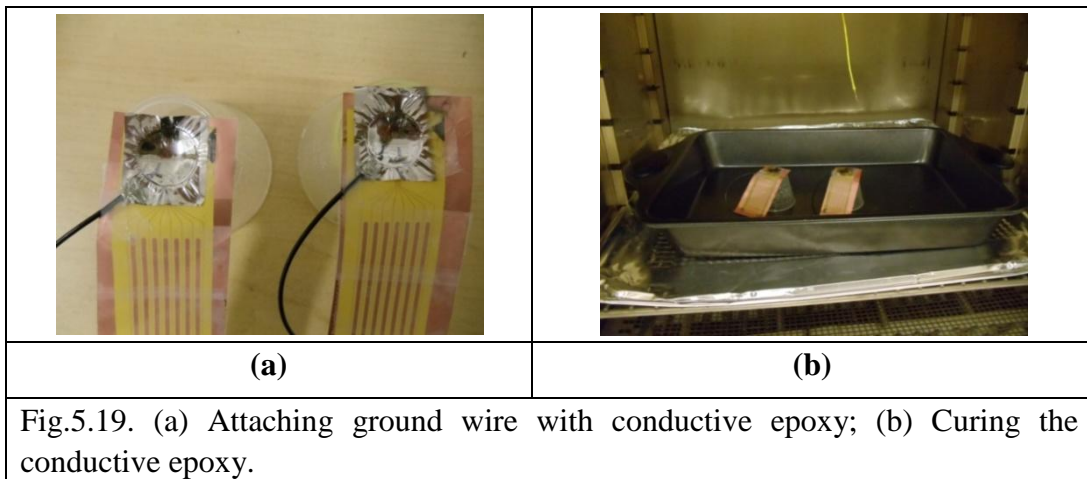
5.2.4 Epoxy backing



Fig.5.18. (a) Pouring out-gassed epoxy into the Teflon tube; (b) Out-gassing epoxy again.

The press-fit system was then flipped over, and the previously out-gassed epoxy was poured into the Teflon tube. The whole press-fit assembly containing the epoxy in the Teflon tube was put in the vacuum chamber at 1250-mTorr again to ensure no air was between the epoxy and the polyimide film. This epoxy formed the backing part of the annular array concave ultrasound transducer. In order to cure the epoxy, the press-fit system was heated in an oven at 60 °C for 5 hours. All these fabrication steps were shown in figure 5.18.

5.2.5 Wire attachment



After the epoxy was cured, conductive epoxy (Epotech H20E, Epoxy Technology etc) was used to connect the ground wire to the PVDF front (ground) electrode and was heated in the oven at 70 °C for 5 hours as shown in figure 5.19.

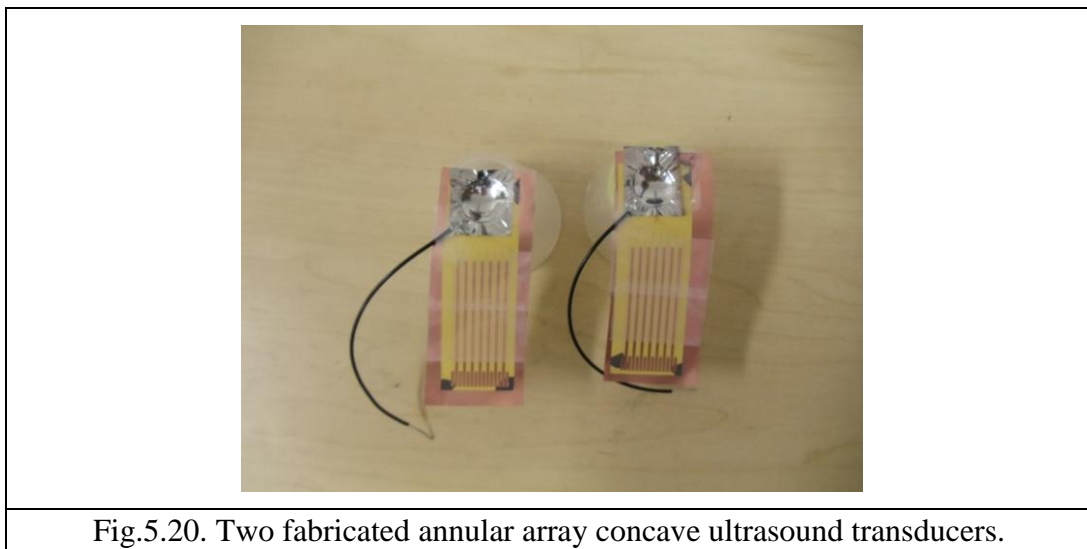


Figure 5.20 shows two successfully fabricated annular array concave ultrasound transducers. These fabricated annular array transducers were later tested for their performance and characterization.

5.3 Annular array concave ultrasound transducer characterization

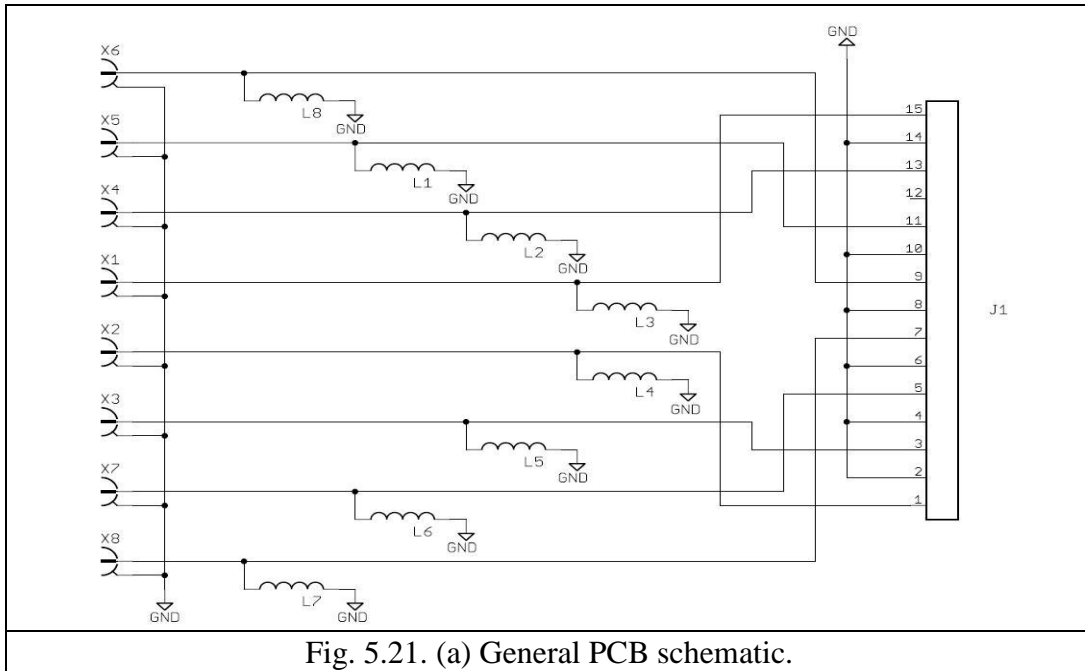


Fig. 5.21. (a) General PCB schematic.

5.3.1 PCB board design

In order to electrically connect to the flex circuit of the patterned annular array polyimide film, a printed circuit board (PCB) board was designed and fabricated, containing 15 through holes for mounting the ZIF flex circuit connector with seven ground pins and eight positive pins, and eight mounting holes for the eight right angle Sub miniature version A (SMA) connectors. On each of the eight electrical traces, there was pad space for mounting an inductor to remove electrical noise. Figure 5.21 (a) shows the general schematic of the PCB and figure 5.21 (b) shows the orientation of the connector for each ring and the PCB dimension.

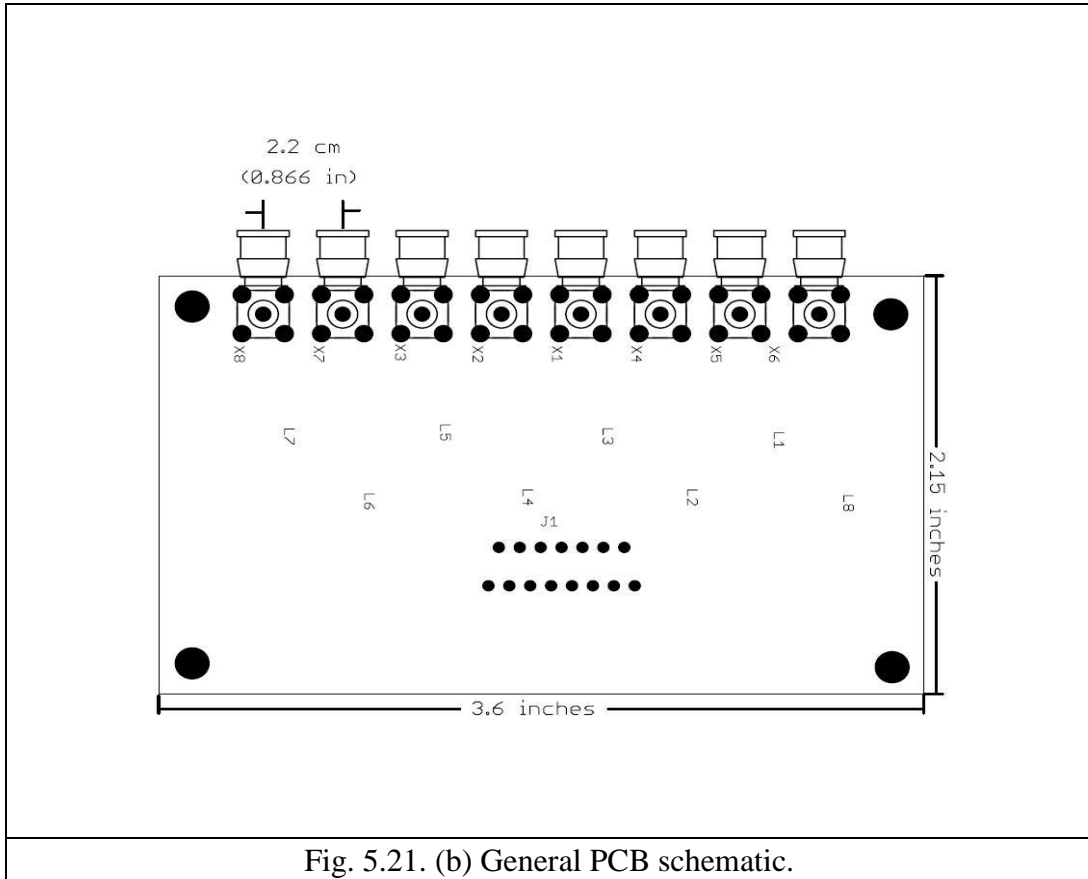
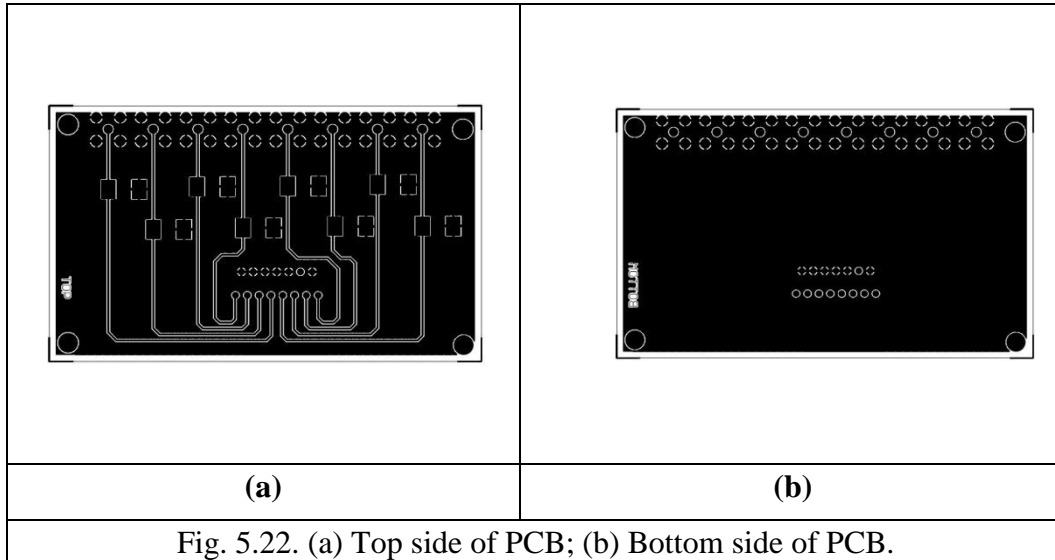


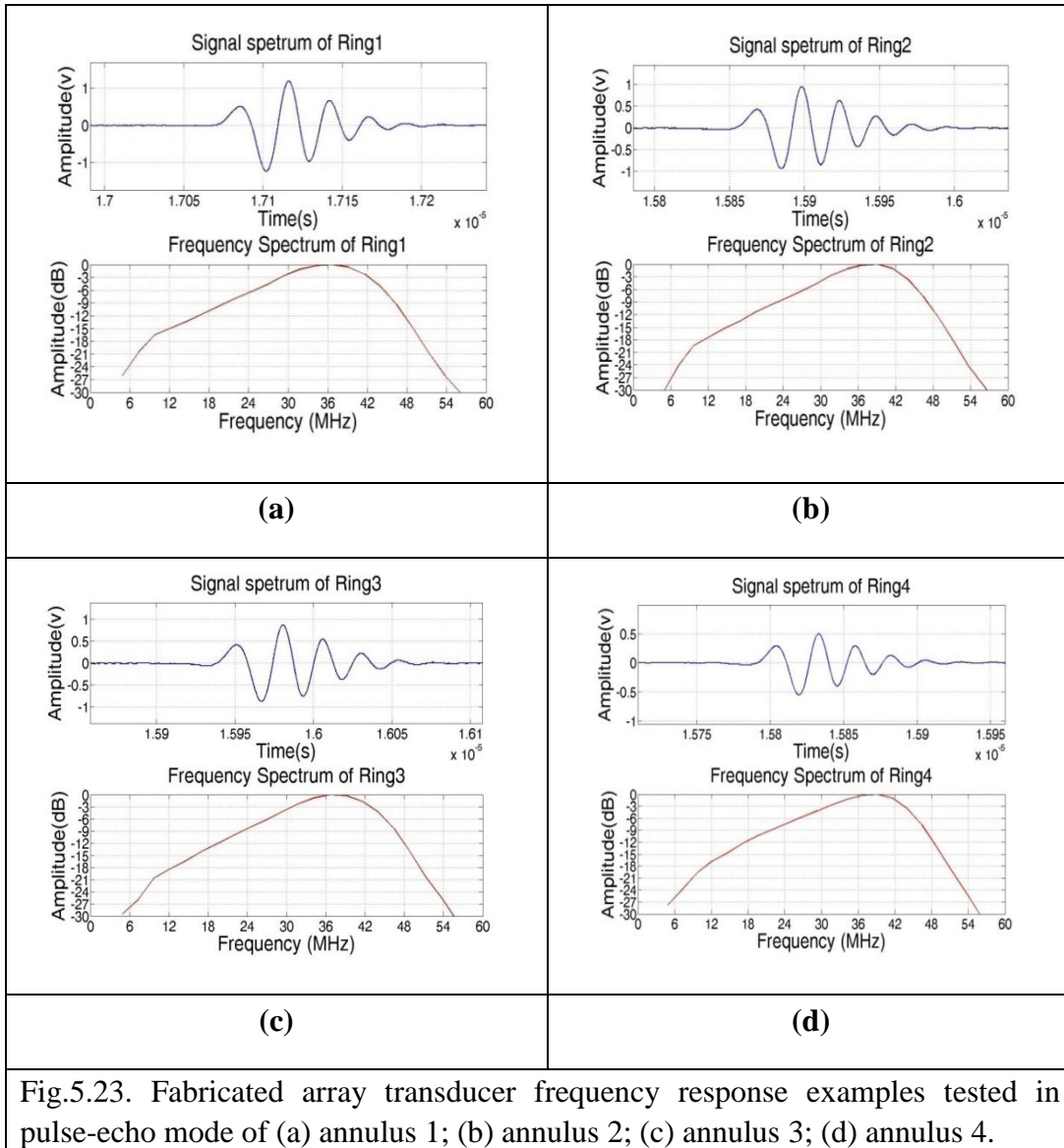
Fig. 5.21. (b) General PCB schematic.

This PCB had double-sided ground layers. Figure 5.22 shows both the top and bottom layers of the PCB. There four mounting holes at the four corners on the PCB for mounting it on the PCB holder. These eight SMA right angle PC mount connectors (Digi-Key Corporation, USA) were used to connect the eight annuluses through the PCB to the eight channels on the multi-channel scope. The 15 pins ZIF flex circuit connector (Adam Tech, New Jersey, USA) was used to connect the 15 pads on the patterned annular array polyimide flex circuit to have electrical connection with the positive traces and ground plane on the PCB.



5.3.2 Fabricated annular array concave ultrasound transducer testing

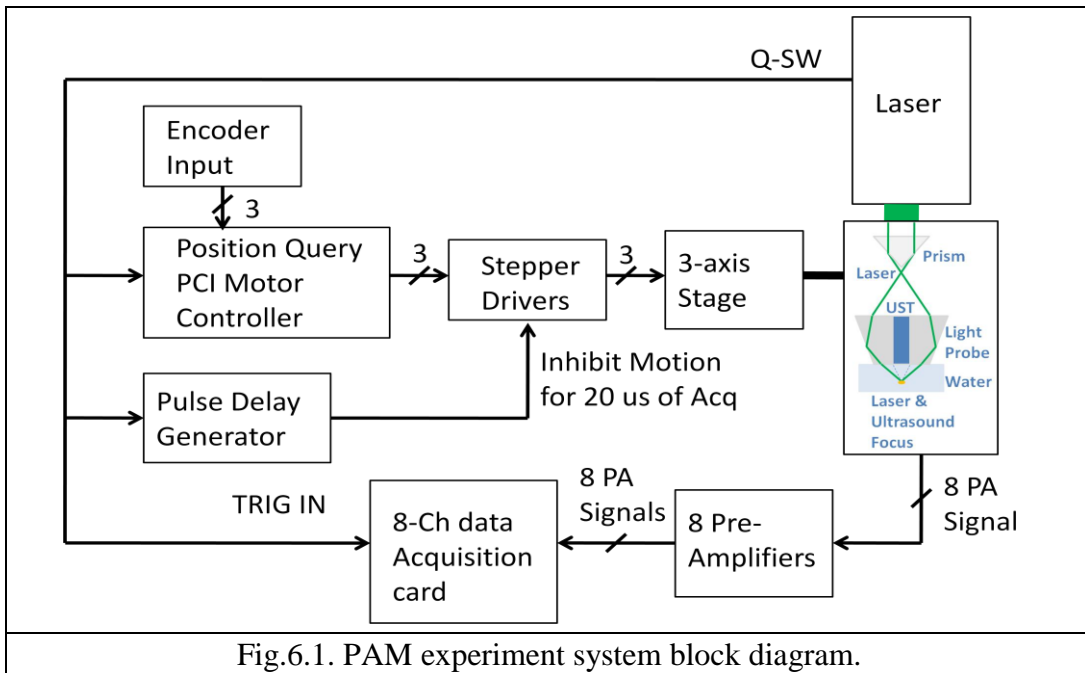
Each individual annulus was connected to a pulse-receiver (5073 PR, Olympus NDT Inc., WA, USA) to test its performance in the pulse echo mode. The pulse-echo experiments were performed in a water-bath using a stainless steel plate acoustic reflector placed at the acoustic focus of the transducer. Received echo signals and their corresponding spectra are displayed in figure 5.23. These results demonstrated a wide bandwidth response with peak frequency amplitude occurring near 40 MHz. Testing results as shown in figure 5.23, illustrated that each annulus had achieved the expected high frequency response, proving that the annular array concave ultrasound transducers were successfully fabricated. For simplicity, only four of the frequency response spectrums by these eight annuli are demonstrated here.



Ch 6: Photoacoustic Microscopy Experiments, Limitations and Proposed Solutions

6.1 PAM experiment setup

Having fabricated our annular array concave ultrasound transducers, we next evaluated their performance for PAM imaging. We used a laser system as our light source and each annular annulus was connected to a data transfer channel on a multiple data input and output card. We placed hair and carbon fibers at different depth relative to the fabricated annular arrays as phantom targets and applied our dynamic receive beam-forming algorithm to the received photoacoustic signals to demonstrate improved imaging depth of field. Our photoacoustic experiment setup was shown in figure 6.1.



A tunable optical parametric oscillator (Surelite OPO Plus, Continuum, Santa Clara, California) was pumped by a Q-switched Nd:YAG laser (Surelite III, Continuum, Santa Clara, California). The laser wavelength we used in our experiment was 532 nm with 10 Hz pulse repetition rate, providing ~5 mJ per pulse of energy. The Q-switch out from the laser triggered the PCI motor-controller card to query the scan position via encoders. The Q-switch also triggered an 8-channel data acquisition card. During our experiment, the motor drivers produced a significant amount of noise in our PA signals, so we used a delay generator to use the Q-switch out trigger to inhibit the motors for 20 μ s

when the Gage data acquisition card (Octopus 8289, Gage Applied Systems, Inc., IL, USA) acquired data. In this way, the noise from the stepper motors was dramatically reduced. We used this system setup to produce photoacoustic images of hair and carbon fibers, using the fabricated annular array concave ultrasound transducer. Our photoacoustic microscopy (PAM) experiment setup is shown in the following system block diagram. The signals were received by the annular array concave ultrasound transducer through eight annuli and proportionally amplified by eight low noise amplifiers (ZFL-500LN+, Mini-Circuits, Brooklyn, USA). These amplifiers could provide ≥ 24 dB gain to the input signals. The digitized amplified signals were subjected to a dynamic receive beam-forming algorithm for final image reconstruction.

6.1.1 Laser and optical system setup

The laser provided the light source and becomes the master trigger in our PAM experiment system as mentioned before. The laser beam was guided and reflected using several optical lenses to achieve an ideal incident angle to shine on the right angle prism as shown in figure 65. The laser beam was reflected by the prism to vertically shine on the light probe and eventually on the target. The laser beam energy was also filtered through these optical lenses to provide approximately 5 mJ per pulse of energy. The laser triggered the PCI motor controller, pulse delay generator, and the 8-channel data acquisition card in order to synchronize the whole photoacoustic data acquisition process up to ± 1 clock cycle of the data acquisition card. The clocks of these instruments were not synchronized, but could be in the future. At each scan position, we acquired A-scan data from the target, and at the end of the scan, these A-scan data were dynamically focused to construct a B-scan image.

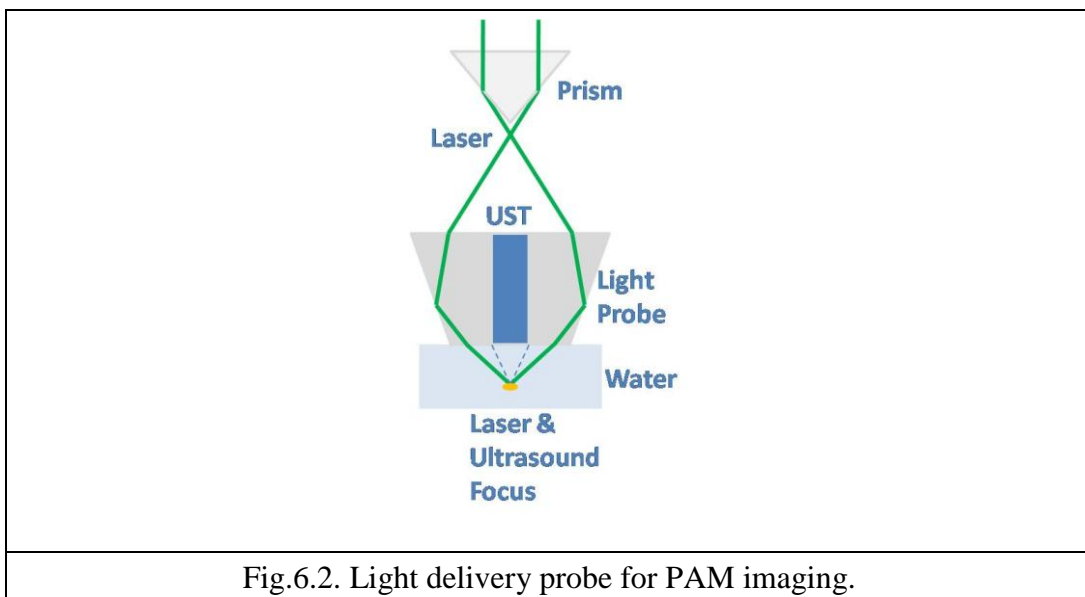
6.1.2 3-axis stage

We used a 3-axis stepper-motor-driven stage to perform mechanical scanning of the transducer and light delivery probe. We used a closed loop positioning system consisting of stepper-motor-drivers (MBC25081, Anaheim Automation, Anaheim, CA), stepper motors (23Y002D-LW8, Anaheim Automation, Anaheim, CA) and linear optical encoders for each stage. We used a PCI card (7330, National Instruments, Quebec, CA) to control the scanning trajectories using custom software. The three encoders (LIE4, Numerik Jena GmbH, Jena, Germany) could send feedback signals to the PCI card for tracking current scan position and direction. The PCI motor controller and the stepper drivers were triggered by the laser. Therefore, the overall scanning speed was controlled by the laser pulse

repetition rate. Using the 3-axis scanning system, we could achieve B-scan and C-scan motion trajectories.

6.1.3 Light probe design

Our experimental setup for photoacoustic microscopy was similar to that described in [20]. In order to achieve maximum photoacoustic signal, the ultrasound and optical foci need to be co-aligned. Our dark-field illumination scheme was similar to previous work [87]. Since the ultrasound focus was at 12mm depth, we calculated certain dimensions of the probe to make sure the rough optical focus was also around 12 mm depth as shown in figure 6.2. For a 1 cm beam, the light will be focused from depths between 5.5 mm to 15.0 mm. The upper and lower widths of our acrylic light delivery cone/probe were 50.5 mm, and 35.21 mm and the height was 25 mm. The light probe was made of acrylic glass for guiding the laser beam and holding the fabricated annular array concave ultrasound transducer to achieve that the optical focus and ultrasound focus were at the same point on the target. This could maximize the photoacoustic signal to provide image with high contrast and resolution. This was very important in photoacoustic imaging, because if the optical focus and the ultrasound focus were not co-aligned, not only the photoacoustic signal was weak, but there could be side lobes or other artifacts in the images.



6.1.4 8-channel gage card

The 8-channel gage card (Octopus 8289, Gage Applied Systems, Inc., IL, USA) was used to acquire the data received from the eight annuli after passing through the mini-circuit amplifiers. This multichannel gage card has up to 125 MS/s sample frequency per channel. All the channels were terminated with 50 ohm for impedance matching. This multi-channel gage card allowed us to control the system from one computer, and it could capture and store data simultaneously. For synchronization purposes, the laser sent a trigger signal to the 8-channel gage card for data acquisition. In this case, the data acquisition and scan motion were synchronized. At each scan position, each annulus received A-scan data that were amplified by the mini-circuit amplifiers, then passed to the 8-channel gage card. The data received at each scan location by the 8 channels were passed to a dynamic receive beam-forming algorithm offline to construct a B-scan photoacoustic image.

6.1.5 Mini-circuit amplifiers

We used eight low noise amplifiers (ZFL-500LN+, Mini-Circuits, Brooklyn, USA) to amplify the signals received by the eight annuli. These amplifiers provided minimum 24 dB gain to the input signals. Since photoacoustic signals at different tissue depth had different strength, these low noise amplifiers could help amplify the weak signals and increase their strength. The low noise amplifier could amplify signal with frequency up to 500 MHz. For certain frequency range, by controlling the initial supply voltage to the eight low noise amplifiers, the amplification gain values could be adjusted. Figure 6.3 showed the relationship between the supply voltage and the gain value in a certain frequency range for these low noise amplifiers [88].

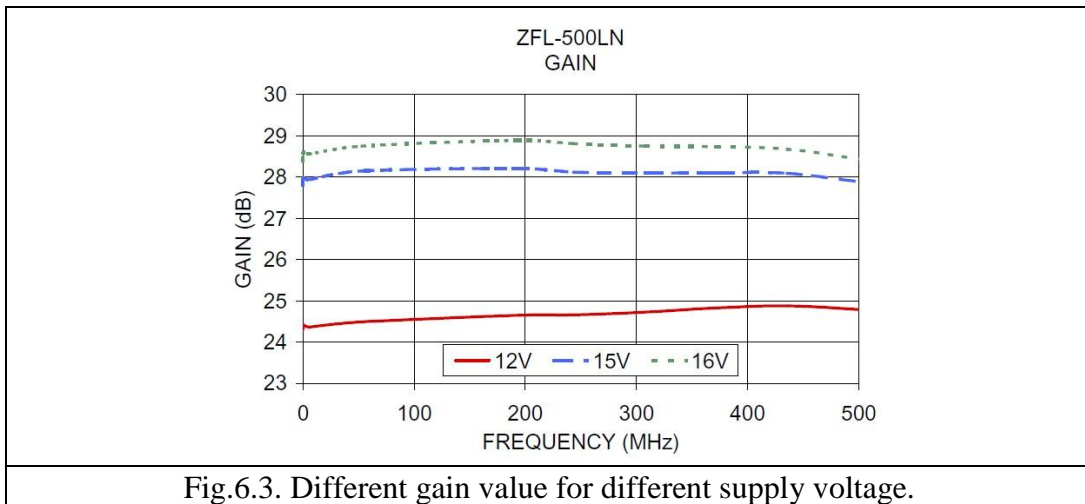


Fig.6.3. Different gain value for different supply voltage.

6.1.6 Photo of PAM experiment system

In order to demonstrate our PAM experiment system, we took a photo of our setup, as shown in figure 6.4. The eight low noise mini-circuit amplifiers were fixed in series using two thin rods and PCB holder was made to hold the PCB. A sample holder was designed to hold the hair and fiber samples. For acoustic coupling, all the samples were immersed in water for photoacoustic imaging experiment.

6.2 PAM experiment results

Using the fabricated annular array transducer, we acquired photoacoustic signals of a human hair and 7 μm carbon fiber at different depths, and applied dynamic receive beam-forming algorithms to construct the following images, as shown in figures 6.5 and 6.6. Due to transducer fabrication process flaws, the fabricated array transducer brought artifacts in the photoacoustic images.

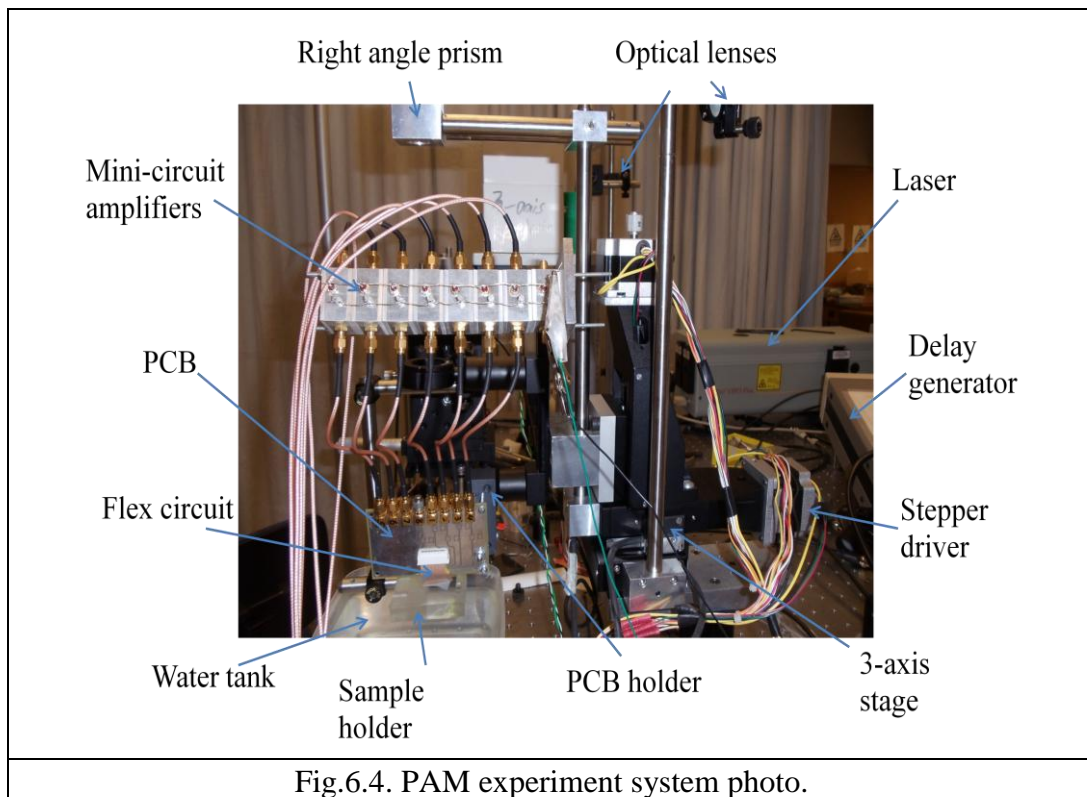


Fig.6.4. PAM experiment system photo.

6.2.1 PA image of hair by fabricated annular array ultrasound transducer

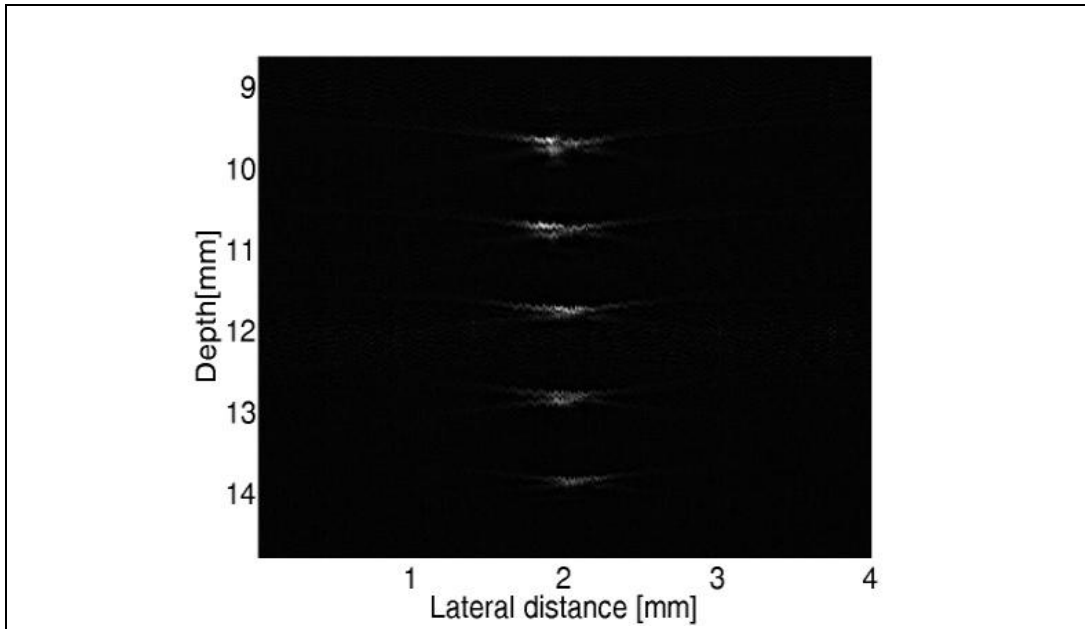


Fig.6.5. Photoacoustic image of hair at different depth with dynamic receive beam-forming algorithm for image construction.

A human hair sample was placed under the light delivery probe for photoacoustic imaging experiment. Using our PAM experiment setup, the hair was imaged at five different depth locations, as shown in figure 6.5. At each depth, the received data from each eight annulus was amplified and applied with dynamic receive beam-forming algorithms. These sets of data were summed up and processed to form the following image. We took three sets of received data from three different locations to analyze the lateral resolution values. These locations were 1 mm above the focus, at the focus, and 1 mm below the focus. We also compared the lateral resolution results of the experimental data with the simulated data, as shown in figure 6.6.

Ideally, the lateral resolution at the focus should be the smallest. From figure 6.6(a), it was noticed that the blue curve represented the received photoacoustic signal values at the focus and their amplitudes were the largest, but the lateral resolution was not the smallest. Compared with the simulated lateral resolution data at the three locations, the experimental data was not accurate. This could relate to many factors, such as transducer fabrication issues and photoacoustic experiment set up issues.

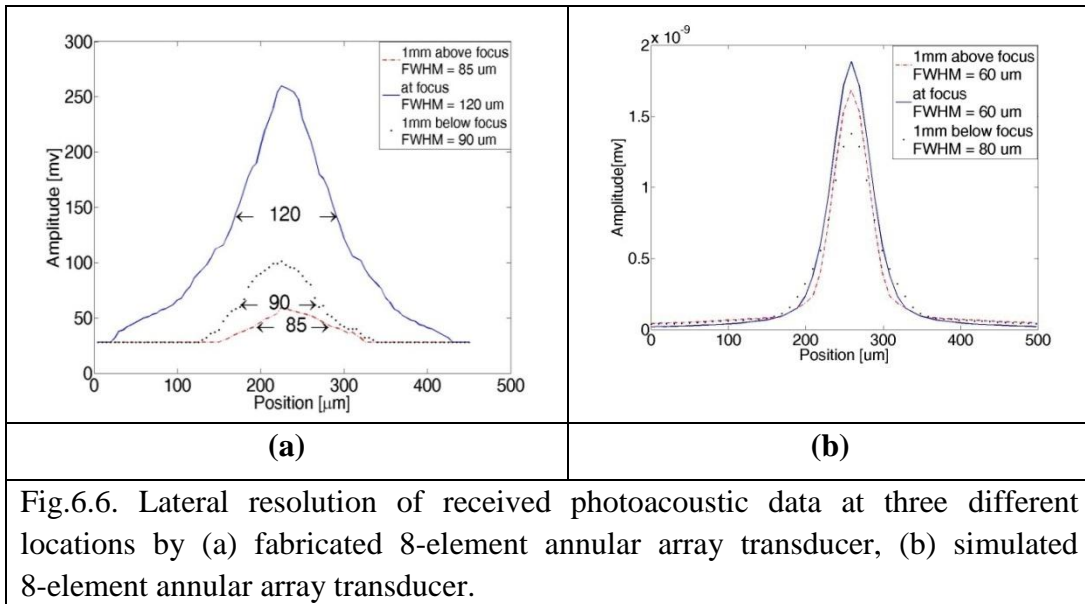


Fig.6.6. Lateral resolution of received photoacoustic data at three different locations by (a) fabricated 8-element annular array transducer, (b) simulated 8-element annular array transducer.

6.2.2 PA image of fiber by fabricated annular array ultrasound transducer

The 7 μm carbon fiber was also imaged at five different depth locations and the one placed right at the optical and ultrasound focus was chosen for resolution study. Since the carbon fiber was very thin, we needed to adjust the laser energy to prevent it from burning and breaking the fiber. Figure 6.7 shows a zoomed in version of the photoacoustic image of the carbon fiber imaged at the co-aligned focus by the fabricated annular array concave ultrasound transducer.

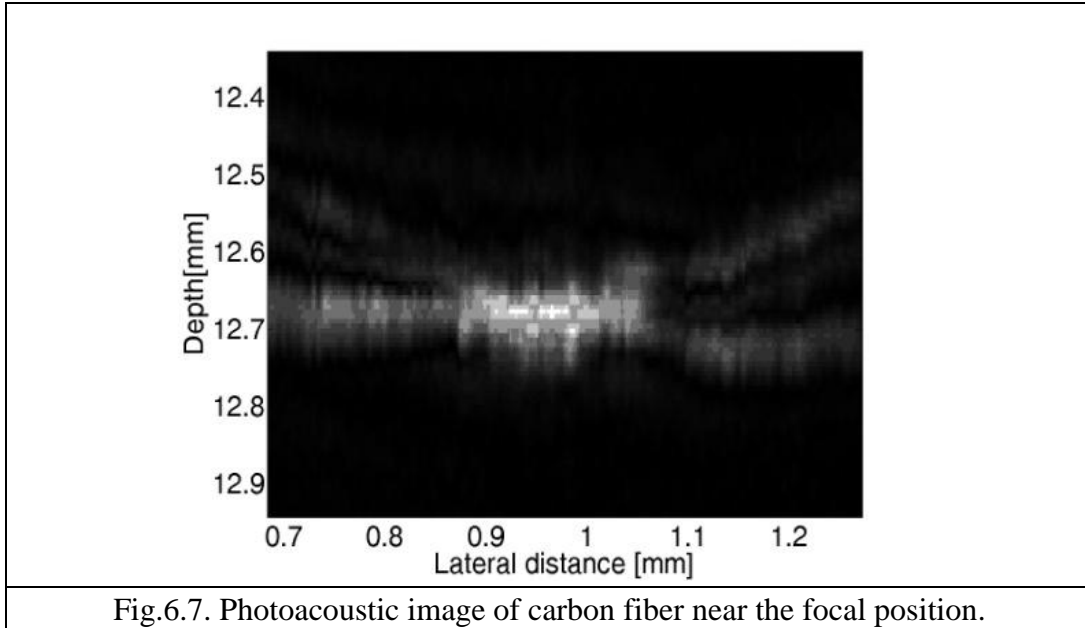


Fig.6.7. Photoacoustic image of carbon fiber near the focal position.

6.3 Limitations

6.3.1 Side lobe level issue

From both figures 68 and 70, it could be seen that the side lobe level was quite high. Ideally, we proposed to fabricate annular array transducer with large numerical aperture to reduce side lobe levels in photoacoustic images; there were other fabrication issues may cause the side lobe problem. We used the press-fit assembly to press the bonded PVDF and polyimide films. In this case, the PVDF was stretched by the stainless steel ball during the pressing process, causing strain deformation. This could affect the sensitivity of the PVDF film, thus affecting the signal detection ability by different annulus and resulting in receiving different signal strength. The received signal strength decreased from the center annulus to the outer annulus. During the press process, the film crinkling & roughness also affected the side lobe levels in the received image. When forming the concave curvature of the front transducer aperture, there was a lack of accurate centering of the ring pattern on the Teflon tube, and this led to additional side lobe level effects. The side lobe problem might also relate to the optical alignment. If the light beam was not evenly distributed on the target; during the scanning, the target might not absorb light evenly, causing unbalanced optical absorption, resulting high side lobe levels in the final photoacoustic images.

6.3.2 3-axis scanning limitation

There was a mechanical problem with one axis, so it could not make a three dimensional scan. We predicted the bearing inside was broken. After repairing it, there was still a problem regarding to no feedback from the stepper controller associated with that axis stage. This prevented tracking the scan position for each data acquisition, so it could not construct image by using the data from this scan stage. For the other two axes, the scan limit was also limited by the physical scanning range of 2.5 cm in each direction. We found that the motor drivers produced a lot of noise in the photoacoustic signals; even using a delay generator to delay the Q-switch out trigger to inhibit the motors for 20 μ s, there was still some noise left in the PA signals.

6.3.3 Real-time imaging limitation

Our group was still under development on achieving real-time photoacoustic microscopy imaging using the fabricated annular array concave ultrasound transducer. So far, all the data received by each individual annulus were stored first and processed offline to construct an image. However, realtime beamforming and display should be quite attainable. In fact, realtime operation has been achieved by several other systems in our laboratory. [37, 38, 39, 40].

6.4 Proposed solution

6.4.1 Spray-on technique

Since using the press-fit assembly to fabricate the annular array transducer caused stretching the PVDF film, the sensitivity of each annulus was reduced and the acoustic signal received by different individual annulus was uneven and reduced from the center annulus to the outer annulus. We propose a new method to fabricate such annular array concave ultrasound transducer by avoiding stretching the PVDF. This new method uses a spray-on technique, which simply sprayed on the piezoelectric material on a previously shaped-up concave backing. In this case, there was no stretching on the piezoelectric material, because it was sprayed on. We are presently pursuing this course of research in collaboration with the Industrial Materials Institute of the NRC in a group led by Jean-Pierre Monchalín. We have supplied those samples to coat with their spray-on piezo-films. We are using fused silica ground into a concave shape using a rotating brass ball with diamond paste. The concave backing was first coated with a thin layer of Ni metal as the back electrode layer and was sprayed on the piezoelectric material. Another

Ni layer was coated on top of the piezoelectric material layer as the top electrode. Before coating the top Ni metal layer, the piezoelectric material was subjected to a process called corona poling to enhance its piezoelectric properties by aligning the molecules in a certain ideal orientation. Once we receive these samples, two wires will be used to bond to the two Ni metal layers with conductive epoxy to engage electrical conductivity with the two metal layers. We aim to first test a high-NA high-frequency single element transducer (these are difficult enough to fabricate) then pursue patterning of the rings to form an annular array.

Ch 7: Discussion, Conclusions, and Future Work

7.1 Discussion

The objective of this thesis was to develop a dark-field confocal photoacoustic microscopy system based on custom-fabricated high-frequency and high-numerical aperture annular array transducers. The intention of fabricating these transducers was to maintain the high focusing quality and spatial resolution provided by high-frequency high-numerical aperture single-element transducers while attempting to extend the depth of field by using dynamic receive focusing. The main contributions to the literature include simulations, fabrication (although our fabrication method was based on a technique published by another group) and photoacoustic experiments. To our knowledge our work represents the first implementation of high-frequency, high-numerical aperture annular array transducers for photoacoustic imaging.

While previous groups have used acoustic field simulations to optimize annular array performance for pulse-echo ultrasound imaging, our simulations are to our knowledge the first documented systematic study of how annular array parameters affect image quality for photoacoustic imaging. Field II simulations revealed that planar annular arrays exhibited undesirably high sidelobe artifacts when attempting dynamic focusing with the large numerical apertures (~ 0.45) of previous PAM systems. Forming annuli into a concave shape enabled high-NA focusing with a mixture of geometric focusing and electronic (dynamic-receive) focusing. However, even though the dynamic range could be extended considerably and high-NA focusing well away from the geometric focus was successfully implemented, there were consequences to doing so. Sidelobe levels, a result of focusing artifacts rapidly grew in regions away from the geometric focus so that even though the focusing was improved, the quality of the focusing was not maintained beyond a couple of mm on either side of the focus. There are still potential image quality advantages over single-element transducers, but the image-quality advantages are also coupled with artifacts. It is possible that some of these artifacts could in part be minimized using higher channel counts and smaller kerfs, however, some of the artifacts stem from the breakdown of assumptions needed by the Fresnel approximation which are required for dynamic electronic focusing to properly work. Additionally, we did not consider higher channel counts because we were limited by available hardware to an 8-channel data acquisition system.

Fabrication of our high-frequency annular array transducers followed closely with previous work by Ketterling et al, but specific details differed from their work. In brief, we used a press-fit technique to stretch a piezopolymer-film into a concave shape with back-electrodes formed from patterned metalized polyimide. Epoxy was used as a backing material which had an acoustic impedance that closely matched the polyimide and piezopolymer.

The ultrasound pulse echo testing indicated that all the individual annuluses had wide bandwidth responses with center frequency around 40 MHz. This is an accomplishment that few groups have been able to reproduce.

The fabrication process turned out to be fairly challenging with many critical steps. For the photolithography process, a layer of photoresist was first spin-coated on the copper layer of the polyimide. The spread and spin parameters were set to ensure certain thickness of the coated photoresist. We used special fab-compatible double-sided tape to secure the polyimide on a silicon carrier wafer for contact lithography. Because the polyimide was effectively suspended on the tape above the wafer, contact lithography was not ideal due to larger than desired distances between the mask and the polyimide. After the lithography step, the polyimide film was developed, etched and cleaned to successfully form the mask pattern on the copper side of the polyimide film. The etching step was very critical because it could break the electrical leads by over etching it or cause electrical shortage by under etching it. In the future, outsourcing the flex-circuit fabrication is recommended.

A single drop of epoxy was used to bond the piezopolymer to the polyimide. If this bonding layer was too thick, it resulted in a lower-than desirable frequency response. If the bonding layer was not adequate, the piezopolymer could peel away from the polyimide and result in effective “dead” zones. Rolling the polyimide-epoxy-PVDF sandwich structure with a rolling tool turned out to help achieve a more reproducible thin-bonding layer and was a modification from the work of previous groups. A small bead of conductive epoxy was used to bond and electrically connect a ground-wire to the top metalized surface of the piezopolymer. Many failed attempts of transducer fabrication were due to lack of connectivity from this step and were thought to be due to details of using the conductive epoxy. Bake-temperatures and fresh conductive epoxy were critical to the success of these procedures. Soldering could not be used because it would denature the piezopolymer.

A more fundamental issue that ultimately limited the effectiveness of our proposed annular array was a problem of stretching of the piezopolymer during the press-fit procedure. Stretching of the piezopolymer resulted in reduced sensitivity and this was most severe for outer annuli. This resulted in an effective apodization across the aperture surface and effectively limited the numerical aperture of the transducer, which was one of the key aspects we hoped to maintain in our design. Aside from this problem, we believe that other non-idealities resulted in point-spread functions significantly less focused than simulated predictions. Such non-idealities include undesirable crimping of the piezopolymer, lack of perfect centering of the annuli to the geometric center of the concave surface, among other issues. The centering problem could lead to the acoustic focusing axis effectively being angled relative to the geometric focusing axis. This problem alone should not be too problematic except that the dark-field optical focusing is designed to be concentric with the acoustic geometric focal axis. Crimping of the piezopolymer is problematic because the effective directivity becomes unpredictable and the transducer could pick up on off-axis signals that would effectively have lower sensitivity in an ideal annular array transducer. Jitter problems observed in our experimental data can be solved with future clock-synchronization between the laser and the data acquisition system.

To solve the problems of piezopolymer stretching, we propose the use of spray-on piezo-films pioneered by C.-K. Jen, M. Kobayashi, K.-T. Wu and others. We are presently working with a group at the Industrial Materials Research Institute, an Institute of the National Research Council of Canada to fabricate such transducers. The advantage of this technology is that a sol-gel-based piezo-spray can be sprayed onto a concave transducer surface, cured and poled so that there are no stretching issues as we experienced with the piezopolymer press-fit technique. One potential disadvantage is that fairly high temperatures are needed to make a good transducer. These temperatures can be lower than 400 °C, meaning potential CMOS compatibility (to be explored), but these temperatures are higher than typically compatible with polymers or plastics. Even if their melting points are above 400 °C, these materials can undergo plastic deformation, optical opacity and can produce toxic gases due to these temperatures. This means that we cannot use epoxies or plastics as acoustic backing materials (desirable because of their low acoustic impedance), and must instead use alternate materials with higher melting points such as metals or glasses. Unfortunately these materials have relatively higher acoustic impedances and may result in the piezo-layer acting as half-wavelength rather than quarter-wavelength operation. This is because a backing layer with a high acoustic impedance can result in reflections without 180° phase inversion necessary for quarter-wavelength constructive interference. This means that an

even thinner piezolayer will be needed to attain the same high-frequency wavelength that would be possible if a low-impedance backing were used. Despite this limitation, the spray-on technique does offer some control over film thickness and has been used to produce transducers with frequencies as high as 50MHz. The spray-on technology has principally been used for non-destructive testing applications and has had limited applications in the biomedical regime.

Future work should aim to improve upon the limitations of our transducers, as mentioned. In parallel, our piezo-polymer annular array could be used for phantom and in vivo imaging; however, we found this challenging without transducer optimization. It should be mentioned that at the last IEEE International Ultrasonics Symposium in October 2011, Aristizabal et al. [89] presented a paper on a 5-ring annular array high-frequency transducer for photoacoustic imaging. This paper was presented after our SPIE conference paper. While both our work and theirs demonstrated near 40-MHz piezopolymer transducers (a sufficiently challenging task) there are also some differences. We used a higher-NA transducer with 8 rings instead of 5 and our aperture was much larger than theirs. They pursued some imaging of mouse embryos but seemed to only image within a narrow region of the focal plane of their transducer and did not demonstrate the improved depth-of-field of the transducer using point-spread functions. They combined ultrasound and photoacoustic imaging, but their photoacoustic image quality (in particular lateral resolution) was still far inferior to images presented by Maslov et al. and Zhang et al.

The field of photoacoustics is rapidly evolving and there will no doubt be future improvements to photoacoustic microscopy in the near future. While the work in this M.Sc. thesis did not fully fulfill our original goals of simultaneously improved depth-of-field and maintaining high-NA-enabled lateral focusing due to un-anticipated problems with transducer non-idealities, we did make progress and better understand some of the issues and trade-offs in achieving this challenging goal. In particular, we did successfully fabricate transducers with 40 MHz center frequency and broad bandwidth (a challenging task), we did fabricate a working annular array transducer with high frequency and high numerical aperture (with some non-ideal aspects) and we did demonstrate improved depth-of-field photoacoustic microscopy with such a transducer for the first time.

Bibliography

- [1] Huihong Lu, Peng Shao, Janaka Ranasinghesagara, Tim DeWolf, Tyler Harrison, William Gibson, and Roger J. Zemp, "Improved depth-of-field photoacoustic microscopy with a custom high-frequency annular array transducer", *Proc. of SPIE*, Vol. 7899, 78993R-1, 2011.
- [2] Srivalleesha Mallidi, Geoffrey P. Luke and Stanislav Emelianov, "Photoacoustic imaging in cancer detection, diagnosis, and treatment guidance", *Trends in Biotechnology*, Vol. 29, No. 5, May 2011.
- [3] http://en.wikipedia.org/wiki/Photoacoustic_imaging_in_biomedicine
- [4] <http://omlc.ogi.edu/spectra/hemoglobin/>
- [5] Richard S. C. Cobbold, "Foundations of Biomedical Ultrasound", *Oxford University Press, Inc.* printed in USA, ISBN-13 978-0-19-516831-0, 2007.
- [6] Roger Zemp, "Photoacoustic Imaging in Biomedicine"
- [7] A. L. McKenzie, "Physics of thermal processes in laser-tissue interaction", *Phys. Med. Biol.*, Vol. 35, No 9, 1175-1209, 1990.
- [8] Vitalii Eduardovich Gusev, Aleksandr Alekseevich Karabutov, "Laser Optoacoustics", *American Institute of Physics*, New York, 1993.
- [9] Lihong V. Wang and Hsin-i Wu, "Biomedical Optics Principles and Imaging", *published by Wiley-Interscience, a John Wiley & Sons, Inc., printed in USA*, ISBN: 978-0-471-74304-0, Pg 287, 2007.
- [10] Philip McCord Morse and Herman Feshbach, "Methods of theoretical physics", *McGraw-Hill*, New York, 1953.
- [11] Hao F Zhang, Konstantin Maslov, George Stoica & Lihong V. Wang, "Functional photoacoustic microscopy for high-resolution and noninvasive *in vivo* imaging", *Nature Biotechnology*, Vol. 24, No. 7, July 2006.
- [12] Liang Song, Konstantin Maslov, Rachel Bitton, K. Kirk Shung, and Lihong V. Wang, "Fast 3-D dark-field reflection-mode photoacoustic microscopy *in vivo* with a 30-MHz ultrasound linear array", *Journal of Biomedical Optics*, Vol. 13, No. 5, September/October 2008.

- [13] Yiwen Wang, Xueyi Xie, Xueding Wang, Geng Ku, Kelly L. Gill, D. Patrick O’Neal, George Stoica, and Lihong V. Wang, “Photoacoustic tomography of a nanoshell contrast agent in the In vivo rat brain”, *Nano Letters*, Vol. 4, pp. 1689–1692, 2004.
- [14] Minghua Xu and Lihong V. Wang, “Universal back-projection algorithm for photoacoustic computed tomography”, *Physical Review E*, vol. 71, pp. 016706-1–016706-7, 2005.
- [15] Andreas Buehler, Amir Rosenthal, Thomas Jetzfellner, Alexander Dima, Daniel Razansky, and Vasilis Ntziachristos, "Model-based photoacoustic inversions with incomplete projection data", *Medical Physics*, Vol. 38, No. 3, 1694-1704, 2011.
- [16] Geng Ku and Lihong V. Wang, “Deeply penetrating photoacoustic tomography in biological tissues enhanced with an optical contrast agent”, *Optics Letters*, Vol. 30, No. 5, March 1, 2005.
- [17] Xueding Wang, Yongjiang Pang, and Geng Ku, "Three-dimensional laser-induced photoacoustic tomography of mouse brain with the skin and skull intact", *Optics Letters*, Vol. 28, No. 19, 1739-1741, Oct 1, 2003.
- [18] Xueding Wang, Yongjiang Pang, Geng Ku, Xueyi Xie, George Stoica and Lihong V. Wang, "Noninvasive laser-induced photoacoustic tomography for structural and functional *in vivo* imaging of the brain", *Nature Biotechnology*, Vol. 21, 803-806, 2003.
- [19] Kruger RA, Kiser WL Jr, Reinecke DR, Kruger GA, "Thermoacoustic computer tomography using a conventional linear transducer array", *Med Phys.*, Vol. 30, No. 5, 856-860, May 2003.
- [20] Lihong V. Wang, “Multiscale photoacoustic microscopy and computed tomography,” *Nature Photonics*, Vol. 3 September, 2009.
- [21] Ian Collions and Paul Workman, "New approaches to molecular cancer therapeutics", *Nature Chemical Biology*, Vol. 2, 689-700, 2006.
- [22] Kruger RA, Kiser WL, Reinecke DR, Kruger GA, Miller KD, "Thermoacoustic molecular imaging of small animals", *Molecular Imaging*, Vol. 2, No. 2, 113-123, 2003.

- [23] Xueding Wang, Geng Ku, Malgorzata A. Wegiel, Darryl J. Bornhop, George Stoica, and Lihong V. Wang, "Noninvasive photoacoustic angiography of animal brains in vivo with near-infrared light and an optical contrast agent", *Optics Letters*, Vol. 29, Issue 7, 730-732, 2004.
- [24] Mohammad Eghtedari, John A. Copland, Vsevolod L. Popov, Nicholas Kotov, Massoud Motamedi, and Alexander A. Oraevsky, "Bioconjugated gold nanoparticles as a contrast agent for photoacoustic detection of small tumors", *SPIE*, Vol. 4960, 76-85, 2003.
- [25] Yiwen Wang, Xueyi Xie, Xueding Wang, Geng Ku, Kelly L. Gill, D. Patrick O'Neal, George Stoica and Lihong V. Wang, "Photoacoustic Tomography of a Nanoshell Contrast Agent in the *in Vivo* Rat Brain", *Nano Letters*, Vol. 4, No. 9, 1689-1692, 2004.
- [26] L. Li, **R.J. Zemp**, (equal contribution) G. Lungu, G. Stoica, L.V. Wang, "Photoacoustic imaging of gene expression", *J. Biomed. Optics*, Vol. 12, No. 2, pp. 020504, March/April 2007.
- [27] L. Li, H. Zhang, **R.J. Zemp**, K. Maslov, L.V. Wang, "Simultaneous imaging of a lacZ-marked tumor and microvasculature morphology in vivo by dual-wavelength photoacoustic microscopy", *Journal of Innovative Optical Health Sciences*, Vol. 1, No. 2, 207–215, 2008.
- [28] **R.J. Zemp, L.Li**, L.V. Wang, "Photoacoustic Imaging of Gene Expression" in *Photoacoustic Imaging and Spectroscopy*, Edited by Lihong V. Wang, Taylor & Francis Group/CRC press, 2009.
- [29] **R.J. Zemp**, M.L. Li, R. Bitton, K.K. Shung, G. Stoica, and L.V. Wang, "Photoacoustic Imaging of the Microvasculature with a High-Frequency Ultrasound Array Transducer", *J. Biomed. Optics*, Vol. 12(1), pp. 010501, Jan./Feb. 2007.
- [30] R. Bitton, **R. J. Zemp**, J. Yen, L. V. Wang, and K. Kirk Shung, "A 3D high frequency array based 16 channel photoacoustic microscopy system for in-vivo micro-vascular imaging", *IEEE Transactions on Medical Imaging*, Vol. 28, No. 8, pp. 1190-1197, 2009.

- [31] Roger J. Zemp, Liang Song, Rachel Bitton, K. Kirk Shung, and Lihong V. Wang, "Realtime photoacoustic microscopy *in vivo* with a 30-MHz ultrasound array transducer", *OPTICS EXPRESS*, Vol. 16, No. 11, May 26 2008.
- [32] **R.J. Zemp**, L. Song, R. Bitton, K.K. Shung, L.V. Wang, "Realtime photoacoustic imaging of cardiac and respiratory dynamics in mice", *Optics Express*, Vol. 16, No. 22, 2008.
- [33] Hao F. Zhang, Konstantin Maslov, Geoge Stoica, and Lihong V. Wang, "Imaging acute thermal burns by photoacoustic microscopy", *Journal of Biomedical Optics*, Vol. 11, No. 5, September/October 2006.
- [34] Konstantin Maslov, Hao F. Zhang, Song Hu, and Lihong V. Wang, "Optical-resolution photoacoustic microscopy for *in vivo* imaging of single capillaries", *OPTICS LETTERS*, Vol. 33, No. 9, May 1 2008.
- [35] Edward Z. Zhang, Jan Laufer, Boris Povazay, Aneesh Alex, Bernd Hofer, Wolfgang Drexler and Paul Beard, "Multimodal simultaneous photoacoustic tomography, optical resolution microscopy, and OCT system", *SPIE*, Vol. 7564, 2010.
- [36] Mengyang Liu and Takashi Buma, "Wavelength agile photoacoustic microscopy with a pulsed supercontinuum source", *IEEE*, Vol. 978, 382-385, 2010.
- [37] P. Hajireza, W. Shi, P. Shao, A. Forbrich, **R.J. Zemp**, "Real-time Handheld Optical--Resolution Photoacoustic Microscopy", *Optics Express*, Vol. 19, No. 21, Oct 10 2011.
- [38] P. Hajireza, W. Shi, P. Shao, S. Kerr, **R.J. Zemp**, "Label-Free *in vivo* Fiber-Based Optical Resolution Photoacoustic Microscopy", *Optics Letters*, Vol. 36, No. 20, Oct 15 2011.
- [39] Wei Shi, Shaun Kerr, Ilya Utkin, Janaka Ranasinghesagara, Lei Pan, Yogesh Godwal, Roger J. Zemp, Robert Fedosejjevs, "Optical resolution photoacoustic microscopy using novel high-repetition-rate passively Q-switched microchip and fiber lasers", *Journal of Biomedical Optics*, Vol. 15, No. 5, pp. 056017, 2010.
- [40] W. Shi, P. Hajieza, P. Shao, A. Forbrich, **R.J. Zemp**, "In vivo near-real-time volumetric optical-resolution photoacoustic microscopy using a

high-repetition-rate nanosecond fiber-laser”, *Optics Express*, Vol. 19, Issue 18, pp. 17143-17150, Aug 29 2011.

[41] Y. Jiang, A. Forbrich, **R.J. Zemp**, “Blood Oxygen Flux Estimation with a Combined Photoacoustic and High-Frequency Ultrasound Microscopy System: a Phantom Study”, *Journal of Biomedical Optics*, 2010.

[42] Yan Jiang, Tyler Harrison, Alex Forbrich, **R.J. Zemp**, “Oxygen Consumption Estimation using Combined Photoacoustic and Color Doppler Ultrasound Imaging”, *World Molecular Imaging Congress*, San Diego, CA. 2011.

[43] Janaka C. Ranasinghesagara, Yan Jiang, Xuhui Chen, Kory Mathewson, and Roger J. Zemp, "Photoacoustic technique for assessing optical scattering properties of turbid media", *Journal of Biomedical Optics*, Vol. 14, No. 4, July/August 2009.

[44] <http://www.visualsonics.com>

[45] <http://www.olympus-ims.com/data/File/panametrics/UT-technotes.en.pdf>

[46] http://www.proz.com/kudoz/English/medical%3A_instruments/886363-spatial_peak_temporal_average_intensity_720_mw_cm2.html

[47] <http://www.sprawls.org/ppmi2/USPRO/#Unfocused%20Transducers>

[48] Atam P. Dhawan, “Medical Imaging Modalities: Ultrasound Imaging”, Institute of Electrical and Electronics Engineers, 2011.

[49] Yongli Huang, A. Sanli Ergun, Edward Haggstrom, Mohammed H. Badi, and B. T.Khuri-Yakub, “Fabricating Capacitive Micromachined Ultrasonic Transducers With Wafer-Bonding Technology”, *Journal of Microelectromechanical Systems*, Vol. 12, No. 2, April 2003.

[50] Arne Ronnekleiv, “CMUT Array Modeling Through Free Acoustic CMUT Modes and Analysis of the Fluid CMUT Interface Through Fourier Transform Methods”, *IEEE Transactions on Ultrasonics, Ferroelectrics, and Frequency Control*, Vol. 52, No. 12, December 2005.

[51] L.Medina, E. Moreno, G. Gonzalez, and L. Leija, “Circular ultrasonic transducer characterization: theoretical and experimental results”, *Rev. Mex. Fis*, Vol. 49, No. 6, December 2003.

[52] <http://www.us-tip.com/serv1.php>

- [53] L. Satyanarayan, Krishnan Balasubramaniam, C.V.Krishnamurthy, “Phased array ultrasound to image internal corrosion in pipes”, Department of Mechanical Engineering, IIT Madras, Chennai-600 036, India.
- [54] Xiaochen Xu, Lequan Zhang, Lei Sun, Jesse T. Yen, Jonathan M. Cannata, K. Kirk Shung, “High-frequency Duplex Ultrasound Imaging System for Biomedical Applications Using 30 MHz Linear Arrays”, *IEEE Ultrasonics Symposium*, 2007.
- [55] Aaron Fenster, Donal B Downey and H Neale Cardinal, “Three-dimensional ultrasound imaging”, *Physics in Medicine and biology*, 46 R67-R99, November. 6, 2000.
- [56]http://www-kyg.stanford.edu/khuriyakub/opencms/en/research/ultrasonic/3D_Imaging/index.html
- [57] Y. Ona, M. Kobayashi, d. Levesque, L. Song, M. sivagnanasundaram, and C. –K. Jen, “High Frequency (>30 MHz) Flexible Broadband Transducers”, *IEEE ultrasonics symposium*, pp. 92-95, 2007.
- [58] Marc Lukacs, Jianhua Yin, Guofeng Pang, Pichard Garcia, Emmanuel Cherin, Ross Williams and F. Stuart Foster, Jim Mehi, “Performance and Characterization of High Frequency Linear Arrays”, *IEEE ultrasonics symposium*, pp. 105-108, 2005.
- [59] J. M. Cannata, J. A. Williams and K. K. Shung, “A Kerfless 30 MHz Linear Ultrasonic Array”, *IEEE ultrasonics symposium*, pp. 109-112, 2005.
- [60] R. J. Kline-Schoder, D. B. Kynor, M. D. Jaeger, “Fabrication of High Frequency Ultrasonic Transducer Arrays Using Physical Vapor Deposition”, *IEEE*, 1999.
- [61] Chih-Kuang Yeh, Chao-Hung Chunh, Jia-Jiun Chen and Jia-Jin Jason Chen, “High-frequency ultrasonic imaging system: a preliminary small animals study”, *International Journal of Electrical Engineering*, Vol. 15, No. 3, PP. 195-202, 2008.
- [62] Kevin C. Graham, Lauren A. Wirtzfeld, Lisa T. Mackenzie, “Three-dimensional high-frequency ultrasound imaging for longitudinal evaluation of liver metastases in preclinical models”, *Cancer Research*, Vol. 65, No. 12, June 15, 2005.

- [63] Ioannis M Aslanides, Peter E Libre, Ronald H Silverman, Dan Z Reinstein, Douglas R Lazzaro, Mark J Rondeau, Gregory K Harmon, DJackson Coleman, "High frequency ultrasound imaging in papillary block glaucoma", *British Journal of Ophthalmology*, Vol. 79, Pg. 972-976, 1995.
- [64] John Sun, Liis Lindvere, Martijn e. van Raaij, Adrienne Dorr, Bojana Stefanovic, and f. Stuart Foster, "In Vivo Imaging of Cerebral Hemodynamics Using High-Frequency Micro-Ultrasound", *Cold Spring Harb Protoc*, 2011.
- [65] Dietz, "United States Patent on Annular Array Ultrasonic Transducers", August 27, 1985.
- [66] Emanuel J. Gottlieb, Jonathan M. Cannata, Chang Hong Hu, K. Kirk Shung, "High Frequency Copolymer Annular Array Ultrasound Transducer Fabrication Technology", *IEEE ultrasonics symposium*, pp. 121-124, 2005.
- [67] Kevin A. Snook, Timothy A. Ritter, Thomas R. Shrou, K. Kirk Shung, "Design of a High Frequency Annular Array for Medical Ultrasound", *IEEE ultrasonics symposium*, pp. 1161-1164, 2001.
- [68] Jeremy A. Brown, Christine E. M. Demore, and Geoffrey r. Lockwood, "Design and Fabrication of Annular Arrays for High-Frequency Ultrasound", *IEEE Transactions on Ultrasonics, Ferroelectrics, and Frequency Control*, Vol. 51, No. 8, August 2004.
- [69] Kevin A. Snook, Chang-Hong Hu, Thomas R. Shrou, and K. Kirk Shung, "High-Frequency Ultrasound Annular-Array Imaging. Part I: Array Design and Fabrication", *IEEE Transactions on Ultrasonics, Ferroelectrics, and Frequency Control*, Vol. 53, No. 2, February 2006.
- [70] Jeffrey A. Ketterling, Orlando Aristizabal, Daniel H. Turnbull, and Frederic L. Lizzi, "Design and Fabrication of a 40-MHz Annular Array Transducer," *IEEE Transactions on Ultrasonics, Ferroelectrics, and Frequency Control*, Vol. 52, No. 4, April 2005.
- [71] Peter R. Stephanishen, "Transient Radiation from Pistons in an Infinite Planar Baffle", *Journal of the Acoustical Society of America*, Feb 24 1970.

- [72] Peter R. Stepanishen, "Pulsed transmit/receive response of ultrasonic piezoelectric transducers", *Acoustical Society of America*, Vol. 6, 1815-1827, June 1981.
- [73] J.A. Jensen, "Field: A Program for Simulating Ultrasound Systems", Paper presented at the 10th Nordic-Baltic Conference on Biomedical Imaging, *Medical & Biological Engineering & Computing*, pp. 351-353, Volume 34, Supplement 1, Part 1, 1996.
- [74] J.A. Jensen and N. B. Svendsen: "Calculation of pressure fields from arbitrarily shaped, apodized, and excited ultrasound transducers", *IEEE Trans. Ultrason., Ferroelec., Freq. Contr.*, 39, pp. 262-267, 1992.
- [75] <http://server.oersted.dtu.dk/personal/jaj/field/?background.html>
- [76] Jorgen Arendt Jensen, "User's guide for the Field II program", August 17, 2001.
- [77] Suhyun Park, Salavat R. Aglyamov, Stanislav Y. Emelianov, "Beamforming for photoacoustic imaging using linear array transducer," *IEEE Ultrasonics Symposium Proc*, pp. 856-859, 2007.
- [78] Aruna Kroetch, "NanoFab's Quick Overview of L-EDIT", June 27, 2005.
- [79] http://www.nanofab.ualberta.ca/downloadable_files/processes/OverviewofMaskMaking.pdf
- [80] Stephanie Bozic and Jolene Chorzempa, "Solitec Spinner", *NanoFab in University of Alberta*, March 23, 2009.
- [81] Tyler Lucas, "EE 457: Multiplayer Devices", Mach 1, 2010.
- [82] http://www.nanofab.ualberta.ca/site/?page_id=467
- [83] Stephanie Bozic and Jolene Chorzempa, "Hands-on Demonstration of Basic Processing", *NanoFab in University of Alberta*, May 2009.
- [84] Jolene Chorzempa and Stephanie Bozic, "HPR 504 Photo Resist", *NanoFab in University of Alberta*, April 11, 2011.
- [85] Stephanie Bozic and Jolene Chorzempa, "ABM Mask Aligners", *NanoFab in University of Alberta*, March 26, 2009.

[86] http://www.nanofab.ualberta.ca/site/?page_id=365

[87] H. F. Zhang, K. Maslov, M. L. Li, G. Stoica, and L. H. V. Wang, "In vivo volumetric imaging of subcutaneous microvasculature by photoacoustic microscopy", *Optics Express*, Vol. 14, pp. 9317-9323, Oct 2 2006.

[88] <http://www.minicircuits.com/pdfs/ZFL-500LN.pdf>

[89] Orlando Aristizábal, Jonathan Mamou, Erwan Filoux, Jeffrey A. Ketterling, Daniel H. Turnbull, Parag V. Chitnis, " Simultaneous photoacoustic and high-frequency ultrasound in vivo imaging of the mouse embryonic vasculature", *IEEE International Ultrasonics Symposium*, October 2011.

Appendices

Appendix 1: Simulation of photoacoustic image of five point-absorbers using a 40 MHz single element concave ultrasound transducer with 0.5 and 0.33 numerical apertures

```
% Generate the transducer apertures for send and receive
f0=40e6;           % Transducer center frequency [Hz]
fs=500e6;         % Sampling frequency [Hz]
cw=1540;          % Speed of sound in water[m/s]
lambda=cw/f0;     % Wavelength [m]
Efocus=12/1000;  % Transmit Focal radius of aperture [m]
% Receive Focal radius of aperture [m]
R=6/1000;         % Radius of active aperture of transducer [m] 0.5 NA
% R=4/1000;       % Radius of active aperture of transducer [m] 0.33 NA
ele_size=1/1000;% Size of mathematical elements [m]
% f-number
f = Efocus/(2*R);
% NA
NA = 1/(2*f);
% Initialize field II program
field_init;
% Set the sampling frequency
set_sampling(fs);
% Generate aperture for emission
emit_aperture = xdc_concave(R, Efocus, ele_size);
% Set the impulse response and excitation of the emit aperture
impulse_response=sin(2*pi*f0*(0:1/fs:2/f0));
impulse_response=impulse_response.*hanning(max(size(impulse_respon
se)))';
xdc_impulse (emit_aperture, impulse_response);
excitation=sin(2*pi*f0*(0:1/fs:2/f0));
xdc_excitation (emit_aperture, excitation);
% Generate aperture for reception
receive_aperture = xdc_concave(R, Efocus, ele_size);
xdc_impulse (receive_aperture, impulse_response);
% Create the point scatterers' positions
dz=1/1000;        % Distance between points [m]
```

```

z_start=9/1000;      % Start of point [m]
NP=5;                % Number of points
% Initializing positions
positions = [zeros(1,NP); zeros(1,NP); (1:NP)*dz+z_start]';
amplitude=ones(NP,1);
amplitude=amplitude*10e9;
% Imaging range
no_lines=300;        % Number of A-scan lines in image
sector=2/1000;       % Size of image sector [m]
d_x=sector/no_lines; % Increment for image
s_x= -sector/2;      % Start point of image sector
delta_x=d_x*ones(1,NP);
delta=[delta_x; zeros(1,NP); zeros(1,NP)]';
positions=positions+[s_x.*ones(1,NP);zeros(1,NP);zeros(1,NP)]';

for j=1:no_lines
j
% Calculate the received response
positions=positions+delta;
[v, t1]=calc_scatter(emit_aperture, receive_aperture, positions,
amplitude);
% Store the result
image_data(1:max(size(v)),j)=v;
times(j) = t1;
end
%Free space for apertures
xdc_free (emit_aperture)
xdc_free (receive_aperture)

for j=1:no_lines %i is the no_lines
a(:,j) = squeeze(image_data(:,j,:));
b(:,j) = sum(a,2);
end
image=abs(hilbert(b));
%Plotting with proper scales
x_scale = (sector*1000)*[1:no_lines]./no_lines; % [mm]
y_scale = (t1+[1:size(image,1)]/fs)*(cw/2)*1000; % [mm]
figure;imagesc(x_scale, y_scale, log(image));

```

```
set(gca, 'FontSize', 34);  
xlabel('Lateral distance [mm]', 'FontSize', 34);  
ylabel('Depth[mm]', 'FontSize', 34);  
colormap gray;  
brighten(-0.8);
```

Appendix 2: Simulation of annular array concave ultrasound transducer

```
% Initialize field II program
field_init;
focus=12/1000;           % Geometric focus point [m]
ele_size=0.1/1000;       % Size of mathematical elements [m]
f0=40e6;                 % Transducer center frequency [Hz]
fs=500e6;               % Sampling frequency [Hz]
cw=1540;                % Speed of sound in water[m/s]
R1=1.9488/1000;         % Radius of active aperture of transducer1 [m]
R2=2.82761434428389/1000;% Radius of active aperture of transducer2 [m]
R3=3.51692297169796/1000;% Radius of active aperture of transducer3 [m]
R4=4.10852202418295/1000;% Radius of active aperture of transducer4 [m]
R5=4.63783128930247/1000;% Radius of active aperture of transducer5 [m]
R6=5.12297440613297/1000;% Radius of active aperture of transducer6 [m]
R7=5.57470026881446/1000;% Radius of active aperture of transducer7 [m]
R8=6/1000;             % Radius of active aperture of transducer8 [m]
kerf=0.1/1000;         % Separation between each annuli [m]
% Set the sampling frequency
set_sampling(fs);
% Define transducer
Th = xdc_concave(R8, Rfocus, ele_size);
% Do it for the rectangular elements
colormap(cool(128));
data = xdc_get(Th, 'rect');
[N,M]=size(data);
apo_rx = zeros(8,M);
data1 = zeros(N+1,M);
data1(1:N,1:M) = data;
% Do the actual display
for i=1:M
x=[data(11,i), data(20,i); data(14,i), data(17,i)];% [mm]
y=[data(12,i), data(21,i); data(15,i), data(18,i)];% [mm]
z=[data(13,i), data(22,i); data(16,i), data(19,i)];% [mm]
r = sqrt(x.^2+y.^2);
rmin = min(min(r));
rmax = max(max(r));
hit = 0;
```

```

if (rmax<R8 && rmin>(R7+kerf))
hit = 1;
c=data(5,i)*ones(2,2);
data1(N+1,i) = 8;
apo_rx(8,i) = data(5,i);
apo8 = apo_rx(8,:);
end
if (rmax<R7 && rmin>(R6+kerf))
hit = 1;
c=data(5,i)*ones(2,2);
data1(N+1,i) = 7;
apo_rx(7,i) = data(5,i);
apo7 = apo_rx(7,:);
end
if (rmax<R6 && rmin>(R5+kerf))
hit = 1;
c=data(5,i)*ones(2,2);
data1(N+1,i) = 6;
apo_rx(6,i) = data(5,i);
apo6 = apo_rx(6,:);
end
if (rmax<R5 && rmin>(R4+kerf))
hit = 1;
c=data(5,i)*ones(2,2);
data1(N+1,i) = 5;
apo_rx(5,i) = data(5,i);
apo5 = apo_rx(5,:);
end
if (rmax<R4 && rmin>(R3+kerf))
hit = 1;
c=data(5,i)*ones(2,2);
data1(N+1,i) = 4;
apo_rx(4,i) = data(5,i);
apo4 = apo_rx(4,:);
end
if (rmax<R3 && rmin>(R2+kerf))
hit = 1;
c=data(5,i)*ones(2,2);

```

```

data1(N+1,i) = 3;
apo_rx(3,i) = data(5,i);
apo3 = apo_rx(3,:);
end
if (rmax<R2 && rmin>(R1+kerf))
hit = 1;
c=data(5,i)*ones(2,2);
data1(N+1,i) = 2;
apo_rx(2,i) = data(5,i);
apo2 = apo_rx(2,:);
end
if (rmax<R1)
hit = 1;
c=data(5,i)*ones(2,2);
data1(N+1,i) = 1;
apo_rx(1,i) = data(5,i);
apo1 = apo_rx(1,:);
end
if hit == 0
c=data(5,i)*zeros(2,2);
end
hold on
surf(x,y,z,c)
end
% Put som axis legends on
Hc = colorbar;
view(3);
set(gca, 'FontSize', 34);
xlabel('x [mm]', 'FontSize', 34); %[mm]
ylabel('y [mm]', 'FontSize', 34); %[mm]
zlabel('z [mm]', 'FontSize', 34); %[mm]
grid;
axis('image');
hold off;

```

Appendix 3: Ultrasound and photoacoustic images of four point-absorbers acquired by simulated annular array concave ultrasound transducer before applying DR beam-forming

```
% Initialize field II program
field_init;
% Set initial parameters
load apo_rx01 % 8-element annular array aperture
Rfocus=12/1000;      % Geometric focus point [m]
ele_size=0.1/1000;   % Size of mathematical elements [m]
f0=40e6;             % Transducer center frequency [Hz]
fs=500e6;            % Sampling frequency [Hz]
cw=1540;             % Speed of sound in water[m/s]
R1=1.9488/1000;      % Radius of active aperture of transducer1 [m]
R2=2.82761434428389/1000;% Radius of active aperture of transducer2 [m]
R3=3.51692297169796/1000;% Radius of active aperture of transducer3 [m]
R4=4.10852202418295/1000;% Radius of active aperture of transducer4 [m]
R5=4.63783128930247/1000;% Radius of active aperture of transducer5 [m]
R6=5.12297440613297/1000;% Radius of active aperture of transducer6 [m]
R7=5.57470026881446/1000;% Radius of active aperture of transducer7 [m]
R8=6/1000;          % Radius of active aperture of transducer8 [m]
kerf=0.1/1000;      % Separation between each annuli [m]
% Set the sampling frequency
set_sampling(fs);
% Define transducer
Th = xdc_concave(R8, Rfocus, ele_size);
% Load previous defined 8-element annular array aperture
% Calculate the pulse echo field and display it
xpoints=(-1:0.01:1);
Lx = length(xpoints);

points_matrix1 = [xpoints; zeros(1,Lx); 10*ones(1,Lx)]';
points_matrix2 = [xpoints; zeros(1,Lx); 11*ones(1,Lx)]';
points_matrix3 = [xpoints; zeros(1,Lx); 12*ones(1,Lx)]';
points_matrix4 = [xpoints; zeros(1,Lx); 13*ones(1,Lx)]';
points_matrix = [ points_matrix1; points_matrix2; points_matrix3;
points_matrix4];
% Set the apodization for the individual mathematical elements
```

```

element_no=1;
% Define emit aperture
emit_aperture = xdc_concave(R8, Rfocus, ele_size);
apo_emit = sum(apo_rx,1);
ele_apodization (emit_aperture, element_no, apo_emit);
% Set the impulse response and excitation of the emit aperture
impulse_response=sin(2*pi*f0*(0:1/fs:2/f0));
impulse_response=impulse_response.*hanning(max(size(impulse_respon
se)))';
xdc_impulse (emit_aperture, impulse_response);
excitation=sin(2*pi*f0*(0:1/fs:2/f0));
xdc_excitation (emit_aperture, excitation);
%Generate PSF data received by 8 rings
for rd = 1:8
%Define receive aperture
receive_aperture = xdc_concave(R8, Rfocus, ele_size);
%Call apodization for all eight rings
ele_apodization (receive_aperture, element_no, apo_rx(rd,:));
% Set the impulse response for the receive aperture
xdc_impulse (receive_aperture, impulse_response);
[RF_data, start_time] = calc_hhp (emit_aperture, receive_aperture,
points_matrix/1000); %for US rf data

%[RF_data, start_time] = calc_hp(receive_aperture,
points_matrix/1000); %for PA rf data

% Store the result
image_data(1:max(size(RF_data)),1:size(points_matrix,1),rd)=RF_dat
a;
data = image_data(:, :, rd);
psf(:, :, rd) = data(:, 1:Lx);

psf1 = data(:, 1:Lx);
psf2 = data(:, Lx+1:2*Lx);
psf3 = data(:, 2*Lx+1:3*Lx);
psf4 = data(:, 3*Lx+1:4*Lx);
psf(:, :, rd) = psf1+psf2+psf3+psf4;
end

```

```

for j=1:Lx %j is the no_lines
a(:, :) = squeeze(psf(:, j, :));
for rd = 1:8
d(:, rd) = a(:, rd);
end
b(:, j) = sum(d, 2);
end
image=abs(hilbert(b));
%plot the data
sector = 2*max(xpoints)/1000;
x_scale = (sector*1000)*[1:Lx]./Lx;
y_scale = (start_time + [1:size(image, 1)]/fs)*(cw/2)*1000; %for US data
y_scale = (start_time + [1:size(image, 1)]/fs)*cw*1000; % for PA rf data
figure; imagesc(x_scale, y_scale, log(image));
set(gca, 'FontSize', 34);
xlabel('Lateral distance [mm]', 'FontSize', 34); % [mm]
ylabel('Depth[mm]', 'FontSize', 34); % [mm]
colormap gray;
brighten(-0.8);

```

Appendix 4: Ultrasound and photoacoustic images of four point-absorbers acquired by simulated annular array concave ultrasound transducer after applying DR beam-forming

```

load psf % Previous simulation raw data
load start_time % Previous simulation start_time
A = psf;
fs=500e6; % Sampling frequency [Hz]
cw=1540; % Speed of sound in water[m/s]
Rfocus=12/1000; % Focal radius of transducer [m]
R1=1.9488/1000; % Radius of active aperture of transducer1 [m]
R2=2.82761434428389/1000;% Radius of active aperture of transducer2 [m]
R3=3.51692297169796/1000;% Radius of active aperture of transducer3 [m]
R4=4.10852202418295/1000;% Radius of active aperture of transducer4 [m]
R5=4.63783128930247/1000;% Radius of active aperture of transducer5 [m]
R6=5.12297440613297/1000;% Radius of active aperture of transducer6 [m]
R7=5.57470026881446/1000;% Radius of active aperture of transducer7 [m]
R8=6/1000; % Radius of active aperture of transducer8 [m]
radius=[R1 R2 R3 R4 R5 R6 R7 R8]; % all ring radiuses
kerf=0.1/1000; % Separation between each annuli [m]
% midpoints of rings
radius2=[0 0.5*((radius(1:end-1)+kerf)+radius(2:end))];
s = size(A);
a = zeros([s(1) s(3)]);
b = zeros([s(1) s(2)]);
nstart = 1;
nend = s(1);
% computed parameters
Ts = 1/fs; % sampling interval
Ds = cw*Ts; % distance unit for one sampling interval

for j = 1:s(2) %j is the no_lines
a(:,j) = squeeze(A(:,j,:));
for rd = 1:s(3)
% z_data = (start_time+[0:nend-1]*Ts)*cw/2; % for US rf data
z_data = (start_time+[0:nend-1]*Ts)*cw; % for PA rf data
zB = z_data;
% for A-scan line n, do the delay and sum operations

```

```

Dzf = Rfocus-sqrt(Rfocus.^2-radius2(rd).^2);% delta Zf(ri) in the
notes
Dr = sqrt((zB-Dzf).^2+radius2(rd).^2); % hB(ri) in the notes
z_delay=Dr-zB;
Dly(:,rd)=interp1(zB/cw,a(:,rd),(zB/cw+z_delay/cw),'linear',0);
end
b(:,j) = sum(Dly,2);
end
%plot the data
image=abs(hilbert(b));
xpoints=(-1:0.01:1);
sector = 2*max(xpoints)/1000;
Lx = length(xpoints);
x_scale = (sector*1000)*[1:Lx]./Lx;
y_scale = (start_time+[1:size(image,1)]/fs)*(cw/2)*1000;%for US data
y_scale = (start_time+[1:size(image,1)]/fs)*cw*1000; % for PA rf data
figure;imagesc(x_scale, y_scale, log(image));
set(gca,'FontSize',34);
xlabel('Lateral distance [mm]','FontSize',34);
ylabel('Depth[mm]','FontSize',34);
colormap gray;
brighten(-0.8);

```